Compositional Inhomogeneity and Defects in Nanomaterials for Optoelectronics

by

Lifan Yan

A dissertation submitted in partial fulfillment
of the requirements for the degree of
Doctor of Philosophy
(Materials Science and Engineering)
in the University of Michigan
2017

Doctoral Committee:

Professor Joanna Mirecki-Millunchick, Chair
Professor Pallab K. Bhattacharya
Professor Emmanuelle Marquis
Dr. Kai Sun

Lifan Yan

ylifan@umich.edu

ORCID iD: 0000-0002-1162-9280

Acknowledgements

Today, I look back at my journey of pursuing the Ph.D. degree and think myself as a person of great luck to have achieved so much. There were a lot of moments of frustration and confusion. My special gratitude and appreciation to my advisor, Prof. Joanna Millunchick, for making me believe that every cloud has a silver lining and keeping encouraging me. She has been pouring her knowledge and giving inspiring advice on both my research and career.

I would also like to express my appreciation to the rest of my committee members: Prof. Pallab K Bhattacharya, Prof. Emmanuelle Marquis, and Dr. Kai Sun. A great deal of my work would not even be possible without Dr. Shafat Jahangir, Dr. Saniya Deshpande, Dr. Thomas Frost, Arnab Hazari's diligent work in Prof. Bhattacharya's lab. My sincere gratitude goes to Prof. Marquis for her invaluable suggestions on Atom Probe Tomography experiments and results analysis. Finally, my deepest thanks to Dr. Kai Sun for his selfless teaching in TEM knowledge as well as his demonstrations of exquisite techniques that will benefit me for the rest of my life. I would also like to acknowledge all funding agencies for this Ph.D. thesis.

Last but not least, I would like to thank my family for their unconditional love and support. My parents, Yongfu Yan and Xilu Xie, support me through the hardship. And I would like to thank my fiancé Allen for making me laugh when I need it most.

Table of Contents

Acknowledgements ii

List of Figures viii

List of Tables xvii

List of Acronyms xviii

Abstract xx

Chapter 1 Introduction and Background 1

1.1 Motivation 1

1.2 Overview of Compositional Inhomogeneity 2

1.2.1 Random Fluctuation 3

1.2.2 Thermodynamic Phase Separation 3

1.2.3 Kinetic Intermixing 6

1.2.4 Compositional Inhomogeneity & Defects 8

1.3 Goals and Objectives 9

1.4 Organization 9

Part I 10

Part II 11

1.5 References 14

Chapter 2 Structural & Compositional Characterization Techniques 18

2.1 Overview of Local Electro Atom Probe(LEAP) 18

2.1.1 Sample Preparation 20

2.1.2 Parameters Selection for Atom Probe Tomography 22

2.1.3 Data Reconstruction 23

2.2 Scanning Transmission Electron Microscopy 25

2.2.1 Specimen Preparation for STEM 26

2.2.2 STEM Imaging and Spectroscopy 29

2.3 References 32

Part I APT vs. STEM in 2D layers and Buried QD Nanostructures 36

Chapter 3 APT vs. STEM on 2D Layer Semiconductor Nanostructures 36

3.1 InGaN Bulk and Thin layer 37

3.1.1 Compositional Inhomogeneity in InGaN bulk layer 39

3.1.2 Compositional Inhomogeneity InGaN Ultra-Thin Layers 44

3.1.3 Summary 48

3.2 GaAsBi Bulk Layer 49

3.2.1 Impact of Droplet Formation on Compositional Inhomogeneity 50

3.2.2 Impact of Temperature on Bi Incorporation 57

3.3 References 64

Chapter 4 APT vs. STEM on Buried Quantum Dots Nanostructure 67

4.1 Ge QDs in AlAs 67

4.1.1 APT and TEM Results 69

4.1.2 Ge QDs in AlAs Growth Study 75

4.1.3 Summary 77

4.2 GaSb QDs with GaAs Capping Layer 78

4.2.1 APT reveals Droplet Epitaxy QD Formation Mechanism 79

4.2.2 STEM Imaging and EELS 83

4.2.3 Summary 85

4.3 Combining APT and STEM in Nanostructure Characterization 86

4.4 References 89

Part II Impact of Composition on Crystal Shape, Defect Formation and Optical Properties 91

Chapter 5 From Pure GaN nanowires to InGaN/GaN Heterostructure Nanowires 91

5.1 Motivation and Background 91

5.2 Pure GaN Nanowires 93

5.3 InGaN/GaN heterostructure nanowire LEDs 99

5.4 Summary 106

5.5 References 108

Chapter 6 Shape Evolution of High Lattice-Mismatched InGaN Nanowire Heterostructures... 111

6.1 Background 111

6.2 InGaN Nanowire Heterostructure 113

6.3 InN/InGaN Nanowire Bimodal Morphology 117

6.4 Bimodal Morphology Formation Mechanism 125

6.5 Optical Properties of InN/InGaN nanowire Heterostructure 127

6.6 Defects in InN/InGaN nanowires 129

6.6.1 Phase Switching & Secondary Growth 129

6.6.2 Cracks 133

6.7 Summary 136

6.8 References 138

List of Figures

Figure 1-1. Schematics showing composition fluctuation in (a) random alloy (b) spinodal alloy (c) clustering 3

Figure 1-2. Calculated Binodal and Spinodal Curves of InGaN[5] 5

Figure 1-3. (a) Atomistic XSTM Image indicating Sb segregation when InAs barrier layer is grown on top of InGaSb[21]; (b) Configuration Diagram for In/Ga exchange process [22] 7

Figure 2-1. Schematic of Atom Probe analysis chamber setup [1] 19

Figure 2-2. The V, total release method of APT sample preparation [8] 21

Figure 2-3. GaAs mass spectra using laser pulsed atom probe tomography[20] 24

Figure 2-4. Illustration of how to back fill a nanowire sample 27

Figure 2-5. An SEM image of FIB lift-out slab 28

Figure 2-6. Illustrations of scratch-off method for TEM sample prep using a syringe. 29

Figure 3-1. Temperature - composition phase diagram of InGaN alloy(a) Relaxed layer (b) Bi-axially strained InGaN layer. [20] 38

Figure 3-2. HAADF image of an In0.15Ga0.85N Bulk layer showing atomic abrupted interface between the substrate and the layer. 39

Figure 3-3.2D Iso-density plot for total ions from the (In)GaN sample, the six-fold symmetry pattern is indicated with dash line. 40

Figure 3-4. (a)Atom Probe Reconstruction of the In0.15Ga0.85N bulk layer with Indium(Cyan) and Ga(blue). (b) 1D concentration profile of Indium vs Distance(nm) 41

Figure 3-5. (a) 2D concentration contour plot of Indium in the bulk layer. (b) experimental concentration compared to the binomial distribution. (c) 1D concentration profile along the line(green) in (a). (d) 1D concentration profile along the line(blue) in (a) 43

Figure 3-6. (a) APT reconstruction showing In(red) ultra-thin layer from x-z plane viewpoint. (b) The 1D concentration profile of fraction of In vs Distance(nm) (c) 2D iso-concentration contour plot of the fraction of Indium ions. 45

Figure 3-7. (a) Cross sectional HAADF TEM image taken from InGaN Quantum Dots sample (b) EDS line profile across one QD[11] 46

Figure 3-8. Edge-on view of 3D reconstruction of InGaN QD Sample, Indium is denoted by red. 46

Figure 3-9. 1D In concentration profile along the growth direction with 2D iso-concentration contour plots of each layer on the left side 47

Figure 3-10. (a) Theta- 2 Theta XRD results on Sample A(black), B(magenta), and C(blue). (b) Planar view SEM image of Sample C (c) Sample B (d) Sample A, respectively......................... 52

Figure 3-11. (a) TEM image of cross section of sample A (b) APT reconstruction of Sample A showing inhomogeneous Bi distribution, denoted by blue dots (c) Line profile of Bi concentration of a cylindrical ROI (d)Illustration of the available elemental fluxes and different incorporation regimes when Ga droplets are present on the growth surface 53

Figure 3-12. (a) Cross Sectional TEM image of Sample C (b) spatial distribution of Bi atoms in APT reconstruction (c) 1D Bi concentration profile along Z axis. 54

Figure 3-13. (a) Cross Sectional TEM image of Sample B (b) APT reconstruction reveals lateral composition modulation (c) Line profile of Bi concentration for a cylindrical ROI. 55

Figure 3-14. (a) HAADF image of sample B, showing bright spots of GaAsBi in bulk film (b) GaAsBi precipitates formed on the surface on the sample, and one at the end of a sub grain boundary. (c) HAADF image of a zoomed in view on GaAsBi precipitates. Bi can be seen that has ordered on zinc blende (111). (d) APT reconstruction with iso-concentration surface for Bi at 3%. (e) line profile of the cylindrical ROI showing matrix of 1% Bi with fluctuation. 57

Figure 3-15. RMS and Bi incorporation vs Growth Temperature Tg... 58

Figure 3-16. Low magnification cross sectional TEM image showing smooth surface and uniform Bi incorporation for Sample D (b) High magnification HAADF image showing small

Bi-rich clusters uniformly distributed (c) HAADF image showing Bi-poor(dark) and Bi-rich (bright). 59

Figure 3-17. (a)APT reconstruction of sample D (2) 1D concentration profile of Bi along z axis of a cylindrical ROI. 60

Figure 3-18. (a) Cross Sectional TEM image of Sample E (340 ^{0}C) (b) APT reconstruction with Bi atoms denoted in blue (c) 1D conecntration profile of a cylindrical ROI. 60

Figure 4-1. Process for Ge QDs formation using in-situ annealing 68

Figure 4-2. Size distribution of APT results: number of Ge QDs vs. Volume (nm^3) 70

Figure 4-3. Atom Probe results of Ge(green) and Al(cyan) (b) iso-concentration surfaces are constructed using 6% Ge as a threshold. 71

Figure 4-4. Compositional profile across one of the iso-concentration surface constructed 71

Figure 4-5. TEM micrograph of Ge QDs buried in overgrown AlAs. Inset of HAADF image of Ge QDs 72

Figure 4-6. Trajectory aberrations and impact on the density due to changes in the surface curvature, low and high field precipitate.[17] 73

Figure 4-7. (a) 2D iso-density contour plot of Ge, Al and As ions. (b) Density plot of Ge ions.. 74

Figure 4-8. Core Concentration (Ge atomic %) vs. volume (nm^3) 75

Figure 4-9. (a) schematic of Ge QDs growth study sample (b) DF TEM image of three Ge QDs layers (c) APT reconstruction with distribution of Al(cyan), Ga (yellow) and Ge (red)............. 76

Figure 4-10. APT reconstruction of side view(top) and top view(bottom) of APT data for SK growth (left column) and DE growth (right column).. 81

Figure 4-11. Cross sectional profile of (a) SK QD and (b) DE QDs. Linear Sb composition profile of (c) QDs and (d) wetting layer. 81

Figure 4-12. Schematic detailing the (a) initial substrate, (b) droplet and ring formation, and (c) quantum dot formation stages of droplet epitaxy 82

Figure 4-13. Cross-sectional TEM images of capped (a)–(c) SK and (d) and (e) DE nanostructures. High-resolution images of an (b) intact SK dot, a (c) defected SK dot and a (e) DE ring.. 83

Figure 4-14. EELS profiles along lines shown in the TEM images for the (a)SK and (b) DE quantum dots.. 85

Figure 5-1. CL Spectrum of pure GaN nanowires (Sample A). 94

Figure 5-2. (a) Cross sectional SEM image of pure GaN nanowires (b) mono wavelength CL image at 370 nm (c) mono-wavelength CL image at 570 nm... 94

Figure 5-3. (a) Low Magnification Bright Field TEM image of pure GaN nanowire showing several stacking faults. (b) High Resolution Bright Field TEM image is showing the atomic structure of the stacking fault. The scale represents length of 2nm.. 96

Figure 5-4. (a) CL Spectrum of GaN nanowire sample grown at 550°C (Sample A2) (b) Cross sectional over layered CL image with SEM image (c) monowavelength CL image with filter centered at 2.14 eV (570 nm)... 97

Figure 5-5. (a) 52 tilted SEM image of sample A2. (b) low magnification TEM image of sample A2.. 97

Figure 5-6. Side and top view SEM images of InGaN/GaN nanowire LED structures grown at 800 °C and with a Ga flux of (a) 1.46 × 10-7 Torr grown of pure GaN nanowire (b) 1.94× 10-7 Torr (Sample C) (c) 1.64 × 10-7 Torr (Sample C), and (d) 1.46× 10-7 Torr (Sample D) with substrate temperature of 800 °C.. 100

Figure 5-7. Cathodoluminescence spectrum of InGaN/GaN nanowire LED structures (left) and Cross section over layered CL image (left) and SEM image (right) of InGaN heterostructure-nanowire (a) Sample B (b) Sample C and (c) Sample D (right). The scale bar represents the length of 1 μm.. 102

Figure 5-8. HAADF image of InGaN heterostructure wire structures. (a) strain-driven InGaN quantum dots with faceting (arrowed). (b) Faceted InGaN layers (arrowed)............................ 102

Figure 5-9. (a) Low magnification Bright Field image of a nanocrown (Sample D). (b) Low Magnification Bright Field image of a nanocrown in its early stages of formation (Sample C). (c) High Magnification Bright Field image of the feature boxed in (b) the arrows point out the grain boundary between the nascent nanocrown and the nanowire. (d) High Resolution Bright Field image of a nucleus that will develop into a nanocrown taken from Sample B.......................... 104

Figure 5-10. (a) SEM image of nanocrown and (b) CL image of the same area for wavelength range from 310 to 850nm. 105

Figure 6-1. Schematics of nanowire heterostructure morphologies (a) disc-in-nanowire heterostructure (b) 3D island nucleation within nanowire (c) Quantum dot forming caused by pyramidal growth (d) pin head structure. 113

Figure 6-2. (a) Demonstrate of growth temperature(black) and group III fluxes used for Sample C (red for Ga and blue for In). 115

Figure 6-3. SEM and TEM images for InxGa1-xN heterostructure Nanowires (a) x = 0.3 (b) x = 0.85 (c) x = 1.0. 117

Figure 6-4. (a) SEM image of nanowire morphology for Sample C at 52°tilted, nanowires with pencil shape and polyhedral bead morphology are observed (b) Cross section STEM image of nanowires for Sample C. 118

Figure 6-5. (a) HAADF STEM micrograph of a nanowire carrying features with both pencil shape and bead shape morphologies, with zoomed in micrographs from the top to the bottom of the active region. (b) Top most layer of InN nanodisk: intra dot formed within the nan nanowire (c) 3rd InN nanodisk region, octahedral shape bead formed (d) 2nd InN nanodisk region, facet formed and material latter being deposited could grow into branches on sidewall (e) 1st InN nanodisk region, diameter increase after In is introduced. A core-shell structure formed with n-GaN as the core and p-GaN as the shell. 120

Figure 6-6. (a)-(d) EDS mapping results of a pencil shape nanowire (a) field of view with line indicating direction of line profile (b) Ga-rich region (c) In-rich region (d) line profile of calculated In ratio. 121

Figure 6-7. HAADF STEM micrograph of the half laser structure (Sample B) with zoomed in micrograph of the active region. 123

Figure 6-8. EDS Mapping results of a nanowire with half laser structure. (b) Ga-rich region (c) In rich region (d) Line profile of calculated In ratio. 123

Figure 6-9. (a) Schematic showing the Initial stage nanowire structure (b) BF TEM image of a initial stage nanowire (c) schematic showing observed crystal planes for initial stage nanowires (d) line profile of In composition along the growth direction 125

Figure 6-10. Schematic illustrating the formation of two morphologies. 126

Figure 6-11. PL results of Sample A. Low temperature to room temperature (a) PL intensity and (b) Peak photon energy, both experimental data point and fitted curve. (Courtesy of Arnab Hazari) 128

Figure 6-12. (a) HAADF STEM image of the active region in Sample C, InN and InGaN region being pointed out (b) BF STEM image of the same region (c) BF image of the region circled out the region in (b). Switching between wurtzite (WZ) and zinc blende (ZB). 130

Figure 6-13. (a) HAADF STEM image of a bead shape nanowire, with region zoomed in (b) circled out. (b)BF TEM image showing change of growth front change upon phase switching (c)

FFT diffraction pattern of zinc clende(ZB) region (d) FFT diffraction pattern of wurtzite(WZ) region. 130

Figure 6-14. (a) BF TEM image of $In_{0.5}Ga_{0.5}N$ nanowire (b) HRTEM image of lateral branching upon zinc blende regions. 132

Figure 6-15. (a) HAADF TEM image showing twinning precipitates nucleate on nanowire sidewall (b) FFT of the entire image, twinning can be seen. (c) FFT of the area circled out with the red square area. 133

Figure 6-16. HAADF TEM image of a bead with cracks on the right side (b) zoomed in high resolution image.......... 134

Figure 6-17. Measured crack length vs. the thickness of the whole beads. 135

Figure 6-18. HAADF TEM image (left) of a bead shape nanowire with the position of the cracks pointed out. (b) EDS mapping of Ga in the area (b) EDS mapping of In in the area. 135

List of Tables

Table 3-1. Indium atom density #/nm2 for each InGaN QD wetting layer 48

Table 3-2. Growth Conditions for GaAsBi bulk film samples 50

Table 3-3. Pearson Coefficients and Bi atomic percentage for samples investigated. 62

Table 5-1. Growth parameters and morphologies of InGaN/GaN heterostructure-nanowire 99

List of Acronyms

APT	Atom Probe Tomography
TEM	Transmission Electron Microscopy
STEM	Scanning Transmission Electron Microscopy
XRD	X-ray Diffraction
QW(s)	Quantum Wells
NW(s)	Nanowires
QD(s)	Quantum Dots
PLAP	Pulse laser atom probe
MBE	Molecular Beam Epitaxy
CL	Cathodoluminescence
SEM	Scanning Electron Microscopy
FIB	Focused Ion Beam
LEAP	Local Electrode Atom Probe
SK	Stranski- Krastanov
LED	Light Emitting Diode
HAADF	High Angle Annular Dark Field

MOCVD	Metal-Oxide Chemical Vapor Deposition
ROI	Region of Interest
FWHM	Full With Half Maximum
DE	Droplet Epitaxy
EELS	Electron Energy Loss Spectroscopy
EDS	Energetic Dispersive X-ray Spectroscopy
RMS	Root Mean Square
TD	Threading Dislocation
EL	Electroluminescence
PL	Photoluminescence
BF	Bright Field
DF	Dark Field
FFT	Fast Fourier Transform

Abstract

Semiconductor nanostructures are used in various optoelectronic applications such as solar cells, lasers, and quantum computing. The quantum confinement within these nanostructures is realized through precise control of composition, so it is crucial to understand any compositional inhomogeneities may occur within these structures. This work focuses on compositional inhomogeneities within nanostructures for a number of III-V material systems, and how they affect their optical properties. This thesis is organized in two parts: the first part concentrates on comparing and contrasting the application of Atom Probe Tomography (APT) and Scanning Transmission Electron Microscopy (STEM) in investigating composition inhomogeneity in III-V semiconductor alloys. 2D layers, such as InGaN/GaN and GaAsBi/GaAs, and buried Quantum Dots (QDs), such as Germanium QDs in AlAs and GaSb QDs in GaAs are examined. For ***2D layers***, the 30 nm-thick InGaN layer only presents random alloy composition fluctuation, while QWs less than 1 nm thick show nano-clustering. For GaAsBi bulk layer, it is found that surface droplets can induce composition inhomogeneities since Ga droplets can enhance Bi incorporation. Although samples without any surface droplets are more uniform, lateral composition modulation, pores, as well as GaAsBi precipitates can occur. Surface roughness is proposed to be another cause for non-uniform Bi incorporation. ***Buried QD*** nanostructures are also studied: Ge QDs are induced by high temperature annealing and form to reduce interfacial energy. A combined APT and STEM study shows that the formation mechanism for QD depends strongly on the growth method. For instance, Droplet Epitaxy method results in the formation of smaller and more dilute GaSb QD pairs compared to the more typical Stranski-Kranstanov method. Nonetheless, both methods result in similar compositional profiles along the wetting layers. The second part discusses the role of compositional inhomogeneity and defects play in optical properties of InGaN heterostructure nanowires. For $In_{0.4}Ga_{0.6}N/GaN$ nanowires, compositional inhomogeneities and defects present themselves in various aspects and affect the local optical property. A six-fold lateral branching structure is also observed, and nanowires with lateral branches are optically inactive under room temperature. Higher strained $InN/In_{0.4}Ga_{0.6}N$ heterostructure nanowires have more pronounced composition induced changes. These nanowires also exhibit more complicated strain relaxation mechanisms, such as phase switching and cracking.

Chapter 1 Introduction and Background

1.1 Motivation

Semiconductor nanostructures have been playing an important role in the development of optoelectronics devices for the past decades; they are widely used as solar cells, LEDs, lasers, and photodetectors. The word, “Nano,” originates from the Greek and has the meaning, “dwarf”. A structure needs to be under 100 nm in either one of the three dimensions to be titled as a nanostructure. It is usually classified by the number of dimensionalities that provides electron confinement. A Quantum Well (QW) structure has confinement in only one dimension while the other two dimensions are extended. Structures, like nanowires (NWs) and nanotubes, have quantum confinement in both x and y dimension, only extending in z direction. Quantum Dots (QDs) have confinement in all three dimensions. The band structure of a quantum dot emulates that of a single atom, and can give off photons at a precise energy level, which is ideal for optoelectronic devices.

Semiconductor nanostructures have been intensively investigated for their properties, such as size dependent luminescence and absorption. Precise bandgap engineering is made possible with low dimensional nanostructures, thanks to the development in both theory and experiment. To precisely control the band structure, a highly-controlled growth environment is required. Molecular Beam Epitaxy (MBE), which takes place in an ultra-high vacuum chamber with molecular beams from solid sources of pure elements, can achieve high purity films.

The quantum confinement within these nanostructures is realized through precise control of composition, so it is crucial to understand any compositional inhomogeneities may occur within these structures. **The main subject of this dissertation is how composition varies within nanostructures for a number of III-V materials systems.** What is the magnitude of compositional inhomogeneity? 2D layers, such as InGaN/GaN and GaAsBi/GaAs, and buried QDs structures, such as Ge QDs in AlAs and GaSb QDs in GaAs, are studied and their compositional inhomogeneity issues are discussed. At the same time, does the strain field induced by compositional inhomogeneity cause morphological changes and/or defects? In this thesis, III-Nitride Nanowires will be used as a demonstration of how compositional inhomogeneity can induce crystal shape change, morphology variation, and defect formation. Both structural and compositional properties will be shown. And how they affect the local optical properties of these nanostructures will be discussed.

1.2 Overview of Compositional Inhomogeneity

The goal of this overview is to briefly discuss three main causes for compositional inhomogeneity in compound semiconductor nanostructures. In Figure 1-1, blue dots represent the species of interest when studying the inhomogeneity. Three Commonly seen compositional inhomogeneities are illustrated: random composition fluctuation, spinodal phase separation and clustering. The most known reason for inhomogeneities is thermodynamics, as it provides the chemical driving force for phase separation or mixing. Thermodynamics is used to explain the driving force, and kinetics is involved to describe how the growth is done. Crystal growth in MBE is governed by the interaction of molecular beam since it is carried out in a high vacuum chamber.[1] Therefore, kinetics is another main reason for inhomogeneities. However, even when it is as homogeneous as possible, the III-V semiconductor alloy will contain random compositional fluctuation.

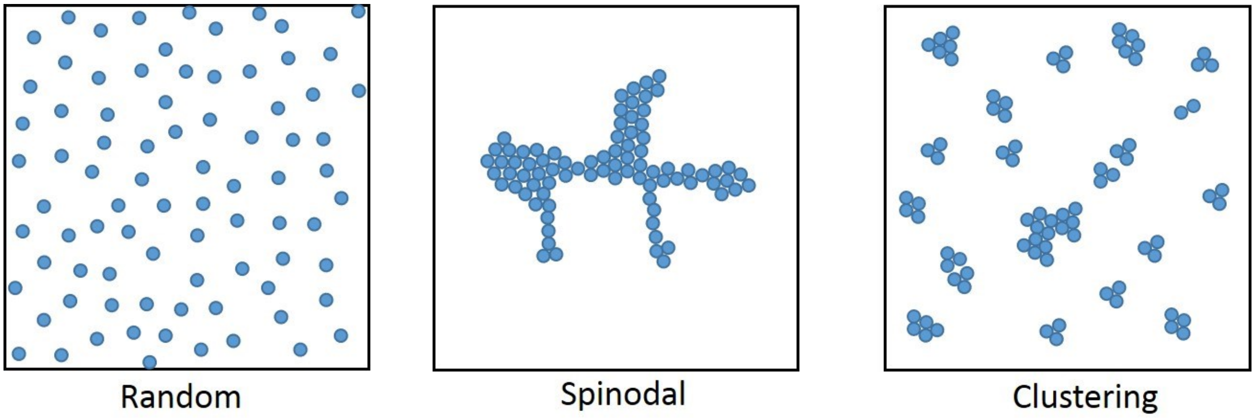

Figure 1-1. Schematics showing composition fluctuation in (a) random alloy (b) spinodal alloy (c) clustering

1.2.1 Random Fluctuation

In a random binary alloy, A_xB_{1-x}, A and B atom would randomly take up the lattice site. The random composition fluctuation, is described by the standard deviation, denoted by σ, for a measured composition. Take $In_xGa_{1-x}N$ as an example, the standard deviation is derived as $\sigma_X = \sqrt{\frac{x(1-x)}{n}}$ for a data set with n atoms a nominal composition of x with the assumed binomial distribution. [2] If examined on a small enough length scale, any random alloy would show random statistical fluctuation in composition.

1.2.2 Thermodynamic Phase Separation

Phase separation is defined as the conversion of a single-phase system into a two, or multiple, phase system, in which each phase is chemically stable and physically distinct. Phase separation occurs whenever a material transitions into the unstable region of its phase diagram. Miscibility gap is a typical thermodynamic phenomenon. Classical nucleation and spinodal decomposition are possible within the miscibility gap. Studies in single crystalline epitaxial layers in systems of $AlGa_xAs_{1-x}$, $GaAs_xBi_{1-x}$, $In_xGa_{1-x}N$ have demonstrated the existence of miscibility gaps for these material systems. [3, 4, 5]

Simulation work can be done to predict the inhomogeneities based on thermodynamics theories, namely calculating Gibb's free energy of the solution at a certain temperature. III-Nitride semiconductor alloys are famous for their tendency to form phase separation due to spinodal decomposition. [6] Ho and Stringfellow report the first simulated binodal and spinodal curves for InGaN system using valence-force-field model (VFF) [5] in Figure 1-2, the solid binodal line defines the composition regime in which the alloys are thermodynamically unstable. When the system falls into regime underneath the binodal line, the system can lower its free energy by separating into two phases with an interface in between. Inside the binodal line, the broken spinodal line indicates regime where phase separation can happen without an energy barrier at a given temperature. Any compositional fluctuations within this composition regime can lead to a phase separation. The spinodal and binodal line have provided a brief roadmap to predict bulk material compositional inhomogeneity.

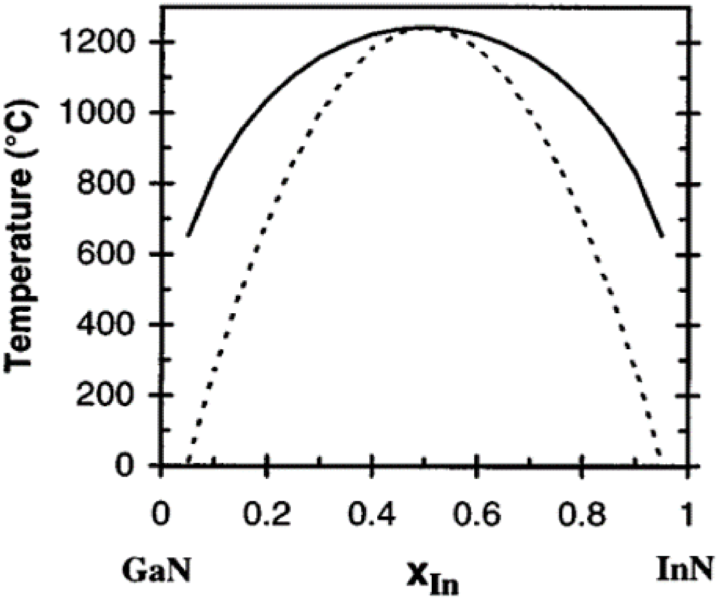

Figure 1-2. Calculated Binodal and Spinodal Curves of InGaN[5]

However, a real-life situation is more complicated than this simple simulation. When working with bulk films of ternary semiconductor alloys, researchers discovered the "Compositional Pulling Effect", produced by the high strain at the interface during epitaxial growth. [7] The composition of a certain element, for example the In in InGaN alloy, will be significantly lower at the interface and increases along the growth, as the strain is relaxed after that.

Compositional inhomogeneity situation also varies depending on the growth technique that has been used.[9] The MBE growth process is mostly considered kinetically controlled because its high deposition rate, which is proven to be able to hinder spinodal decomposition. [10] The solid composition is largely controlled by the sticking coefficients of the atoms, or molecules impinging on the surface. Therefore, metastable alloys can be regularly produced during MBE growth.[9] Since most of the samples for this work are grown by MBE, kinetics is another factor that needs to be taken into consideration.

1.2.3 Kinetic Intermixing

Perhaps the most well understood kinetic intermixing is the one occurs at the growth surface. It is considered one of the main reasons for broaden interfaces in quantum well super lattices heterostructures. Take a heterostructure that contains InGaSb/InAs superlattices as an example, the InGaSb on InAs interfaces are abrupt, while the InAs on InGaSb interfaces are diffuse. The broadness of the interface correlates with the surface segregation of InGaSb. In other words, atoms of the InGaSb move towards the surface during the growth. Figure 1-3 shows a cross sectional Scanning Tunneling Microscopy image, clearly indicating Sb segregation into the barrier InAs layer grown on top of InGaSb quantum well.

Differences in binding energy and atomic size are two elements that affect this process. For III-V semiconductor materials, it is possible to have surface segregation on both group III elements and group V elements. Group III elements segregation in both quantum wells and quantum dots have been studied, and a numerous amount of papers have been published on: InGaAs/InAlAs QWs [11],InGaAs/GaAs QWs [12,13,14,15], InGaAs QDs [16], and InAs QDs [17] Group V elements segregation has been studied in QWs [18]and superlattice GaAs/GaSb[19], InAs/GaSb[20] and InAs/GaInSb. [21]

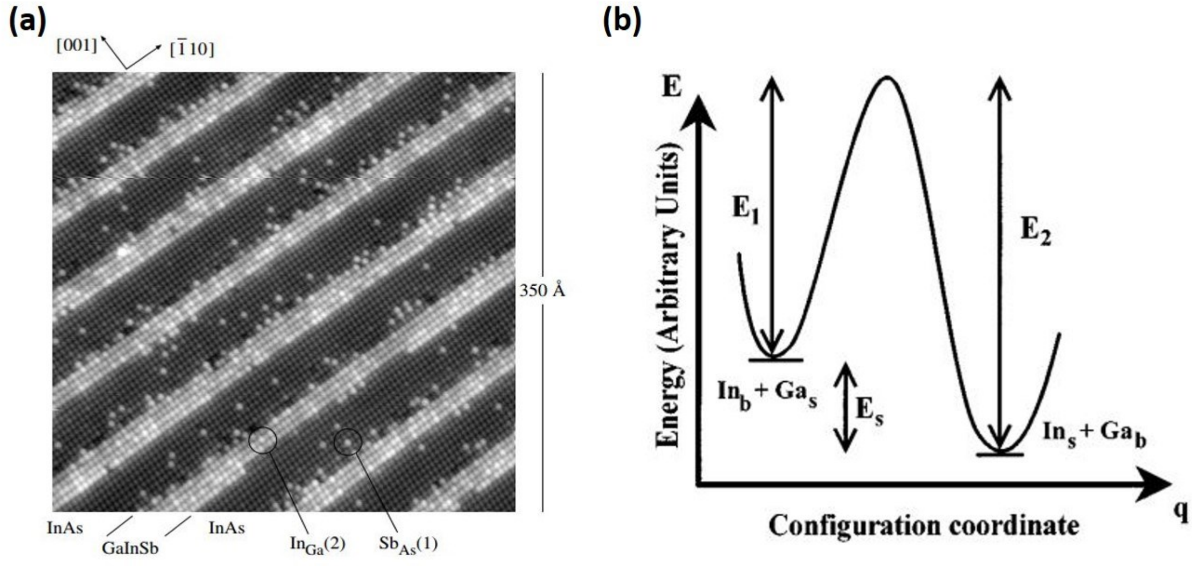

Figure 1-3. (a) Atomistic XSTM Image indicating Sb segregation when InAs barrier layer is grown on top of InGaSb[21]; (b) Configuration Diagram for In/Ga exchange process [22]

The first model that describes epitaxial growth segregation is developed by Muraki et al.[23], in which a constant fraction of the species of interest is being exchanged between the surface layer and the bulk. This model provided some preliminary simulation guidance to predict surface segregation and intermixing. However, it only considers the exchange between the topmost deposited layer and the under-layering substrate. A more complicated model was later proposed and the top three layers of atoms can all participate in the exchange process. [24] This model was used to investigate the Ge segregation and accumulation issue when grown on top of Si. Later, a more justified model for MBE growth was proposed by Dehaese et al. [25] in which they consider the total free energy of the exchange process (shown in Figure 1-3(b)). As shown above, E_s is the "segregation energy" of the equilibrium mode. An exchange process is done by overcoming the energy barrier E_1; the reverse process is also possible, but a higher energy barrier E_2 needs to be overcome. This model fits the results of MBE growth nicely based on its assumption of a low substrate temperature and high growth rate. The segregation energy and the activation energy can be fitted, or theoretically simulated, in multiple semiconductor systems: Si/Ge[24], InGaAs and

AlGaAs [26, 27], and III- Nitride. [28] A typical segregation energy for Si/Ge or Arsenide alloy ranges from 0.15- 0.4 eV, depending on surface conditions. Simulation work found that the segregation energies for III-Nitride alloy are much higher (1.65 eV- 3.85 eV), almost a magnitude higher than the typical value in other III/V and Si/Ge material system. The segregation energy is also largely affected by the polarity of the growth surface. When studying the effect of Sb in preventing InAs QDs decompose, it is reckoned that Godbey's and Dahaese's model should be combined and that it gives the best fit to experimental segregation data collected by atomic resolution XSTM. [29]

1.2.4 Compositional Inhomogeneity & Defects

It has been recognized that compositional inhomogeneities and defects mutually promote each other. An inhomogeneous and defective film can be induced by the large strain undergoes within them. To release the high strain, stacking faults and dislocations are usually inserted. For example, coalescence of small islands and dislocation networks are found in InAs/GaAs [30], I1 type basal stacking faults in InGaN/GaN interface[31, 32]; stacking faults and threading dislocations for strained Si on relaxed SiGe layer. [33] It is also common to observe strain relaxation through surface roughening and other surface defects: in SiGe [34], InAs/GaAs[35], and InGaN/GaN. [36]

When the alloy is in an unstable regime, small defects or fluctuation can induce compositional inhomogeneity. Bertram et al. claimed that surface defects in thick InGaN film are more likely to have In segregation around them. These surface defects are an indicator to threading dislocations (TD) underneath. It is recognized that defects would induce In segregation.[37] On the other hand, compositional inhomogeneity motivates crystal defects. Empirical interatomic potentials and Monte Carlo simulation show compositional inhomogeneity is more pronounced around edge dislocation than screw dislocation. [38]

1.3 Goals and Objectives

There are two main goals of this dissertation. The first goal is to compare and contrast Atom Probe Tomography (APT) and Transmission Electron Microscopy (TEM) in studying compositional inhomogeneities, which will be the content of the first part. 2D layers, both InGaN/GaN and GaAsBi/GaAs nanostructures, will be studied and discussed. APT's capabilities and remaining challenges in investigating 2D layer nanostructures will then be explained. Additionally, the application of APT and TEM in examining buried QDs nanostructures will be discussed. Ge QDs in AlAs and GaSb QDs in GaAs will be the material systems studied.

Another goal of this dissertation is to determine how composition affects crystal shape, defect formation, and optical properties of III-V nanostructures. This part focuses on only one specific type of nanostructure: the InGaN heterostructure nanowire. $In_{0.4}Ga_{0.6}N$ heterostructure nanowires are used to study how structural and compositional properties are correlated to local optical properties. The effect of composition on crystal shape/nanowire morphology and defect formation will be analyzed for InN heterostructure nanowire.

1.4 Organization

Chapter 1: This chapter is the introduction to the thesis. It first discusses the motivation to study the compositional inhomogeneity problem in semiconductor nanostructures. The overview section discusses three commonly seen reasons for compositional inhomogeneity. The following section describes the organization of the thesis. The main body of this thesis is separated into two parts, with each part containing two chapters respectively. The content for each chapter is summarized individually.

Chapter 2: This chapter introduces the two primary characterization techniques used in this thesis: Atom Probe Tomography and Transmission Electron Microscopy. It starts with introducing basic working principles of APT, and followed by sample preparation, parameter selection for APT experiments, and data reconstruction. For the TEM part, it focuses on Scanning Transmission Electron Microscopy(STEM) since it is heavily used in this thesis. Novel approaches for sample preparation will be first described. Then, the imaging and spectroscopy techniques used will also be discussed.

Part I

Part I focuses on comparing and contrasting the application of APT and STEM in investigating composition inhomogeneity issues in III-V semiconductor nanostructures. Two main types of nanostructures that have been studied are 2D layers and buried Quantum Dots: InGaN/GaN layers, GaAsBi bulk layers, Germanium QDs in AlAs, and GaSb QDs in GaAs. For all four material systems, their brief backgrounds and growth methods will be described first. APT reconstructions and TEM results will be shown, and the associated analysis and explanation will be elaborated in details.

Chapter 3: Application of APT on various semiconductor material systems is made possible with the development of laser pulsed APT. In this chapter, GaAsBi bulk layers and InGaN quantum wells are characterized using pulse laser atom probe(PLAP). TEM data give precise morphology information. Side by side comparison of APT and STEM data gives a systematic characterization of low incorporation Bi film samples. Bulk layer InGaN on GaN is characterized first as a reference point. The composition profile is compared to a binomial distribution and shows bulk InGaN layers only have random alloy fluctuation. Furthermore, thin InGaN layer results indicate clustering happens. For GaAsBi bulk layer, it is found that surface droplets can induce composition inhomogeneities since Ga droplets can enhance Bi incorporation. Although samples without any surface droplets are more uniform, lateral composition modulation, pores, as well as GaAsBi precipitates can occur. Surface roughness is then proposed to be another cause for non-uniform Bi incorporation.

Chapter 4: This chapter compares the APT and STEM data for two buried QD nanostructure: Ge QDs in AlAs and GaSb QDs with GaAs capping layer. APT data suggest Ge QDs have an elliptical shape with a gradual interface, while the STEM results indicate a more spherical shape. Trajectory aberration can cause the discrepancy. The size distribution is rather exponential with a long tail and Ge core concentration increases as the QD volume increases. For GaSb QDs project, both Stranski-Krastanov (SK) growth and Droplet Epitaxy(DE) growth QDs are studied. SK QDs have a truncated, pyramidal shape, and they disintegrate upon GaAs capping. DE grown QDs are much smaller than SK QDs and are located on the opposite position on the perimeter of the ring feature. Sb incorporation for DE dots is much lower than SK dots, while Sb concentration for wetting layers are about the same.

Part II

For the second part, the role of compositional inhomogeneity and defects play in optical properties of InGaN heterostructure nanowires will be investigated and discussed. Two sets of nanowires are used in this part: $In_{0.4}Ga_{0.6}N$/GaN and InN/$In_{0.4}Ga_{0.6}N$ heterostructure nanowires. For $In_{0.4}Ga_{0.6}N$/GaN nanowires, compositional inhomogeneity and defects present themselves in various aspects and affect the optical property. A six-fold lateral branching structure is also observed, and nanowires with lateral branches are optically inactive under room temperature. As a higher strained system, the compositional inhomogeneity problem is more pronounced in InN/$In_{0.4}Ga_{0.6}N$ heterostructure nanowires. It not only induces crystal shape change during the growth but also complicates the strain relaxation mechanism.

Chapter 5: A brief introduction to In-rich InGaN nanowire heterostructures will be included. This chapter starts with the morphology and local optical properties for pure GaN nanowires. Pure GaN nanowires grown at 820 °C have strong emission at 370 nm (3.38 eV), which is consistent with the GaN bandgap. The spectrum also shows a broad peak at 570 nm (2.17 eV) and a side peak at 410 nm (3 eV), both are defects related. It then describes the optical and structural properties of $In_{0.4}Ga_{0.6}N$/GaN nanowire. The Cathodoluminescence (CL) results indicate these nanowires have a broad yet strong emission at the target wavelength range (635nm). The broad emission peak can be attributed to faceting, indium clustering, and defects. A unique 6-fold lateral branching structure called “Nano-crown” is also observed. Nanowires with lateral branching are optically inactive at room temperature.

Chapter 6: This chapter starts with nanowire morphology evolution with increment of In incorporated into these nanowires. It then focuses on the compositional inhomogeneity issue in highly strained InN/$In_{0.4}Ga_{0.6}N$ heterostructure nanowires. For this case, the compositional inhomogeneity induces the bimodal morphology, the pencil shape and the bead-shape nanowires. The pencil shape nanowire has less total Indium incorporation and branches, while the bead shape nanowires exhibit high Indium content and strain relaxation related defects. During the growth, Ga segregates axially and forms GaN shell. It has also been observed that Indium segregates along the nanowire axis. Secondary growth is often observed for these nanowires, small nucleus and precipitation can form on the sidewalls. Stacking faults and phase switching are also observed for bead shape nanowires. The crystal structure can switch between wurtzite to zinc blende, the zinc blende regions can further act as seeds for nanowire lateral branching.

1.5 References

1. Naganuma, M. GaAs , Gap , and GaAs , - , P , Films Deposited by Molecular Beam Epitaxy. **187,** 187–200 (1975).

2. Galtrey, M. J. *et al.* Response to 'Comment on "Three-dimensional atom probe studies of an In[sub x]Ga[sub 1−x]N/GaN multiple quantum well structure: assessment of possible indium clustering"' [Appl. Phys. Lett. 91, 176101 (2007)]. *Appl. Phys. Lett.* **91,** 176102 (2007).

3. Markowitz, P. D., Zach, M. P., Gibbons, P. C., Penner, R. M. & Buhro, W. E. Phase separation in AlxGa1-xAs nanowhiskers grown by the solution-liquid-solid mechanism. *J. Am. Chem. Soc.* **123,** 4502–4511 (2001).

4. Wu, M., Luna, E., Puustinen, J., Guina, M. & Trampert, A. Formation and phase transformation of Bi-containing QD-like clusters in annealed GaAsBi. *Nanotechnology* **25,** 205605 (2014).

5. Ho, I. & Stringfellow, G. B. Solid phase immiscibility in GaInN. *Appl. Phys. Lett.* **69,** 2701–2703 (1996).

6. Stringfellow, G. B. Microstructures produced during the epitaxial growth of InGaN alloys. *J. Cryst. Growth* **312,** 735–749 (2010).

7. Stringfellow, G. B. The importance of lattice mismatch in the growth of Ga $_x$ In $_{1-x}$ P epitaxial crystals. *J. Appl. Phys.* **43,** 3455–3460 (1972).

8. Rao, M., Kim, D. & Mahajan, S. Compositional dependence of phase separation in InGaN layers. *Appl. Phys. Lett.* **85,** 1961–1963 (2004).

9. Stringfellow, G. B. Immiscibility and spinodal decomposition in III/V alloys. *J. Cryst. Growth* **65,** 454–462 (1983).

10. Tersoff, J. Spinodal decomposition during step-flow growth. **56,** 4394–4397 (1997).

11. Gerard, J. In situ probing at the growth temperature of the surface composition of (InGa)As and (InAl)As. *Cit. Appl. Phys. Lett* **61,** (2096).

12. Nagle, J., Landesman, J. P., Larive, M., Mottet, C. & Bois, P. Indium surface segregation in strained GaInAs quantum wells grown on GaAs by MBE. *J. Cryst. Growth* **127,** 550–554 (1993).

13. Moran, M. *et al.* Indium segregation in (111) B GaAs – In x Ga 1 − x As quantum wells determined by transmission electron microscopy. *J. Phys. D. Appl. Phys.* **34,** 1943 (2001).

14. Drozdov, Y. N. *et al.* Segregation of indium in InGaAs/GaAs quantum wells grown by vapor-phase epitaxy. *Semiconductors* **37,** 194–199 (2003).

15. Litvinov, D. *et al.* Influence of InGaAs cap layers with different In concentration on the properties of InGaAs quantum dots. *J. Appl. Phys.* **103,** (2008).

16. Djie, H. S. *et al.* Intermixing of InGaAs quantum dots grown by cycled monolayer deposition. *J. Appl. Phys.* **100,** (2006).

17. ZolotaryovA Schramm, A., Heyn, C., Hansen, W., Zolotaryov, A. & Schramm, A. InAs-coverage dependence of self-assembled quantum dot size, composition, and density. *Cit. Appl. Phys. Lett* **91,** (2007).

18. Harmand, J. C., Li, L. H., Patriarche, G. & Travers, L. GaInAs/GaAs quantum-well growth assisted by Sb surfactant: Toward emission GaInAsÕGaAs quantum-well growth assisted by Sb surfactant: Toward 1.3 □m emission. *Cit. Appl. Phys. Lett* **84,** (2004).

19. Dorin, C., Mirecki, J., Wauchope, M., Millunchick, J. M. & Wauchope, C. Intermixing and lateral composition modulation in GaAs/GaSb short period superlattices. *J. Appl. Phys.* **94,** (2003).

20. Schmitz, J. *et al.* Optical and structural investigations of intermixing reactions at the interfaces of InAs/AlSb and InAs/GaSb quantum wells grown by molecular-beam epitaxy. *or Cryst. GROWTH ELSEVIER J. Cryst. Growth* **150,** 858–862 (1995).

21. Steinshnider, J. *et al.* Origin of antimony segregation in GaInSb/InAs strained-layer superlattices. *Phys. Rev. Lett.* **85,** 4562–4565 (2000).

22. Dehaese, O., Wallart, X. & Mollot, F. Kinetic model of element III segregation during molecular beam epitaxy of III-III'-V semiconductor compounds. *Appl. Phys. Lett.* **52,** 52

(1995).

23. Muraki, K., Fukatsu, S., ShirakiR Ito, Y., Shiraki, Y. & Ito, F. Surface segregation of In atoms during molecular beam epitaxy and its influence on the energy levels in InGaAs/GaAs quantum wells *Appl. Phys. Lett.*. **61,** 141913–2245 (1992).

24. Godbey, D. J. & Ancona, M. G. Modeling of Ge segregation in the limits of zero and infinite surface diffusion. *J. Vac. Sci. Technol. A Vacuum, Surfaces, Film.* **15,** 976–980 (1997).

25. Dehaese, O., Wallart, X. & Mollot, F. Kinetic model of element III segregation during molecular beam epitaxy of III-III???-V semiconductor compounds. *Appl. Phys. Lett.* **52,** 52 (1995).

26. Moison, J. M. *et al.* Surface segregation in III-V alloys. *J. Cryst. Growth* **111,** 141–150 (1991).

27. Landesman, J. P. *et al.* in *Semiconductor Interfaces at the Sub-Nanometer Scale* (eds. Salemink, H. W. M. & Pashley, M. D.) 105–113 (Springer Netherlands, 1993). doi:10.1007/978-94-011-2034-0_11

28. Bogusławski, P., Rapcewicz, K. & Bernholc, J. Surface segregation and interface stability of AlN/GaN, GaN/InN, and AlN/InN {0001} epitaxial systems. *Phys. Rev. B* **61,** 10820–10826 (2000).

29. Bozkurt, M., Ulloa, J. M. & Koenraad, P. M. An atomic scale study on the effect of Sb during capping of MBE grown III–V semiconductor QDs. *Semicond. Sci. Technol.* **26,** 64007 (2011).

30. Yamaguchi, H. *et al.* Atomic-scale imaging of strain relaxation via misfit dislocations in highly mismatched semiconductor heteroepitaxy: InAs/GaAs(111)A. *Phys. Rev. B* **55,** 1337–1340 (1997).

31. Wu, Z. H. *et al.* Partial strain relaxation by stacking fault generation in InGaN multiple quantum wells grown on (1 1- 01) semipolar GaN. *Appl. Phys. Lett.* **98,** (2011).

32. Fischer, A. M. *et al.* Misfit strain relaxation by stacking fault generation in InGaN

quantum wells grown on m-plane GaN. *Appl. Phys. Express* **2,** 0410021–0410023 (2009).

33. Bedell, S. W., Fogel, K., Sadana, D. K., Chen, H. & Domenicucci, A. Observation of stacking faults in strained Si layers. *Appl. Phys. Lett.* **85,** 2493–2495 (2004).

34. Ozkan, C. S., Nix, W. D. & Gao, H. Strain relaxation and defect formation in heteroepitaxial Si1−xGex films via surface roughening induced by controlled annealing experiments. *Appl. Phys. Lett.* **70,** 2247–2249 (1997).

35. Pearson, C., Dorin, C., Mirecki-Millunchick, J., Chen, Y. & Orr, B. Compositionally modulated structures studied by in situ scanning tunneling microscopy. *Mater. Res. Symp. Proceeding Vol.* **696,** 8–12 (2002).

36. Cho, H. K., Lee, J. Y., Yang, G. M. & Kim, C. S. Formation mechanism of V defects in the InGaN/GaN multiple quantum wells grown on GaN layers with low threading dislocation density. *Appl. Phys. Lett.* **79,** 215–217 (2001).

37. Bertram, F. *et al.* Microscopic correlation of redshifted luminescence and surface defects in thick InxGa1-xN layers. *Appl. Phys. Lett.* **80,** 3524–3526 (2002).

38. Sakaguchi, R., Akiyama, T., Nakamura, K. & Ito, T. Theoretical investigations of compositional inhomogeneity around threading dislocations in III-nitride semiconductor alloys. *Jpn. J. Appl. Phys.* **55,** (2016).

Chapter 2 Structural & Compositional Characterization Techniques

Two primary characterization techniques are utilized in this thesis: Atom Probe Tomography and Scanning Transmission Electron Microscopy. This chapter starts with introducing basic knowledge for each technique as well as how it is implemented. The general knowledge for APT characterization, including sample preparation, parameter selection, and data reconstruction is included. For STEM, the basics of Scanning Transmission Electron Microscopy is briefly described. Implemented imaging, and spectroscopy techniques are then discussed.

2.1 Overview of Local Electro Atom Probe(LEAP)

Atom Probe Tomography provides the 3D composition distribution through evaporating atoms/ions successively off the surface. Ion clusters are subjected to ionization from the apex of the needle-shape specimen and projected to the detector. It is set up in an ultra-high vacuum chamber with chamber pressure about 10^{-10} Torr. The needle shape specimen is mounted on a stage with precise position control. The stage is also equipped with cryogenic temperature control; the tip temperature can be lowered to 20 K to reduce migration and noise. A DC, high voltage power supply is connected to the specimen for the required electrostatic field. A beam of pulsed laser is focused onto the tip by using in-vacuum laser control and the spot size is minimized. The counter electrode is setup right opposite of the specimen for detection. The detailed setup is shown in Figure 2-1.

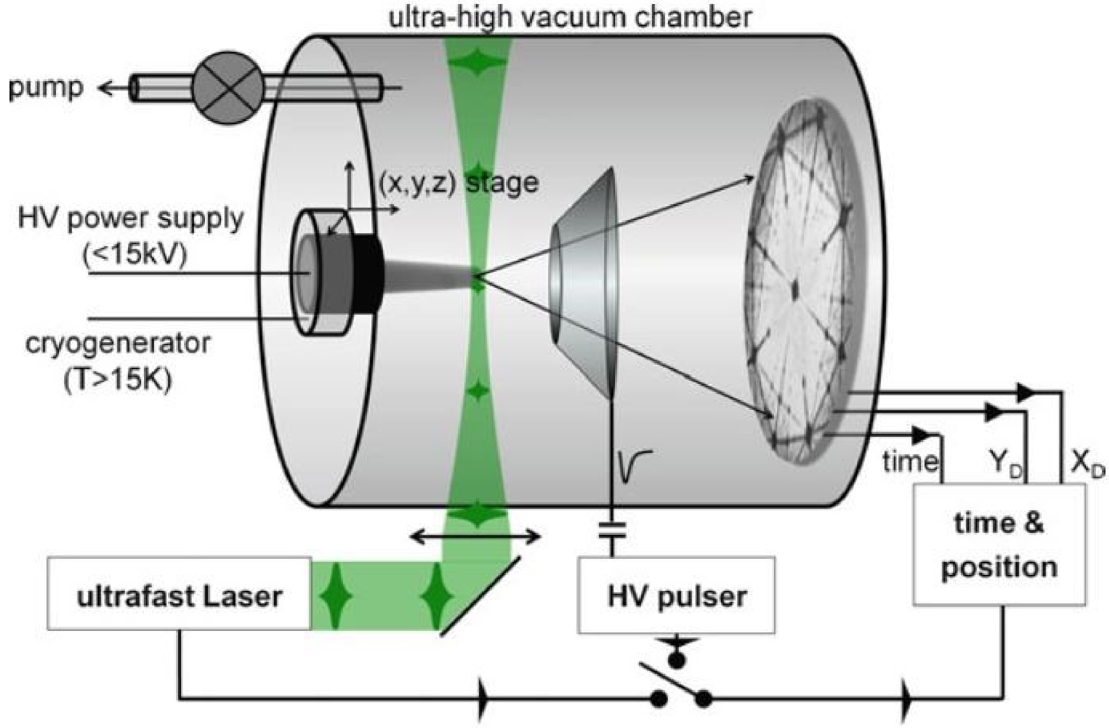

Figure 2-1. Schematic of Atom Probe analysis chamber setup [1]

A mass to charge spectrum is generated based on each ion cluster's time of flight. Combining both the mass spectrum and the 2D detector hit events, a 3D compositional distribution can be reconstructed. To ionize and evaporate atoms, Atom Probe requires the sharp needle-shaped specimen with an end radius smaller than 100 nm. [1] Most of the Atom Probe studies treat the tip as a truncated cone with a hemispherical cap. The half angle at the apex of the cone shape is defined as shank angle. The radius of the hemisphere is the radius of curvature of the tip (R). The electric field of the modeled specimen tip, F, with the curvature of radius of R and under high voltage V, can be described as:

$$\mathrm{F} = \frac{V}{k_f R}$$

Where k_f is referred as the field factor. The field factor is mainly affected by the radius of curvature and the overall shape of the specimen [2]. Assuming the electric field to evaporate certain species is a constant value, atoms that sits on the specimen with a smaller radius of curvature would get ionized at lower voltage.

It is possible to assist ion evaporation off the atom probe specimen with a focused laser beam. The increase in the thermal agitation of the surface atoms provokes field evaporation. As the heat propagates through the apex, the surface quenches. Therefore, laser pulsing is also referred to as "thermal pulsing". [1]Because of the poor conductivity of semiconductor materials, it is recommended to use the laser pulsing mode, especially for wide bandgap material. In most experiments, the energy of the laser pulses is kept constant throughout the experiment. The illumination parameter of the pulse laser is defined here as energy(J).

2.1.1 Sample Preparation

As stated before, the electrostatic field on the specimen is largely determined by the shank angle and the tip shape. Hence specimen preparation is important to acquire a good data set. The specimen preparation for semiconductor nanostructure usually falls under one of two categories: direct growth on the APT post or FIB/SEM dual beam lift-out. The direct growth method is only suitable for bottom-up grown nanowires, and is described in details by Perea et al. .[3]

All specimen prepared for this work use the FIB/SEM dual beam lift-out method. This method is chosen because of its advantage of making site specific specimens, which is crucial for complex embedded layer structures and semiconductor devices. Miller et al. have devoted a section of his book chapter to discuss detailed steps for APT specimen preparation using FIB. [4,5] For this study, only perpendicular orientations specimen extraction is applied to study the multilayer samples. In another word, the interfaces between multiple layers are perpendicular to the orientation of the apex of the needle shape specimen.

The sample is prepared using the V, or total release method [6] to lift out a wedge in the first step. Then the long wedge is separated into individual pieces and attached to a pre-sharpened multi-tip coupon. The usage of pre-manufactured microtip array coupon makes it easier to lift out material and shape it for APT measurement [7]. The sample preparation process is illustrated in Figure 2-2. At this step, high voltage and beam current (30kV, 2.5 nA) is used to minimize the required time.

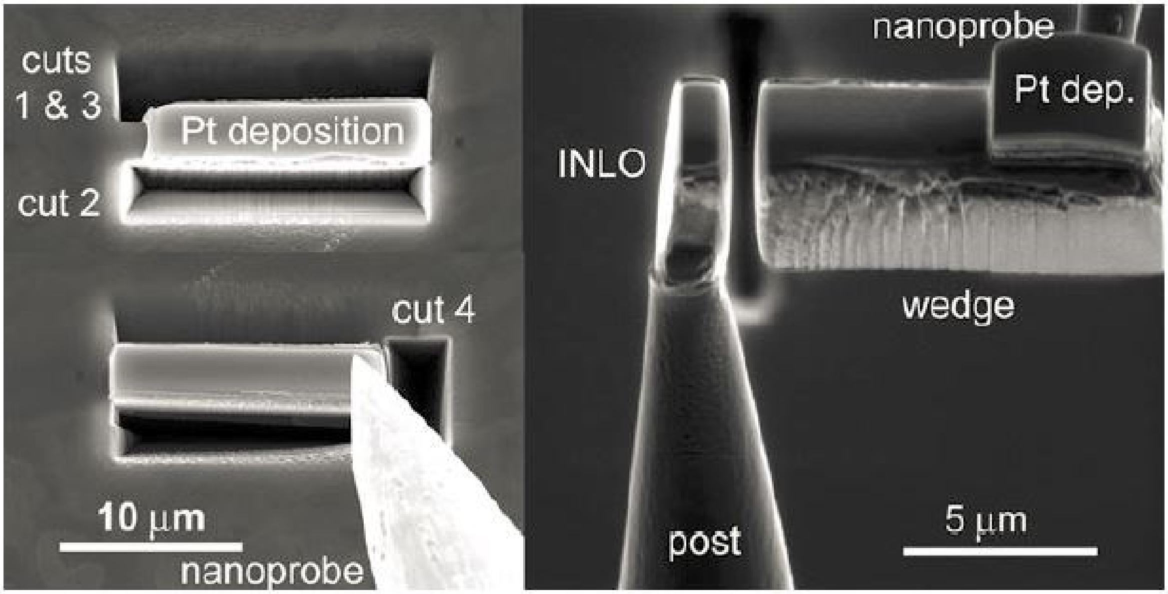

Figure 2-2. The V, total release method of APT sample preparation [8]

The next step is making the specimen into needle shape using annular milling. For semiconductor materials, the most common damage that can be introduced in the sample preparation step is the Ga damage. To prevent the penetration of Ga ions with specimen [9], low voltage and current (5kV, 0.12 nA- 4 pA) are used to sharpen the specimen in annular milling. Ga penetration or implantation has been reported to cause a variety of issues for Atom Probe Tomography results including distorted stoichiometry, interface mixing [10], and precipitation dissolution. [11] Therefore, even with a protective Pt capping layer, it is best practice to ① bury the region/layer of interest underneath a thin capping layer of similar material. For example, the GaSb quantum dots are capped with ~50 nm of GaAs. ② use stream file milling program on the Dual Beam FIB/SEM under which the apex is subjected to minimum Ga implantation.

2.1.2 Parameters Selection for Atom Probe Tomography

Several parameters can be adjusted to get the most optimal result depending on the nanostructure and the material: the pulsing mode and rate, the base temperature, and laser pulse power. The electric field required to evaporate atoms from the specimen is largely determined by base temperature and surface shape [1].

For semiconductor materials, it is known that the laser pulse energy, laser pulse frequency, and specimen base temperature could affect the compositional results. [12, 13] The effect of specimen base temperature often correlated with laser pulse energy. For the purpose to reduce noise and dopant drifting, the base temperature should be kept low. [14] The picosecond laser pulse would induce a momentary increment of the apex temperature. It is desirable to apply high enough pulse such that field evaporation occurs during the pulse only, while keeping the DC voltage low enough such that there is no evaporation between laser pulses. [15] When running a specimen, it is important to keep the correct III to V ratio, that is,1:1. It has been reported using a small pulse energy can give correct III:V ratio. [16] Thereby, the base temperature is kept around 25 K, and the laser pulse energy is kept at ~0.2 pJ. The pulse frequency is another parameter that required adjustment. When having large ions, it may be necessary to bring the pulse rate down to detect group V ion clusters. [17] Too high a pulse rate would leave not enough time for the ions to travel to the detector. Also, it is noticed that a high pulse rate can induce heat to build up on the surface of the specimen and melt the material. [1] In practice, the pulse rate for a specimen that contains Sb and Bi is usually set at 125 kHz.

Wide bandgap nanostructures (GaN, AlGaN, etc.) are more prone to composition bias. [16] Though the ideal case will be a perfect 1 to 1 III-V ratio, APT experiments usually result in 55:45 III-V ratio in practice. For the latest Cameca LEAP 5000XHR, it is possible to set up a constant evaporation field and let the software self-adjust the laser pulse energy. It is reported at T = 40K, an average stoichiometric can be achieved with an effective surface field ~24.3V/nm. [16]

2.1.3 Data Reconstruction

APT data are constructed using CAMECA's proprietary IVAS software. Mass spectra of (In)GaAs [18, 3], GaSb [17,19], and GaN [16] nanostructures show that semiconductor materials are more likely to have ion clusters , X_n, during evaporation. A mass spectrum of GaAs is shown below (Figure 2-3). Cluster sizes up to As_6 was observed. [20] Besides homonuclear group-V cluster ions, heteronuclear clusters of III-V elements are also reported, and the fraction of ion cluster can be affected by experiment conditions. [19]

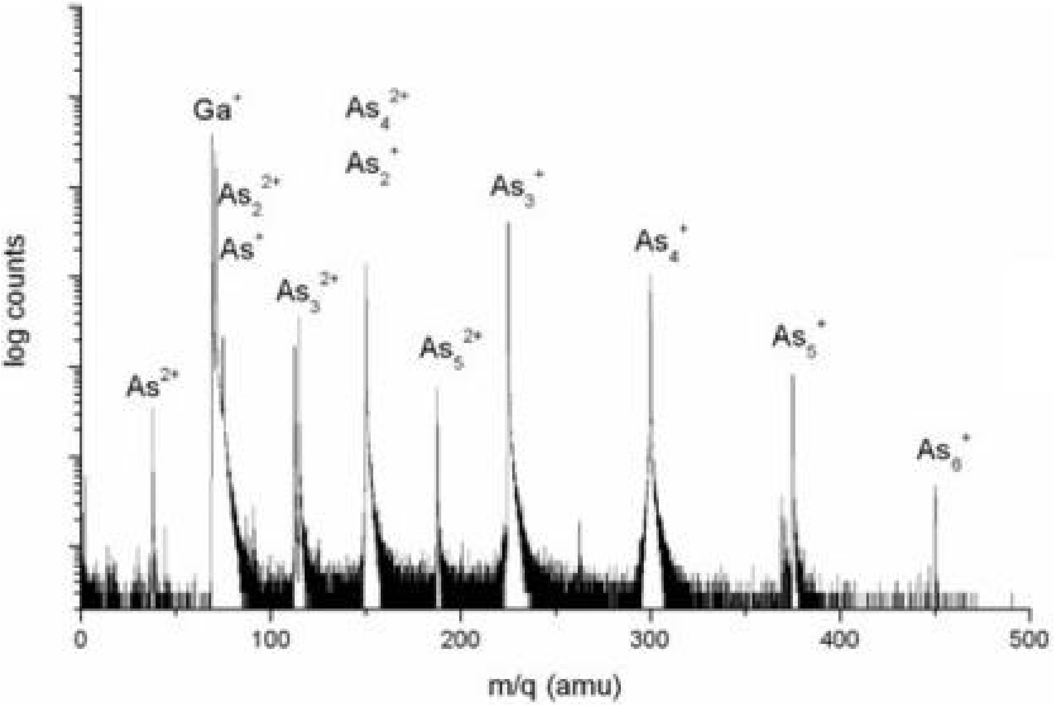

Figure 2-3. GaAs mass spectra using laser pulsed atom probe tomography[20]

The formation mechanism for these cluster ions is not well understood. Some researchers believed it is a temperature mediated process[21, 22], while others believe it is the deep penetration of electric field that induces more than just outermost atoms to evaporate. Larger agglomerates can also detach directly from the surface. The presence of heavy cluster ions in pulsed laser atom probe (PLAP) data has several consequences affecting the data accuracy, including mass peak overlaps and distortion on data accuracy (both chemical and spatial). [23]

Working with a known nanostructure is helpful for data reconstruction. It is important to estimate the reconstruction parameters as accurately as possible. Two main parameters that can be adjusted are field factor k_f and image compression factor (ICF) ξ. For wide band gap semiconductor nanostructures, it might be best to cut a cylindrical region of interest with uniform cross sectional total ion density to eliminate composition distortion near the edge.

2.2 Scanning Transmission Electron Microscopy

Scanning Transmission Electron Microscopy has been identified as a potent tool in atomic level material characterization. [24] High energy electron beam is converged into a focused spot and raster through the whole area of examination. The electrons that have been elastically scattered have a large deflection angle, and hence the contrast in high angle annular dark field (HAADF) images can be attributed mostly to “Z contrast”. [25, 26] Other imaging techniques like Annular Dark Field (ADF) and Bright Field (BF) imaging are also commonly used.

Elemental composition analysis can be done on STEM through both Energy-dispersive X-ray spectroscopy (EDS) and Electron Energy Loss Spectrum (EELS). EDS is the main elemental composition mapping technique used in this work for its easiness. The high-energy electron beam is capable of exciting an electron in an inner shell, ejecting it from the shell and creating an electron hole. The hole will then be filled with an electron from an outer, higher-energy shell, while the difference in energy between the two shells may be released as an X-ray. The energy -dispersive spectrometer would pick up the signal of the number and the energy of X-rays emitted. Since the characteristic energies are unique for every element, EDS can measure the elemental composition of the specimen. EELS is another integrated compositional profiling technique used in this work. When the specimen is exposed to a beam of electrons with a known and narrow range of energies, some of the electrons would lose energy and slightly deflected due to inelastic scattering. The electron spectrometer can measure the amount of energy loss. By interpreting the energy loss spectrum, EELS is capable of measuring atomic composition, chemical bonding, valence and conduction band electronic properties, and surface properties. [27]

2.2.1 Specimen Preparation for STEM

There are many ways to prepare a TEM specimen: traditional hand grinding, FIB lift-out, scratch off and disperse method. The general goal is to make an electron transparent specimen. Ideally, it is uniformly thin and should be representative of the nanostructure. The traditional hand grinding method is used when the material is sensitive to Ga damage, such as GaSb. The FIB lift-out method is the most frequently used method, because it does not require cleavage of the sample to prepare a cross sectional TEM specimen. The scratch off and disperse method is only be used for nanowire samples. However, the scratch-off method is not applicable if the interface between nanowires and the substrate needs to be imaged. The following section will describe FIB lift-out method and scratch-off and disperse method since these are the two major methods for sample preparation in this thesis.

2.2.1.1 FIB Lift-out Method

FIB "lift-out" is preferred for highly structured samples, frequently used in quantum wells and quantum dot samples. Detailed procedures of regular FIB lift-out can be found in the Williams and Carter's book. [28] The process requires a thin slab of specimen being lifted out from the sample using the Omniprobe. The thin slab is then attached to the TEM grid with Pt deposition. Low voltage and current should be used at the final thinning step to prevent Ga damage. To prepare a good nanowire TEM specimen with FIB lift-out method, the nanowire sample needs to be backed filled. Figure 2-4 illustrates detailed steps to back fill a nanowire sample and prepare it for FIB lift out.

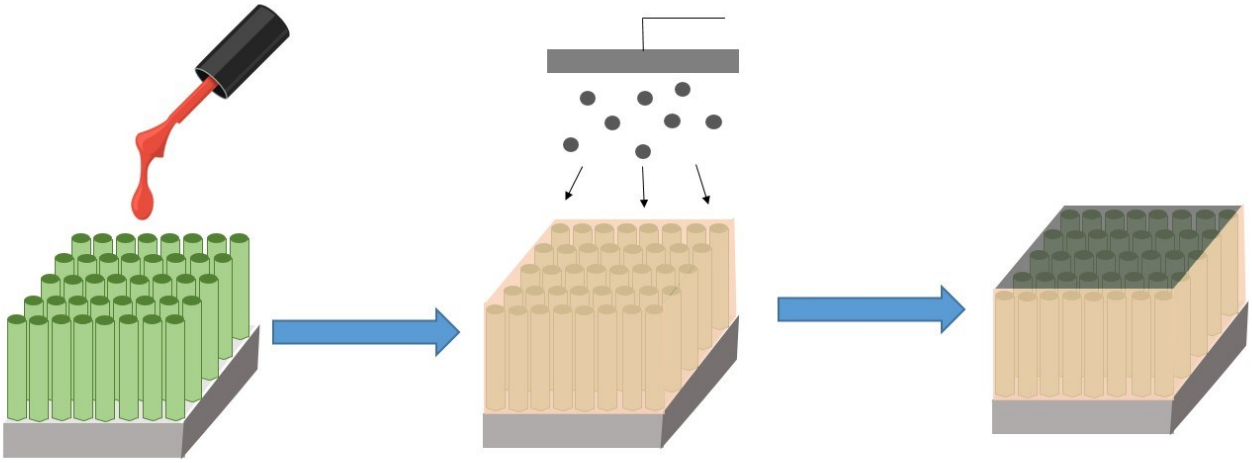

Figure 2-4. Illustration of how to back fill a nanowire sample

As shown above, drip a small drop of M-bond epoxy onto the nanowire sample. The sample can be either heated on the heat plate for 20 minutes, or left overnight for the epoxy to cure. A thin layer of carbon needs to be coated on top of the surface to make it conductive. The coating is done by the sputter coater, configured to evaporate carbon using carbon fiber inserts. After this step, the sample can be taken into SEM/FIB dual beam to do a TEM lift-out. Since M-bond is transparent under TEM if thin enough, a regular TEM lift-out procedure can be done easily with the shape of the nanowires fully preserved.

Figure 2-5 shows the SEM image of one of the lift-out nanowire specimen during thinning process. Each layer is labeled: the protective Pt layer is on the topmost and nanowires are all encapsulated in the back-filled M-bond Epoxy. An ideal piece of TEM sample would be 4-5 micron in height, capturing ~ 1 μm M-bond in height plus 2-3 micron tall of Si- substrate.

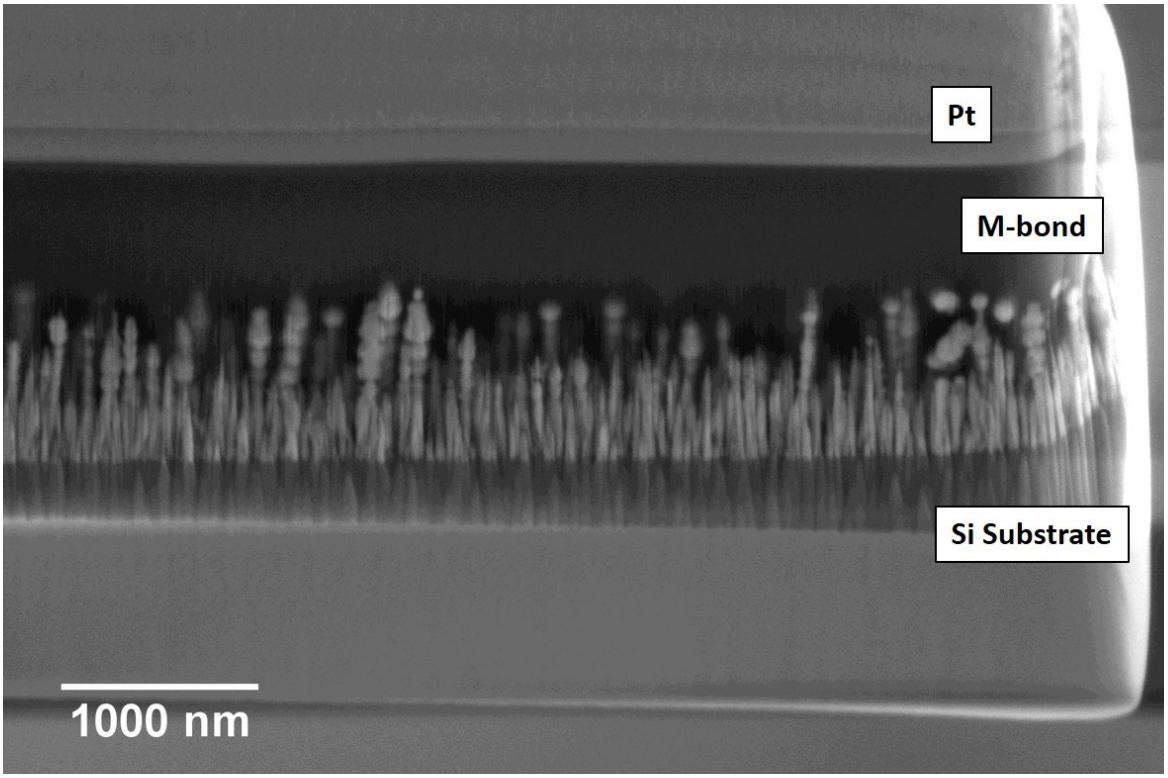

Figure 2-5. An SEM image of FIB lift-out slab

2.2.1.2 Scratch-off Method

The scratch-off method targets specifically for nanowire sample with the goal of imaging individual nanowire. Some nanowires can be dispersed easily by a small amount of liquid, while others might require being put in a centrifuge tube and sonic bathed. Figure 2-6 illustrates how the scratch-off method is realized nanowires that can be easily dispersed. A new syringe is first filled with water or water/methanol solution. First, apply pressure and scratch the nanowire sample with the syringe. Then, move the syringe on top of a lacy carbon film TEM grid held by tweezers and push the syringe slowly till a drop of the solution rolls off. The solution would wash off the nanowires accumulated on the syringe head. Hence nanowires are dispersed on the lacy carbon TEM grid. An infrared heat lamp is then used to evaporate the residual liquid. These steps can be repeated until the desired number of nanowires have been dispersed on the grid. The sample is ready to be imaged after the grid is completely dry. This method requires a new syringe/syringe head for each sample.

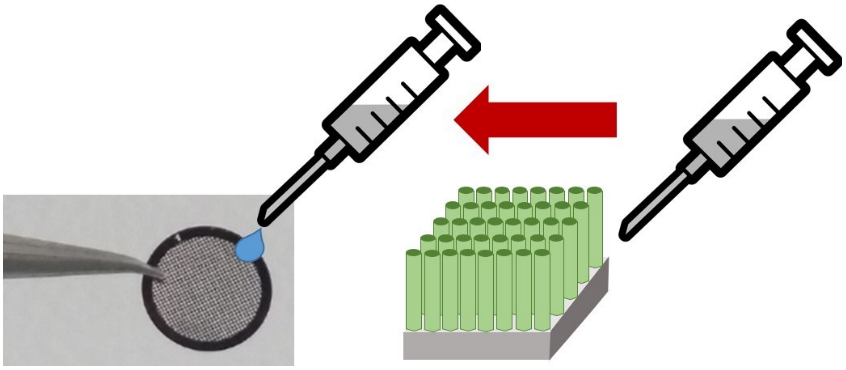

Figure 2-6. Illustrations of scratch-off method for TEM sample prep using a syringe.

2.2.2 STEM Imaging and Spectroscopy

STEM has been brought to a new level with latest aberration correction techniques, and has a strong advantage of simultaneous imaging and spectroscopy collection. For this work, the two main techniques that have been utilized are High Angle Annular Dark Field(HAADF) imaging and Energetic Dispersive X-ray Spectroscopy(EDS).

2.2.2.1 HAADF Imaging

The nature of HAADF imaging is particularly attractive in studying semiconductor nanomaterials in that it produces an image contrast strongly depends on atomic number(Z) and not being overly sensitive to either specimen thickness or to aberrations of lens after specimen. These images are often amenable to direct and visual interpretation, even allow us to observe directly heavy dopant atoms within crystals.[29, 30] Another appealing feature for STEM is the simultaneous bright field(BF) and HAADF images. The pixel-to-pixel correlation provides different but complementary views of the same region. [31]

However, it needs to be pointed out that some semiconductor materials are sensitive to the finely focused electron beam. It has been shown before that exposure to electron beam would induce inhomogeneous strain for InGaN quantum wells [32], and AlGaAs quantum well structure [33]. In other cases, hole drilling might happen when the current applied is intense enough. [27] Too high a beam energy or beam current density can be harmful to the specimen.

2.2.2.2 Energy Dispersive Spectroscopy(EDS)

X-ray analysis in STEM is a robust and reliable method to characterize elemental composition. The spatial resolution of EDS largely depends on the incident probe dimension and its interaction with the electron-transparent thin sample. The X-ray signal intensity varies with angle of incident and the excitation volume of the electron beam. As mentioned by Williams and Carter's book, it is important to ensure high enough X-ray counts. [28] Increasing spot size of the electron beam as well as tilting the sample towards the X-ray detector can improve the low counts situation. The X-ray mapping technique includes three analysis modes: point, line, and area mapping. Results collected using line mode is referred as "line profile", and the ones collected using area mode is referred as "maps". The resolution of the EDS analysis can be affected by TEM sample thickness and microscope column configuration.[28, 29] If properly configured, it is possible to achieve atomic resolution EDS mapping. In practice, it is not always the case that the microscope will achieve the highest resolution. Hence for small features of interest (~1-2nm), it is a better choice using Electron Energy Loss Spectroscopy(EELS).

Conducting quantitative x-ray analysis can determine local compositions of thin specimens. The traditional way of quantitative X-ray analysis uses the Cliff-Lorimer ratio method. [34] More recently, an improved quantitative procedure has been developed to overcome some of the limitations of the Cliff-Lorimer ratio. [35, 36]

2.3 References

1. Gault, B., Moody, M. P., Cairney, J. M. & Ringer, S. P. *Atom Probe Microscopy*. **160,** (2012).
2. Gipson, G. S. & Eaton, H. C. The electric field distribution in the field ion microscope as a function of specimen shank. *J. Appl. Phys.* **51,** 5537–5539 (1980).
3. Perea, D. E. *et al.* Three-dimensional nanoscale composition mapping of semiconductor nanowires. *Nano Lett.* **6,** 181–185 (2006).
4. Miller, M. K. & Forbes, R. G. in *Atom-Probe Tomography* 189–228 (Springer US, 2014). doi:10.1007/978-1-4899-7430-3_4
5. Martin, A. Manipulating Quantum Dot Nanostructures for Photonic and Photovoltaic Applications by. (2013).
6. Thompson, K., Larson, D. J. & Ulfig, R. M. Pre-sharpened and Flat-top Microtip Coupons: a Quantitative Comparison for Atom-Probe Analysis Studies. *Microsc. Microanal.* **11,** 2004–2005 (2005).
7. Larson, D. J. *et al.* Local Electrode Atom Probe Tomography A User's Guide., 2013.
8. Miller, M. K. *et al. Atom Probe Microscopy: The Local Electrode Atom Probe*. *Text* **10,** (2013).
9. Rubanov, S. & Munroe, P. R. Damage in III – V Compounds during Focused Ion Beam Milling. *Microsc. Microanal.* **11,** 446–455 (2005).
10. Larson, D. J., Foord, D. T., Petford-Long, a. K., Cerezo, a. & Smith, G. D. W. Focused ion-beam specimen preparation for atom probe field-ion microscopy characterization of multilayer film structures. *Nanotechnology* **10,** 45–50 (1999).
11. Miller, M. K. & Forbes, R. G. *Atom-probe tomography: The local electrode atom probe. Atom-Probe Tomography: The Local Electrode Atom Probe* **9781489974,** (2014).
12. Hashizume, T., Hasegawa, Y., Kobayashi, A. & Sakurai, T. Atom-probe investigation of

III-V semiconductors: Comparison of voltage-pulse and laser-pulse modes. *Rev. Sci. Instrum.* **57,** 1378–1380 (1986).

13. Agrawal, R., Bernal, R. A., Isheim, D. & Espinosa, H. D. Characterizing Atomic Composition and Dopant Distribution in in Wide Band Gap Semiconductor Nanowires Using Laser-Assisted Atom Probe Tomography. *J. Phys. Chem. C* 17688–17694 (2011).

14. Cerezo, A., Clifton, P. H., Gomberg, A. & Smith, G. D. W. Aspects of the performance of a femtosecond laser-pulsed 3-dimensional atom probe. *Ultramicroscopy* **107,** 720–725 (2007).

15. Shariq, A. *et al.* Investigations of field-evaporated end forms in voltage- and laser-pulsed atom probe tomography. *Ultramicroscopy* **109,** 472–479 (2009).

16. Mancini, L. *et al.* Composition of Wide Bandgap Semiconductor Materials and Nanostructures Measured by Atom Probe Tomography and Its Dependence on the Surface Electric Field Franc o Jean-Franc o. (2014).

17. Müller, M., Smith, G. D. W., Gault, B. & Grovenor, C. R. M. Compositional nonuniformities in pulsed laser atom probe tomography analysis of compound semiconductors. *J. Appl. Phys.* **111,** (2012).

18. Du, S. *et al.* Quantitative dopant distributions in GaAs nanowires using atom probe tomography. (2013). doi:10.1016/j.ultramic.2013.02.012

19. Müller, M., Saxey, D. W., Smith, G. D. W. & Gault, B. Some aspects of the field evaporation behaviour of GaSb. *Ultramicroscopy* **111,** 487–92 (2011).

20. Gorman, B. P., Norman, A. G. & Yan, Y. M icroscopy M icroanalysis Atom Probe Analysis of III – V and Si-Based Semiconductor Photovoltaic Structures. 493–502 (2007).

21. Grovenor, C. R. M., Cerezo, A., Liddle, J. A. & Smith, G. D. W. Pulsed Laser Atom Probe Analysis of Semiconductor-Materials. *Inst. Phys. Conf. Ser.* **141,** 665–674 (1987).

22. Drachsel, W., Jentsch, T., Gingerich, K. A. & Block, J. H. Observation of doubly charged triatomic cluster ions in field evaporation. *Surf. Sci.* **156,** 173–182 (1985).

23. Müller, M., Gault, B., Smith, G. D. W. & Grovenor, C. R. M. Accuracy of pulsed laser

atom probe tomography for compound semiconductor analysis. *J. Phys. Conf. Ser.* **326,** 12031 (2011).

24. Muller, D. a. Structure and bonding at the atomic scale by scanning transmission electron microscopy. *Nat. Mater.* **8,** 263–270 (2009).

25. Howie, A. Image Contrast And Localized Signal Selection Techniques. *J. Microsc.* **117,** 11–23 (1979).

26. Williams, D. B. & Barry Carter, C. *Transmission Electron Microscopy. Diffraction, Imaging, Spectroscopy*. (2009). doi:10.1007/978-3-319-26651-0

27. Egerton, R. F., Li, P. & Malac, M. Radiation damage in the TEM and SEM. *Micron* **35,** 399–409 (2004).

28. Williams, D. B. & Carter, C. B. in *Transmission Electron Microscopy* 3–22 (Springer US, 2009). doi:10.1007/978-0-387-76501-3_1

29. Nellist, P. D. & Pennycook, S. J. *The principles and interpretation of annular dark-field Z-contrast imaging. Advances in Imaging and Electron Physics* **113,** (2000).

30. Tanaka, N. *Scanning Transmission Electron Microscopy of Nanomaterials*. (IMPERIAL COLLEGE PRESS, 2014). doi:10.1142/p807

31. Pennycook, S. J. in *Transmission Electron Microscopy* 283–342 (Springer International Publishing, 2016). doi:10.1007/978-3-319-26651-0_11

32. Smeeton, T. M., Kappers, M. J., Barnard, J. S., Vickers, M. E. & Humphreys, C. J. Electron-beam-induced strain within InGaN quantum wells: False indium ‘cluster’ detection in the transmission electron microscope. *Appl. Phys. Lett.* **83,** 5419–5421 (2003).

33. Tanaka, T., Kawanishi, H. & Ishikawa, T. Photoluminescence study of electron beam-induced damage in GaAs/AIGaAs quantum well structures.

34. Cliff, G. & Lorimer, G. W. The quantitative analysis of thin specimens. *J. Microsc.* **103,** 203–207 (1975).

35. Watanabe, M., Horita, Z. & Nemoto, M. Absorption correction and thickness determination using the ζ factor in quantitative X-ray microanalysis. *Ultramicroscopy* **65,** 187–198 (1996).

36. WATANABE, M. & WILLIAMS, D. B. The quantitative analysis of thin specimens: a review of progress from the Cliff-Lorimer to the new zeta-factor methods. *J. Microsc.* **221,** 89–109 (2006).

Part I APT vs. STEM in 2D layers and Buried QD Nanostructures

Chapter 3 APT vs. STEM on 2D Layer Semiconductor Nanostructures [*]

Pulsed laser atom probe(PLAP) has made it possible to map composition for semiconductor nanostructures. Another powerful tool to characterize these semiconductor nanostructures is STEM. This chapter is dedicated to comparing the data gathered from APT and STEM on 2D layer semiconductor nanostructures. InGaN bulk and thin layers, as well as GaAsBi bulk layer nanostructures, are examined. It demonstrates how results from these two techniques are utilized in answering some of the unsolved questions in III-V semiconductor nanostructures. This chapter will only focus on the application and related issue for semiconductor 2D layers.

---

[*] This chapter is based on the publication “High performance red-emitting multiple layer InGaN/GaN quantum dot lasers”, (Frost, et al., Japanese Journal of Applied Physics) and “Droplet induced compositional inhomogeneities in GaAsBi”, (C. R Tait, et al., Applied Physics Letter) and has been reformatted to departmental guidelines

3.1 InGaN Bulk and Thin layer

InGaN has been studied as an optoelectronic material with great potential. However, it is notorious for phase separation. Ho and Stringfellow predicted that zinc blende $In_{0.2}Ga_{0.8}N$ is already within the spinode. [1] More recently, Karpov calculated the phase diagram of biaxially strained InGaN, and suggested a spinode shifted to much lower temperatures and higher Indium contents than what is predicted before (Figure 3-1). [2] InGaN QWs are able to have Indium concentration up to 50% without spinodal decomposition.

The first APT nitride quantum wells nanostructure data was recorded by Galtrey et al. [3] on blue emitting Multiple Quantum Well (MQW) nanostructure. The available data sets suggest Indium composition observed does not significantly deviates from random. Despite that their APT data suggesting there is no clustering, several papers report seeing Indium clustering, utilizing strain mapping with High Resolution TEM. [4,5] This discrepancy has resulted in controversy. It is possible that Galtry et al. did not observe Indium clustering because the structure they studied has only 15% Indium, and the quantum well structure is able to relieve the accommodate the lattice mismatch without clustering. Another possibility is Indium clustering happens depending on the growth condition used in each paper. Either low growth temperature or a high growth rate tend to result in inhomogeneous incorporation.

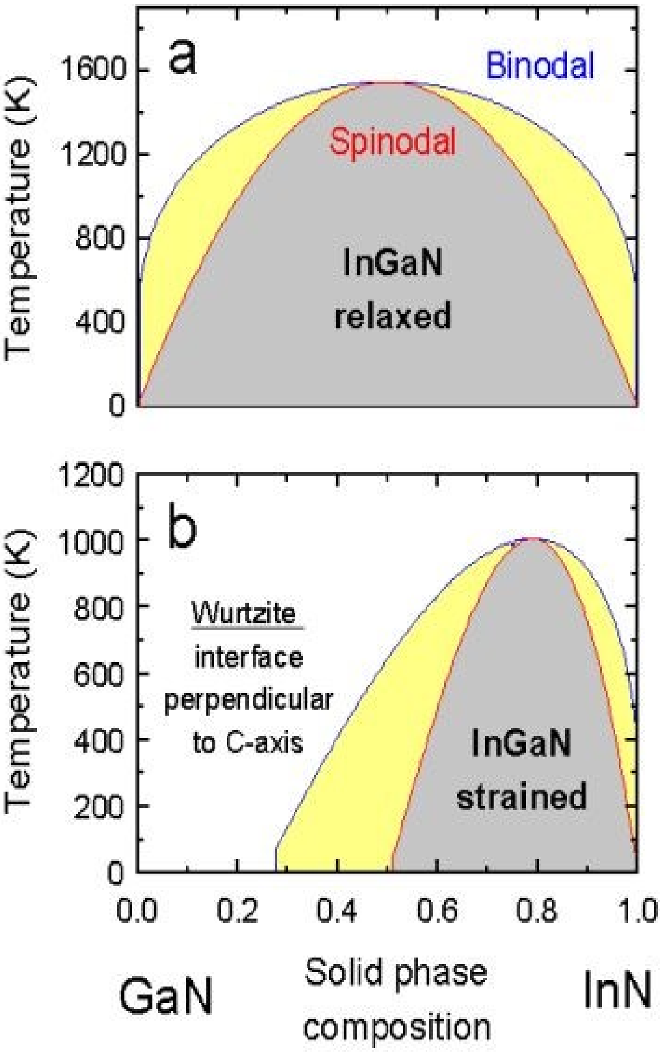

Figure 3-1. Temperature - composition phase diagram of InGaN alloy(a) Relaxed layer (b) Bi-axially strained InGaN layer. [20]

Three nitride samples are studied to understand the compositional inhomogeneities in InGaN nanostructures. A 30-nm thick bulk layer sample with nominal composition of $In_{0.15}Ga_{0.85}N$ is first investigated as a reference point. The InGaN bulk layer sample is grown using Metal-Organic Chemical Vapor Deposition (MOCVD) method on a c-plane sapphire substrate. For this sample, cross sectional TEM and APT are compared to quantify the interfacial broadening due to the instrument. Then both InGaN ultra-thin single and multiple layer samples are examined to study the compositional inhomogeneity issues both qualitatively and quantitively. Both ultra-thin layer samples are grown using MBE.

3.1.1 Compositional Inhomogeneity in InGaN bulk layer

The cross sectional TEM sample is prepared with a conventional FIB lift-out method. Figure 3-2 is the High Angle Annular Dark Field (HAADF) image of the film. The contrast is mainly due to atomic weight, in which case the $In_{0.15}Ga_{0.85}N$ should be brighter than the GaN substrate. The thickness measured by TEM image is ~25 nm thick. The atomic-resolution HAADF images suggest the interface is atomically abrupt.

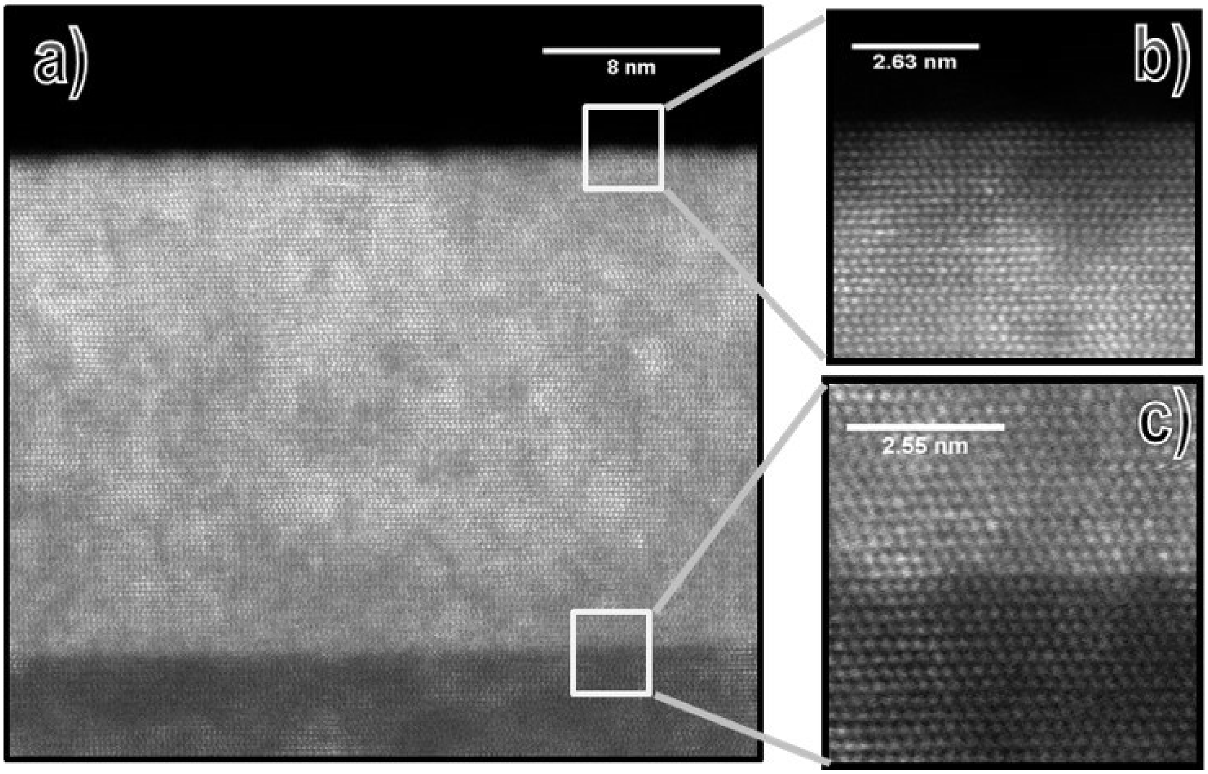

Figure 3-2. HAADF image of an In0.15Ga0.85N Bulk layer showing atomic abrupted interface between the substrate and the layer.

(In)GaN has non-uniform evaporation. The APT specimen is prepared with tip oriented at c-pole. A six-fold symmetry pattern can be observed when looking at the total ion density from the APT data. Figure 3-3 shows the two dimensional iso-density contour plot for InGaN bulk layer specimen. The iso-density plot indicates a lower density region at the center of apex while the outer ring has a higher density of ion. The density plot revealed the crystallographic pole and approximately 6-fold symmetry, which agrees with the stereographic projection along the (0001) direction of the wurtzite hexagonal crystal structure. Even though the sign of pole is clearly observed, lattice planes are not resolved in the reconstructions due to possible local rearrangement and laser mode heat dissipation. This iso-density feature is much different than the In isoconcentration plot. It is reported before that c-pole is the high field region for GaN. [6] Therefore, it is possible this non-uniform density during evaporation is caused by the c-pole.

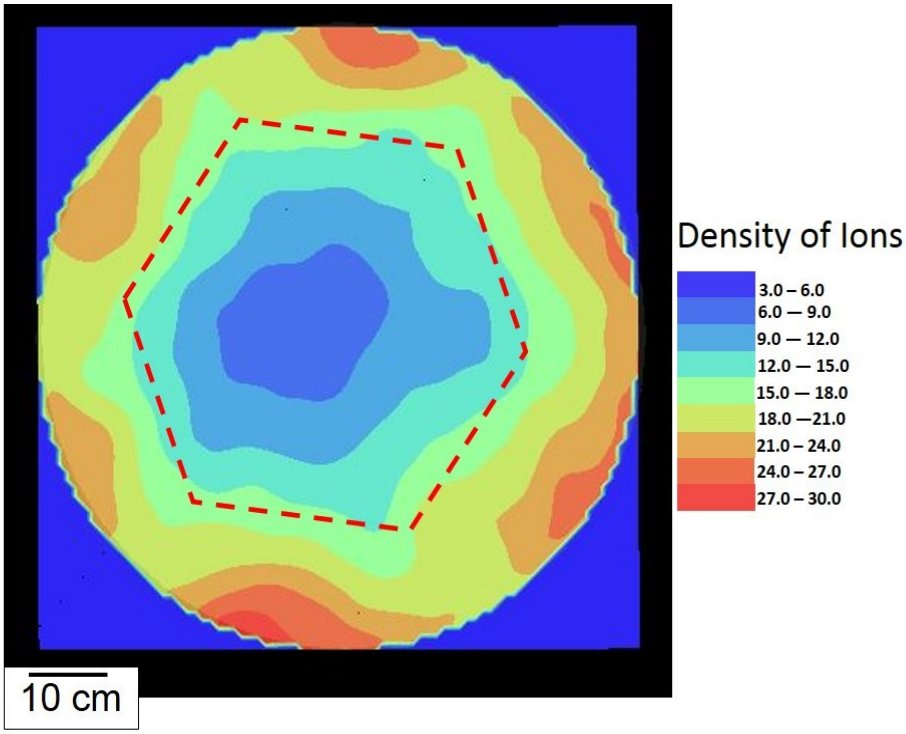

Figure 3-3.2D Iso-density plot for total ions from the (In)GaN sample, the six-fold symmetry pattern is indicated with dash line.

Figure 3-4 shows the Atom Probe reconstruction of one of the specimens for In$_{0.15}$Ga$_{0.85}$N bulk layer sample. Ga atoms are denoted in blue and Indium atoms are denoted in cyan. The reconstruction parameter is calibrated so that the InGaN layer thickness matches the observation from TEM. A cylindrical region of interest (ROI) with diameter of 30 nm and height of 20 nm is chosen perpendicular to the InGaN/GaN interface. The ROI is cut out from the data and the 1D concentration profile is shown in Figure 3-4(b), showing a fraction of Indium vs distance in nm. Although the TEM images indicate an atomically abrupt interface, the APT data show an interfacial thickness of ~1.5 nm. The discrepancy might be due to local rearrangement or the averaging on 1D concentration profile in IVAS. [7] The nominal concentration of this layer is 15% Indium and the concentration profile gives concentration of 17.0 ±0.7 %. The measured concentration is in good agreement with the nominal concentration.

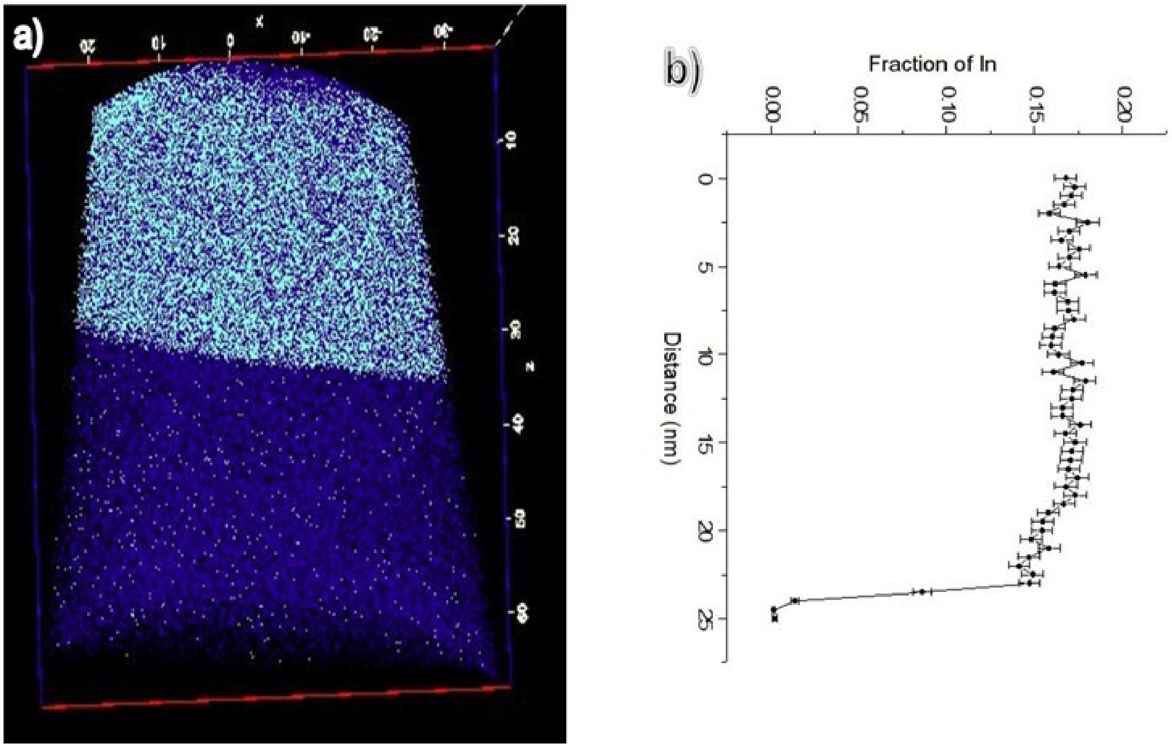

Figure 3-4. (a)Atom Probe Reconstruction of the In0.15Ga0.85N bulk layer with Indium(Cyan) and Ga(blue). (b) 1D concentration profile of Indium vs Distance(nm)

The in-plane compositional variation is shown in Figure 3-5. Two orthogonal lines across the center of the data set are also taken to see how much inhomogeneity is present. The line profiles give In concentration of 17.1 ± 1.7 atomic percentage and 17.2 ± 1.6 atomic percentage. The Indium concentration agrees with the 1D concentration profile along Z axis well, but with larger fluctuations. The larger variation in the orthogonal concentration can be contributed to a fewer number of atoms being accounted for (3 nm × 3 nm × 30 nm). Another artifact, caused by trajectory aberration, needs to be noticed here. The so-called *roll-up* effect is one of the main reasons for the large In concentration fluctuation. [8] This effect corresponds to a possible movement of the atoms moving onto the surface prior to its field evaporation and its flight, and the electric field can be discontinued due to the local geometry of the apex.

Figure 3-5 (b) is the frequency distribution of In. The frequency distribution is commonly used to detect phase separation or precipitation in a material. It starts with dividing the atoms in the volume of analysis into small blocks containing a fixed number of atoms. The histogram plots the total number of unit volumes containing a given composition of solute atoms. The simulated line shows the fitted line assuming a binomial distribution with In composition of 15%, the simulated line represents the composition variation from random alloy fluctuation. The experimental data from APT(red) agree well with simulated binomial distribution (black).

Moody et al. proposed using Pearson coefficient, μ, to describe clustering in APT data since the traditional χ^2 test for significance has a dependence on sample size. The value of χ^2 would increase with increasing number of blocks sampled [9], making it hard to compare directly between different data sets. The Pearson coefficient is calculated by: [10]

$$\mu = \sqrt{\frac{\chi^2}{N + \chi^2}}$$

This equation gives a value of μ between 0 and 1, independent of sample size N. A value close to 0 indicates a random distribution and 1 indicates a complete association in the occurrence of the solute atoms. It is possible to compare the degree of segregation among multiple data set. For the InGaN bulk layer data set, the Pearson coefficient is calculated to be 0.1 with a bin size of 100 atoms. Combined with Figure 3-5, the inhomogeneity observed here is probably due to random alloy fluctuation.

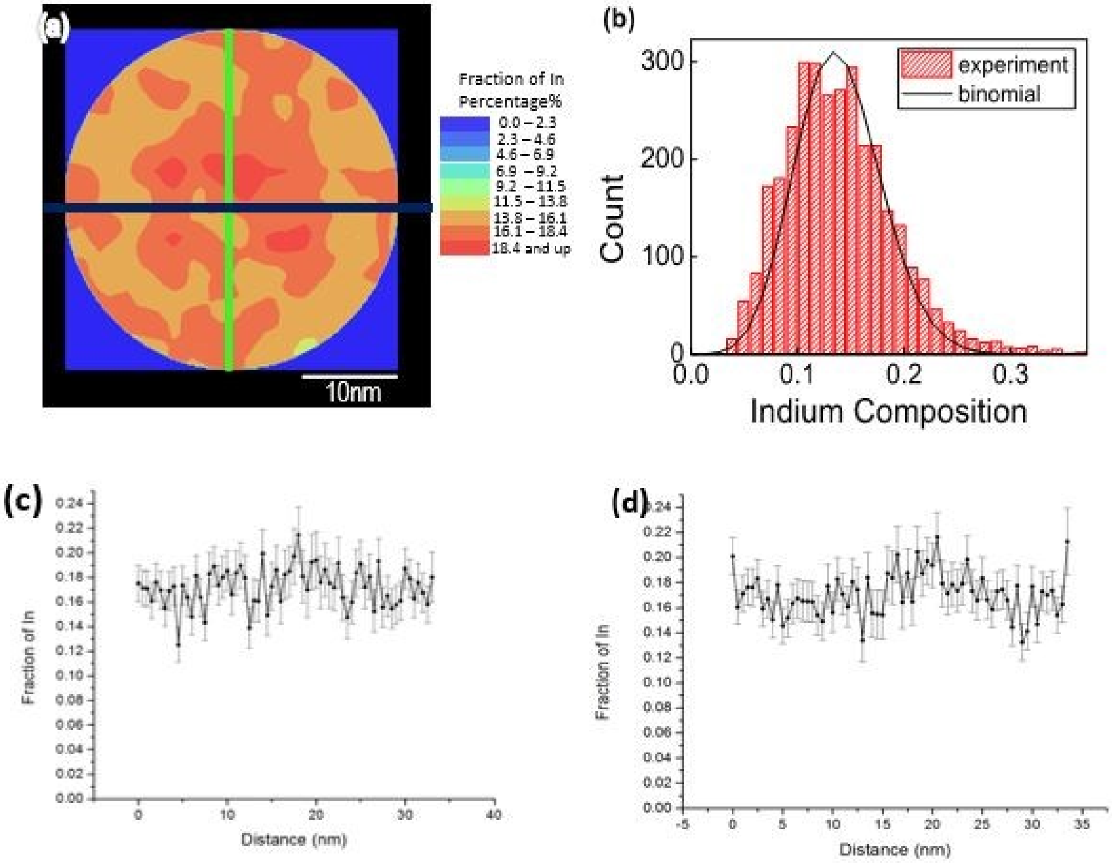

Figure 3-5. (a) 2D concentration contour plot of Indium in the bulk layer. (b) experimental concentration compared to the binomial distribution. (c) 1D concentration profile along the line(green) in (a). (d) 1D concentration profile along the line(blue) in (a)

In summary, InGaN bulk layer sample sets a good reference point for quantifying instrumental broadening. APT data shows a ~1.5 nm thick interface while STEM data suggest abrupt interface. Both STEM and APT data suggest the main compositional inhomogeneity within the bulk layer is attributed by random alloy fluctuation. The Pearson coefficient is found to be ~0.1.

3.1.2 Compositional Inhomogeneity InGaN Ultra-Thin Layers

Unlike InGaN bulk layer, the InGaN ultra-thin layer presents more inhomogeneity. The sample being examined is a thin layer of $In_{0.4}Ga_{0.6}N$ QD sample grown by MBE. Figure 3-6(a) shows the APT reconstruction of a typical specimen with Indium atoms denoted in red. One thin layer of In-rich InGaN thin layer can be clearly seen. Again, a cylindrical ROI is chosen perpendicular to the interface as much as possible. The 1D concentration profile along the Z axis of the cut-out region shows an asymmetric peak at the thin layer position, the Full Width Half Maximum (FWHM) is measured to be about 1 nm thick. The 2D iso-concentration contour plot is generated using a cylindrical ROI with diameter of 30 nm and height of 4 nm. Figure 3-6 (c) shows there is nano-size clustering in the layer. Since a bin size of 0.2 nm is used in the calculation, it is reasonable that a larger error will be observed. There are a few dot regions with diameter of 3-4 nm having In concentration up to 3.6%. The Pearson coefficient is measured to be 0.30, is considered high compared to low Pearson coefficient for other elements.

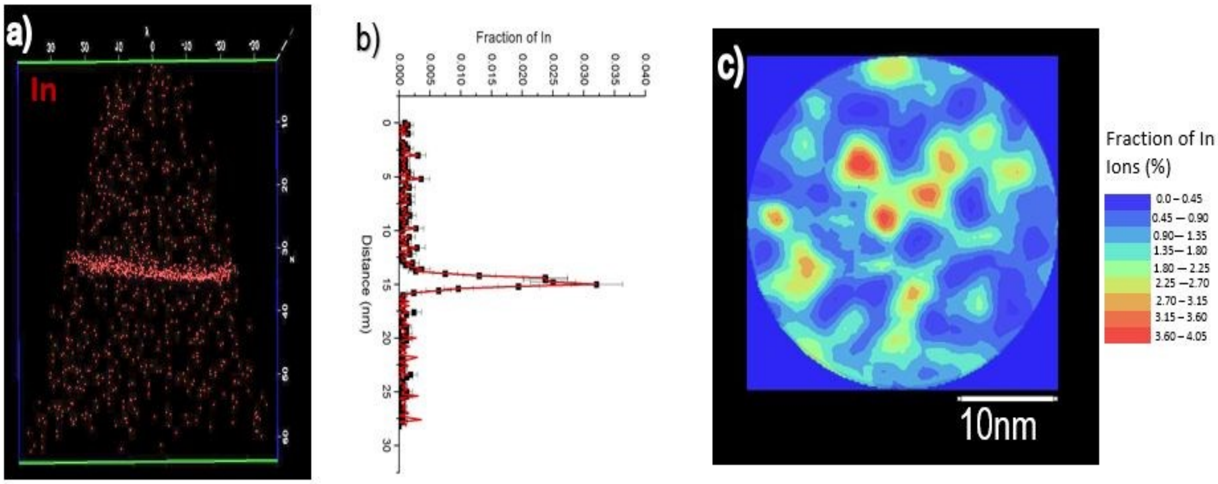

Figure 3-6. (a) APT reconstruction showing In(red) ultra-thin layer from x-z plane viewpoint. (b) The 1D concentration profile of fraction of In vs Distance(nm) (c) 2D iso-concentration contour plot of the fraction of Indium ions.

Next, a more complicated nanostructure is examined in APT with four $In_{0.4}Ga_{0.6}N$ QD wetting layers separated by a GaN barrier layer. HAADF TEM image and EDS mapping of a similar sample are taken to profile the QD composition. [11] Five layers of $In_{0.4}Ga_{0.6}N$ QD layers can be clearly seen (Figure 3-7(a)). On top of the GaN substrate, the first layer of InGaN QDs are grown on the smooth surface. The surface roughness increase as layers of QDs have been deposited. There is no clear sign that QDs align vertically during the growth. Figure 3-7(b) is the zoomed in image for one of the quantum dots, with growth direction indicated. The EDS spectrum showing only Indium composition and Ga composition. The height of the QDs is ~6 nm, and a line profile of 8 nm is collected. The line profile indicates a steep GaN to InGaN interface and a gradual InGaN to GaN interface. The highest In composition is ~40 %, which agrees with the InGaN QDs composition.

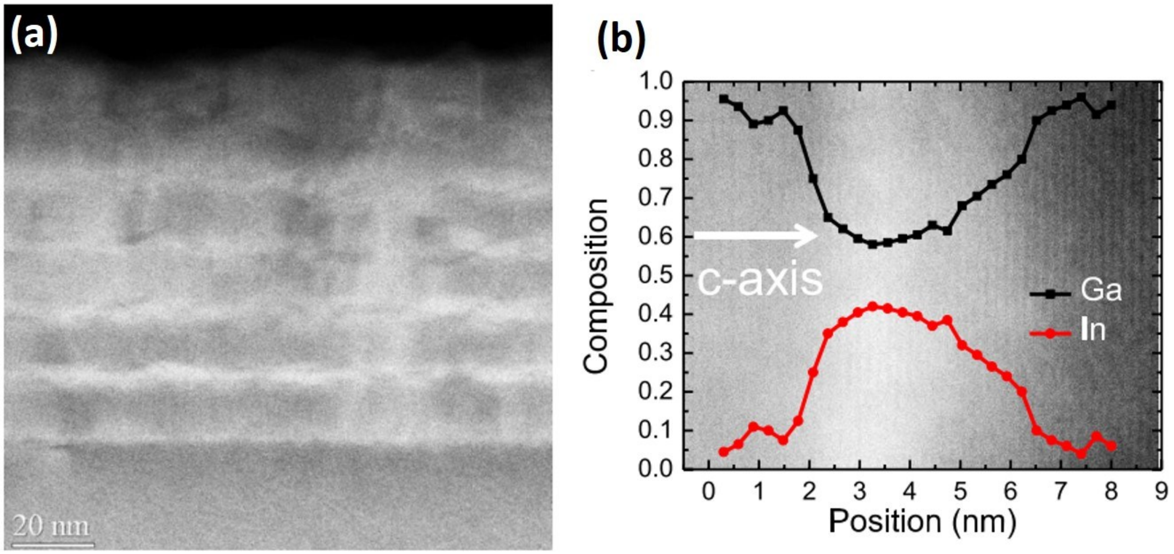

Figure 3-7. (a) Cross sectional HAADF TEM image taken from InGaN Quantum Dots sample (b) EDS line profile across one QD[11]

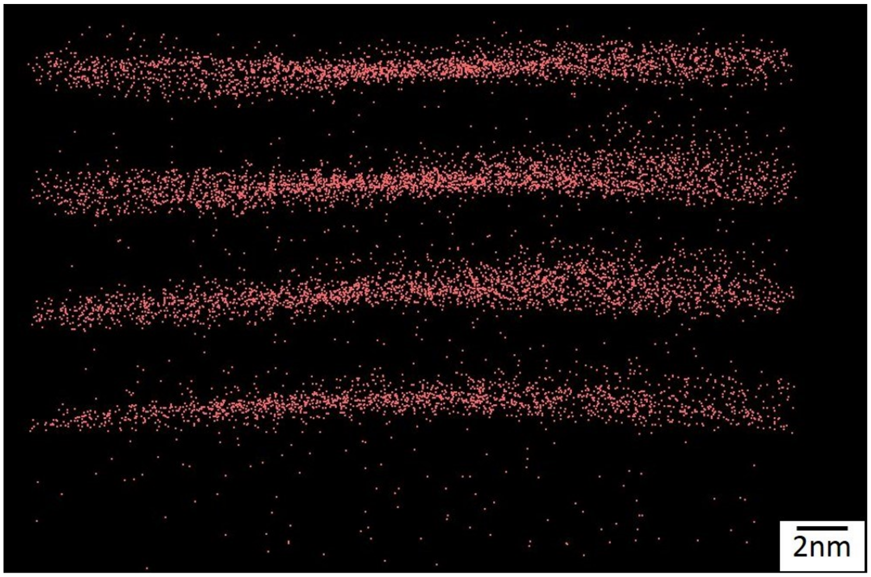

Figure 3-8. Edge-on view of 3D reconstruction of InGaN QD Sample, Indium is denoted by red.

.

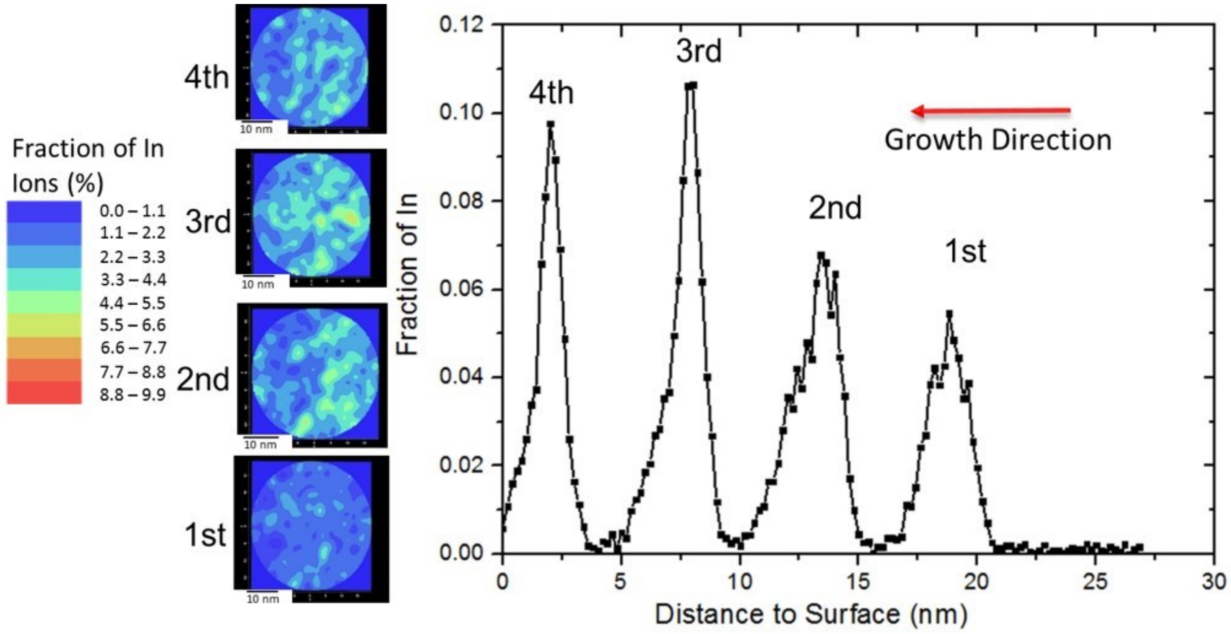

Figure 3-9. 1D In concentration profile along the growth direction with 2D iso-concentration contour plots of each layer on the left side

The APT reconstruction is shown in Figure 3-8, in which Indium atoms are denoted in red. Four layers of In-rich layers are clearly observed. Figure 3-9 shows the 2D iso-concentration contour plots of In as well as the In 1D concentration plot for the multilayer InGaN sample. The 1D concentration profile is generated using a much smaller cylindrical ROI with diameter of 10 nm and height of 27 nm. The Indium concentration decreases exponentially after reaching the peak value. The peak value for the 1st layer is 6% and the 2nd layer reaches 7%, the peak heights of the 3rd and 4th layer (~10%) are higher than the 1st and 2nd layer. However, it can also be seen that 1st and the 2nd peak has larger FWHM than the 3rd and 4th peaks

To analyze the In concentration quantitatively, the number of In atoms contained in each layer, namely the area underneath each peak, is calculated and projected onto the cross section of the ROI. Table 3-1 shows Indium atom densities (#/nm^2) for each layer. The density of Indium atoms increases from 92.4/nm^2, to 145.2/nm^2 from 1st layer to the 3rd layer. The 4th layer is showing a slight drop in density, but still higher than the 1st layer. Therefore, it can be concluded that Indium segregates along the growth. Frost et al also measured the QD density using AFM and found that the first layer has much lower QD density (~7×10^7/cm^2) compared to the latter deposited layers (5×10^{10}/cm^2). [12] It is possible that Indium composition does not reach a threshold composition during the growth of first layer InGaN, and QDs would not form till 3rd layer. Excess Indium atoms segregate and are available to be incorporated as the growth continues, and incorporated into the following InGaN QD wetting layers. The threshold composition can then be reached in the following subsequent wetting layers.

InGaN QD Layer Number	Indium Density(Projected)/(nm^2)
1st	92.4
2nd	117.4
3rd	145.2
4th	117.9

Table 3-1. Indium atom density #/nm2 for each InGaN QD wetting layer

3.1.3 Summary

APT and STEM are utilized to characterize compositional inhomogeneities within InGaN 2D layer nanostructure. A sample with 30 nm thick InGaN layer is first investigated. Even though TEM results indicate an atomic abrupt interface, APT gives an interface of ~1 nm thick due to artifacts or the composition profiling method. Low In containing ($In_{0.15}Ga_{0.85}N$) bulk layer does not show clear sign of clustering for In atoms follow a binomial distribution. On the other hand, $In_{0.4}Ga_{0.6}N$ thin layers show Indium nano-size clustering due to larger lattice mismatch. APT data for the

InGaN multiple thin layer sample shows there is Indium segregation during the growth. At the same time, the surface can roughen up due to QD formation. Both these reasons can cause compositional inhomogeneity for InGaN thin layers.

3.2 GaAsBi Bulk Layer

III-V semiconductor alloys containing Bi, bismides, have recently drawn more attention because of their predicted properties: large bandgap reduction per percentage of Bi incorporation and large spin orbit bowing .[13, 14, 15] Growth of bismides is quite challenging since Bi desorbs from the surface at typical growth temperatures. In order to incorporate as much Bi as possible, samples need to be grown under a low temperature. The growth is further complicated by the formation of group III or Bi droplets. [16] Previous paper published by Rodriguez and Millunchick predicts the highest Bi incorporation in GaAsBi occurs when Ga droplets formed on the surface. [17] In this project, a series of GaAsBi bulk layer samples on top of GaAs (001) substrate grown under different temperature and fluxes combinations to study how these two parameters can be tuned to achieve a higher, uniform Bi incorporation in GaAsBi. This project consists of two sections: the impact of surface droplets on compositional inhomogeneity and a temperature growth study. In total, five samples are grown by MBE with temperature ranges from 315 °C to 340 °C, and two types of growth methods involved. The growth conditions for these five samples are summarized in Table 3-2.

Sample Label	Film Growth Temperature, T_g (°C)	V: III ratio	Growth Method
Sample A	315	1.7	Continuous
Sample B	315	3.5	Continuous
Sample C	315	1.7	Interrupted
Sample D	325	3.2	Continuous
Sample E	340	3.2	Continuous

Table 3-2. Growth Conditions for GaAsBi bulk film samples

3.2.1 Impact of Droplet Formation on Compositional Inhomogeneity

Sample A, B and C are grown and characterized to understand the impact of surface features like Ga droplets on compositional inhomogeneity for GaAsBi. All three samples have the similar structure of GaAs substrate with a 250-nm thick GaAs buffer layer deposited first and 500 -nm thick GaAsBi grown on the top. Sample A is grown at 315 ^{0}C with V: III ratio of ~1.67 and continuous growth, such temperature and fluxes region would promote Ga droplets formation. Sample B is grown under the V: III ratio of ~3.5 with continuous growth. This sample is expected to have a smooth surface due to the high V: III ratio. Sample C grown under V: III ratio of ~1.7 with growth interruption of every 25nm. The interruption is introduced to consume the excess Ga on the surface, therefore suppress droplet formation.

SEM images of all three samples are taken and compared. Sample A has a high density of Ga droplets on the surface as predicted (Figure 3-10 (d)). Sample B shows a smooth, featureless surface (Figure 3-10 (c)). Sample C shows a relatively smooth surface without visible droplets, indicating the excess Ga has been eliminated by growth interruption (Figure 3-10 (b)). The crystal quality has been examined by θ- 2θ X-ray diffraction(XRD) of each sample (Figure 3-10 (a)). Sample A shows a broad film peak. Sample B exhibits a sharp peak of 568 arcsec to the left of the substrate peak and gives an estimation 2% incorporation in Bi. The film is of high crystal quality with only 71 arcsec FWHM. XRD of Sample C also shows a distinct film peak on the left side of the substrate peak with FWHM of 100 arcsec. Crystal quality of the growth interrupted sample is not as good as the continuous growth one with high V: III ratio.

The inhomogeneity issue is further investigated with TEM and APT. Figure 3-10(a) shows the HAADF image of Sample A, in which a Ga droplet is indicated with white dashed line. The non-uniform contrast reveals a large variation in Bi incorporation. Indeed, the APT reconstruction agrees with the TEM image. A reconstruction showing Bi distribution in $50 \times 50 \times 180$ nm^3 is shown in Figure 3-11(b). Bi atoms are denoted by blue dots, with other elements invisible. A cylindrical ROI is cut out and the line profile of Bi along Z axis

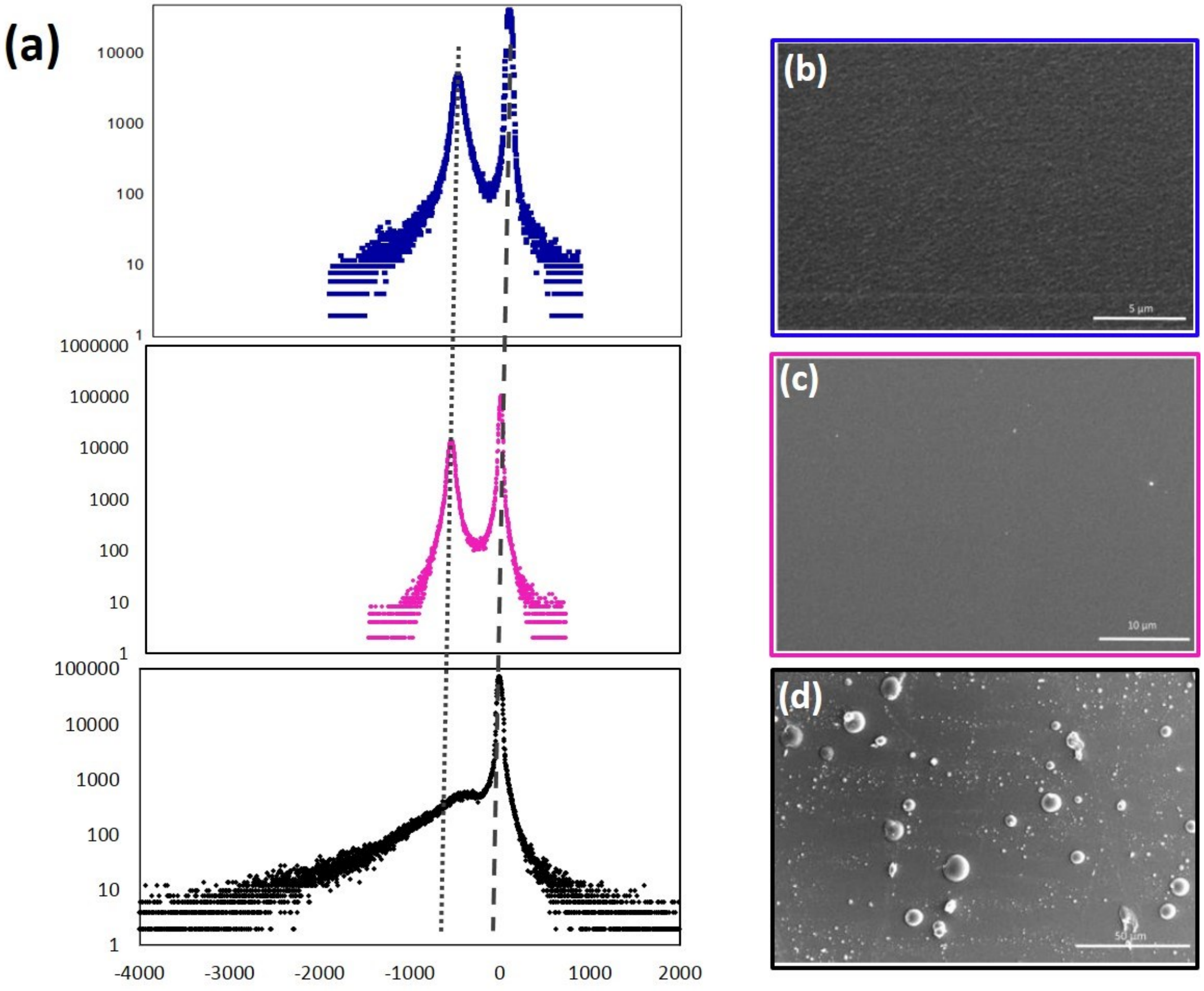

Figure 3-10. (a) Theta- 2 Theta XRD results on Sample A(black), B(magenta), and C(blue). (b) Planar view SEM image of Sample C (c) Sample B (d) Sample A, respectively.

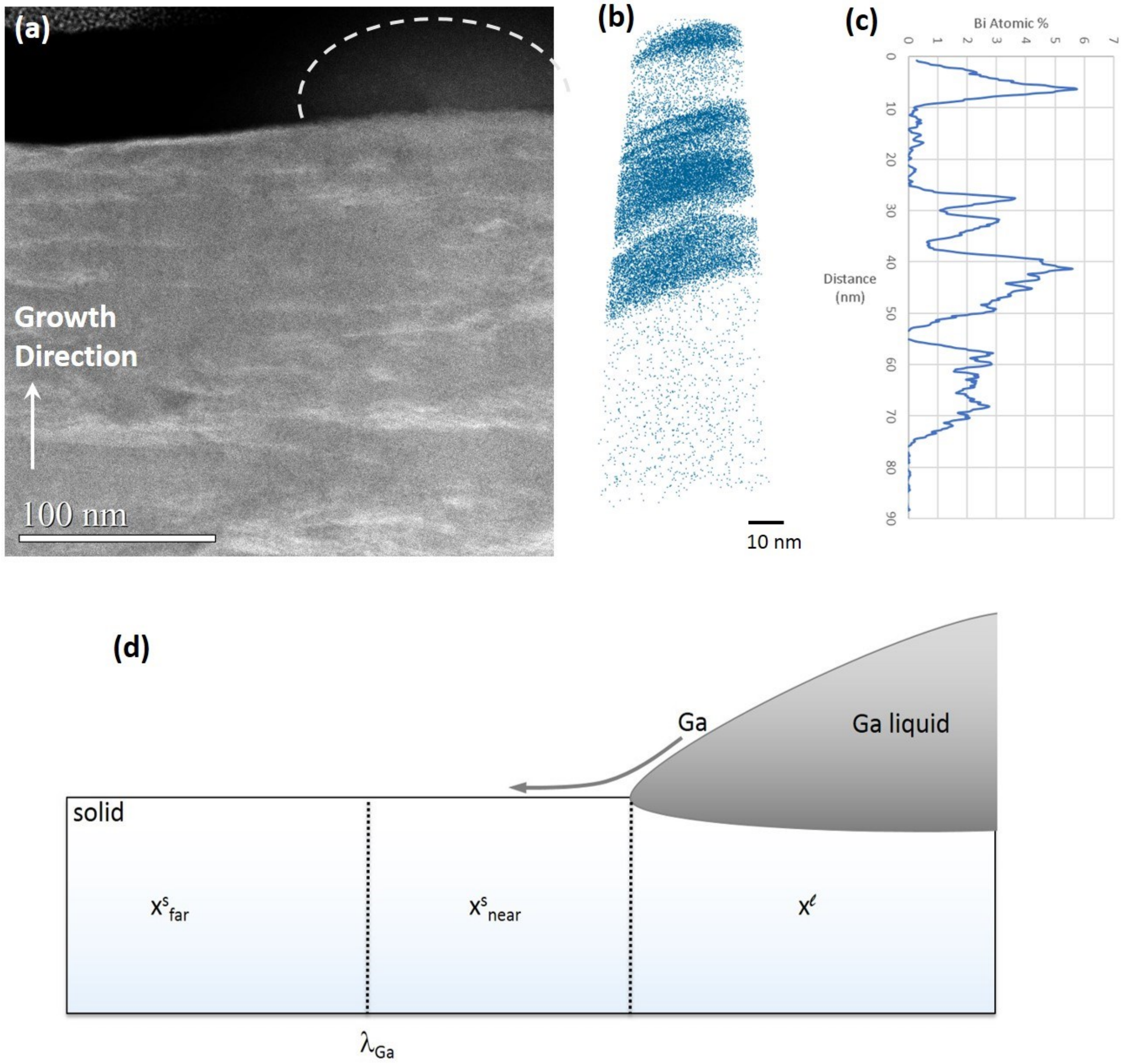

Figure 3-11. (a) TEM image of cross section of sample A (b) APT reconstruction of Sample A showing inhomogeneous Bi distribution, denoted by blue dots (c) Line profile of Bi concentration of a cylindrical ROI (d)Illustration of the available elemental fluxes and different incorporation regimes when Ga droplets are present on the growth surface

As illustrated in Figure 3-11, STEM and APT reconstruction reveal stripy feature of Bi, with thickness ranges from 5 < d < 50 nm. A line profile shows that the Bi incorporation ranges from 0 to 7% along the growth direction. The combination of TEM and APT data suggest that the broadened peak observed in XRD scans are a result of compositional fluctuations instead of defect injection or precipitation. It has been proposed that the composition fluctuation is due to Ga flux gradient on the surface when Ga droplets are present. Bi composition at the vapor-solid interface has been demonstrated to be proportional to the Ga flux assuming constant Bi and As fluxes. [18] Normally, only the flux imprinting on the surface from the vapor is taken into consideration. However, the Ga droplets in this sample can also be a source of Ga. Ga fluxes increase in the vicinity of the droplet, which are prone to Bi incorporation. The region that is far away from the droplet has a much lower Ga flux. This difference in impinging fluxes results in the composition difference in different regimes: beneath the droplet, near the droplet, and far from the droplet (Figure 3-11(d)). The Bi concentration homogeneity is largely improved by growth interruption. (Figure 3-12) The growth is interrupted every 25-nm deposition of GaAsBi. Presence of Ga droplets has a strong impact on the subsequent Bi incorporation of the film, which contributes to the broad background(film) signal in the XRD scan (black). The spatial distribution shows Sample C has a uniform Bi incorporation with average Bi concentration of 0.9%.

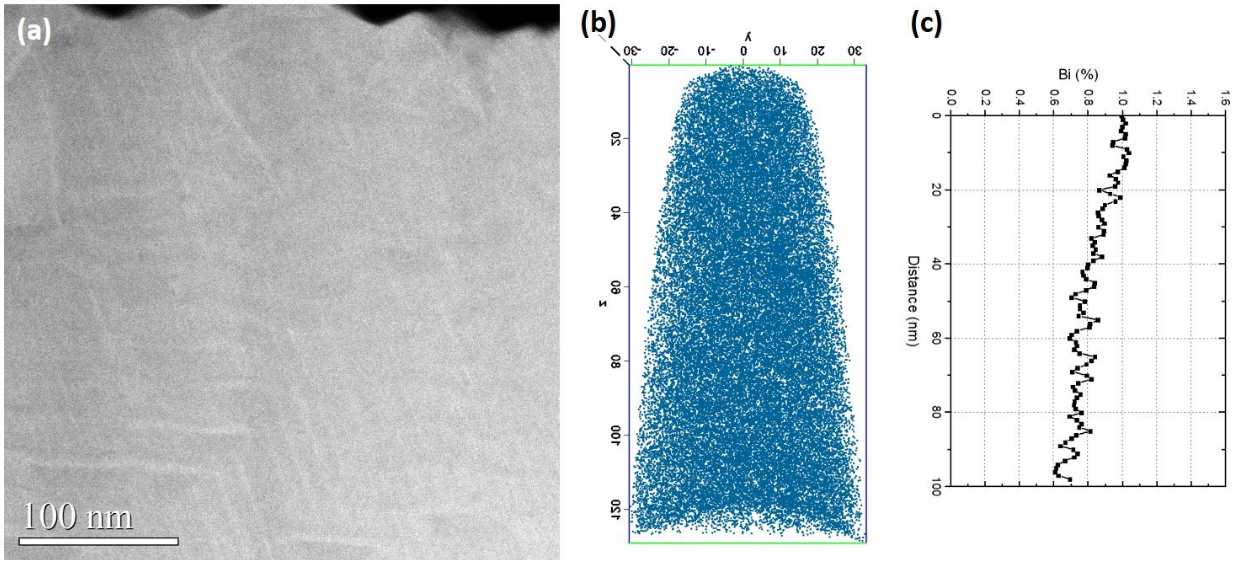

Figure 3-12. (a) Cross Sectional TEM image of Sample C (b) spatial distribution of Bi atoms in APT reconstruction (c) 1D Bi concentration profile along Z axis.

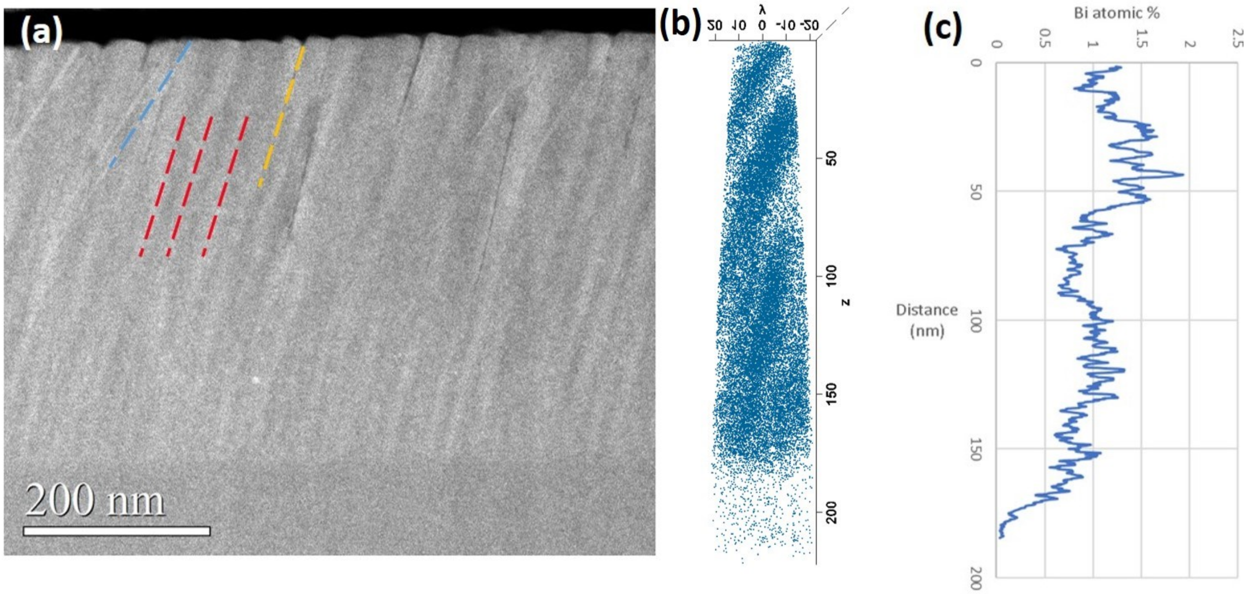

Figure 3-13. (a) Cross Sectional TEM image of Sample B (b) APT reconstruction reveals lateral composition modulation (c) Line profile of Bi concentration for a cylindrical ROI.

APT and TEM of the continuous growth sample with V: III ratio of 3.5 (Sample B) exhibits a more homogeneous Bi distribution with average Bi concentration of 1% (Figure 3-13). Both TEM and APT data reveal lateral composition modulation. Besides lateral composition modulation, zinc blende GaAsBi clusters are also observed in the film. Figure 3-13(a) is the TEM cross sectional image showing rich distribution of GaAsBi clusters. Lateral composition modulation is indicated by red dash lines. GaAsBi clusters tend to locate at the Bi-poor regions. Defects that resemble pores are also observed (orange), the angle between pores and the top surface of the sample varies from 77° to 83°.This agrees with the angle between crystal plane (n11) with ($5 < n < 8$) and (001). Stacking faults angled at 45 ° to the sample surface are also observed (blue). This is not surprising that (111) is the close packing plane for zinc blende crystal structure.

Figure 3-14(a) –(c) provide zoomed-in HAADF TEM images. GaAsBi clusters tend to form around pores. Figure 3-14(c) presents a high resolution HAADF image of GaAsBi clusters, which is almost lattice matched with zinc blende GaAsBi matrix. Figure 3-14(d) is the APT reconstruction for a region that contains Bi-rich clusters. A iso-concentration surface of 3.5% Bi is selected and these clusters in APT have spherical shape. They tend to line up at the Bi-poor region between two Bi-rich stripes. The line profile of a cylindrical ROI (20 nm in diameter and 200 nm in height) is shown in Figure 3-14(e), with growth direction indicated by the arrow. The line profile shows a ~0.9% average Bi concentration the Bi concentration drops at the interface between substrate and film. The line profile has a large Bi concentration fluctuation of ~0.2%, the fluctuations are due to both; lateral composition modulation, and the Bi-rich clusters.

Based on the APT and TEM data, it is speculated that lateral composition modulation, pores, as well as the GaAsBi clusters might be induced by surface roughness. Bi incorporate at a different rate, depending on the crystal plane and the surface reconstruction available. Bi atoms could be incorporated faster at (n11) ($5 < n < 8$) surface, and Bi-rich stripes form as the film continues to grow. There is a driving force for GaAsBi precipitate formation since GaAsBi precipitates are often observed in Bi-poor regions. Mass transport of Bi has been reported before by Wood et al. [19] in their research of annealing-induced Bi-rich precipitates. Pores may be left behind between the precipitates and matrix upon such mass transport.

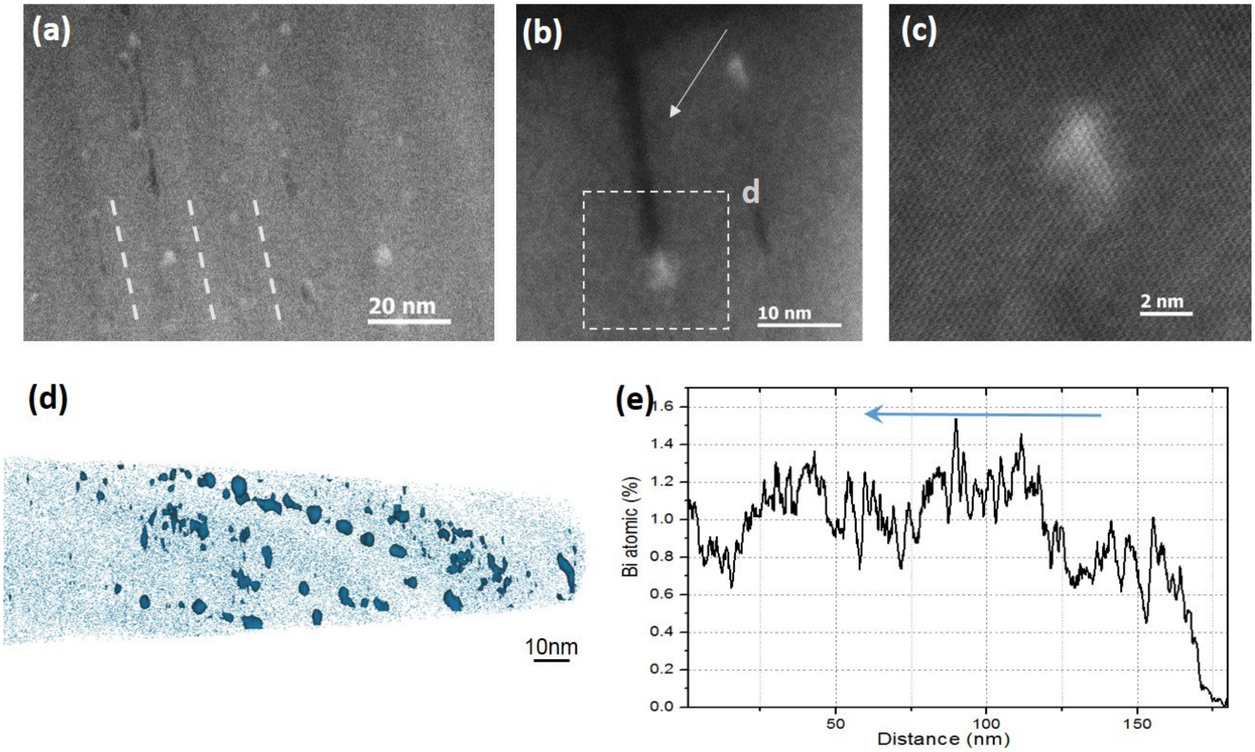

Figure 3-14. (a) HAADF image of sample B, showing bright spots of GaAsBi in bulk film (b) GaAsBi precipitates formed on the surface on the sample, and one at the end of a sub grain boundary. (c) HAADF image of a zoomed in view on GaAsBi precipitates. Bi can be seen that has ordered on zinc blende (111). (d) APT reconstruction with iso-concentration surface for Bi at 3%. (e) line profile of the cylindrical ROI showing matrix of 1% Bi with fluctuation.

3.2.2 Impact of Temperature on Bi Incorporation

Sample D & E are further grown with higher temperature than to test hypothesis of surface roughness induces composition modulation. Sample D is grown under temperature of 325 °C, and Sample E is grown using an even higher temperature at 340 °C. Combination of Sample B (grown at 315 °C), these three samples are studied to see how surface roughness affect Bi incorporation. AFM and XRD scans are done and the results are plotted in Figure 3-15. All Root Mean Square (RMS) roughness are measured in 5 µm* 5 µm areal scans and the composition is estimated from

XRD θ-2θ scans. The Bi composition is measured through the position difference between the substrate peak and the film peak, Δθ.

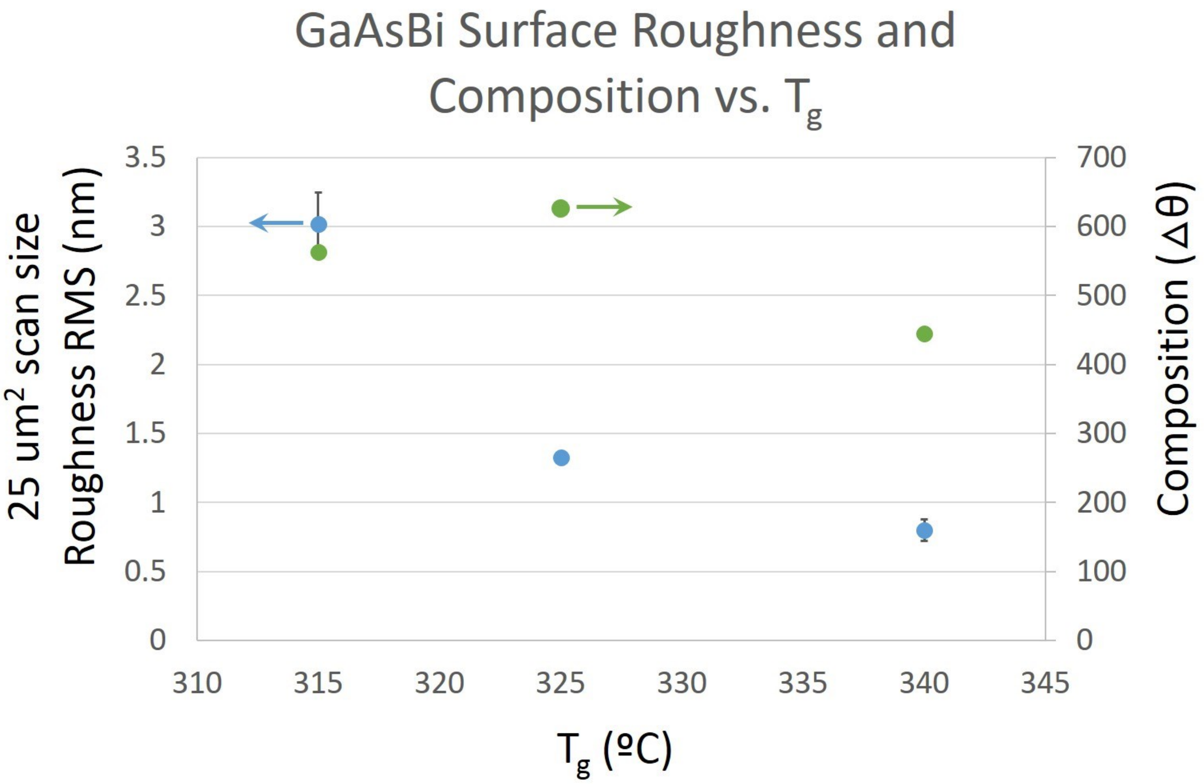

Figure 3-15. RMS and Bi incorporation vs Growth Temperature Tg.

Figure 3-15 shows the RMS roughness(nm) and Bi composition(arcsec) vs the growth temperature. All three samples do not show any Bi droplet formation on the surface. The roughness RMS is 2.7 nm for Sample B (315 °C), 1.3 nm for Sample D (325 °C), and 0.8 nm for Sample E (340 °C). The surface roughness decreases with increasing temperature, which is not surprising, since a higher growth temperature gives more kinetic energy for the atoms to migrate. According to XRD scans, Sample E presents a peak separation of 445 arcsec and Sample B has a separation of 560 arcsec. However, Sample D, which is grown 10 °C hotter than Sample B, shows a much lower roughness RMS but a higher Bi concentration. The peak separation is measured to be 630 arcsec. Figure 3-16 shows the morphology of Sample D, it has clearly shown a much smoother top surface and no clear strips for composition modulation, the contrast is mostly contributed by thickness variation. High magnification HAADF image shows the film is almost a random alloy (Figure 3-16(b)). Defects can occasionally be observed, with really low density. Figure 3-16(c) captures the area where a possible void locates above a Bi-rich region, both the void and the Bi-rich region are circled out with white dash lines. APT reconstruction and Bi 1D concentration profile is present in Figure 3-17, with Bi denoted in blue. Even though TEM suggests a fairly uniform Bi incorporation, Figure 3-17(a) shows a non-uniform Bi incorporation, the average Bi concentration is measured to be 1.4%, and the Pearson coefficient is ~0.30. It has higher Bi incorporation compared to Sample B (0.95%). The Bi concentration measured for Sample D is consistent numbers that has been reported before [20].

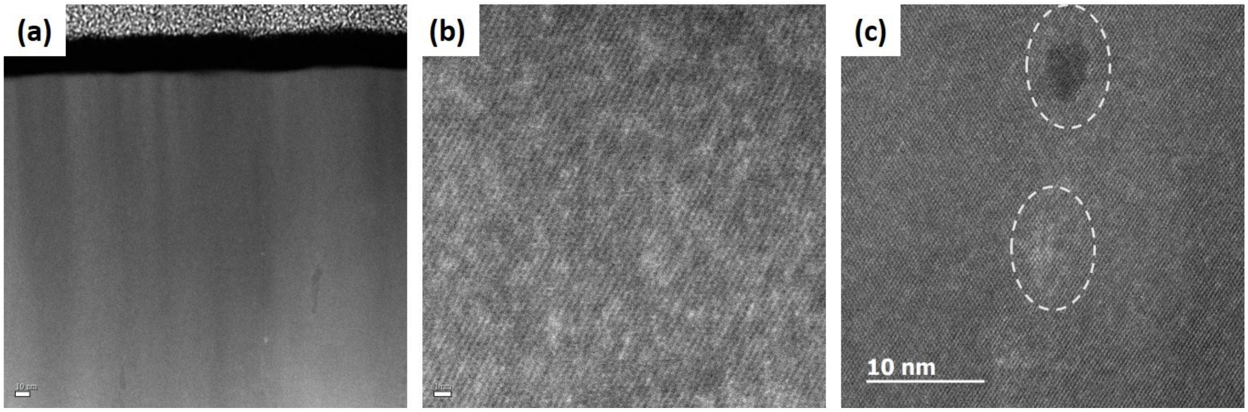

Figure 3-16. Low magnification cross sectional TEM image showing smooth surface and uniform Bi incorporation for Sample D (b) High magnification HAADF image showing small Bi-rich clusters uniformly distributed (c) HAADF image showing Bi-poor(dark) and Bi-rich (bright).

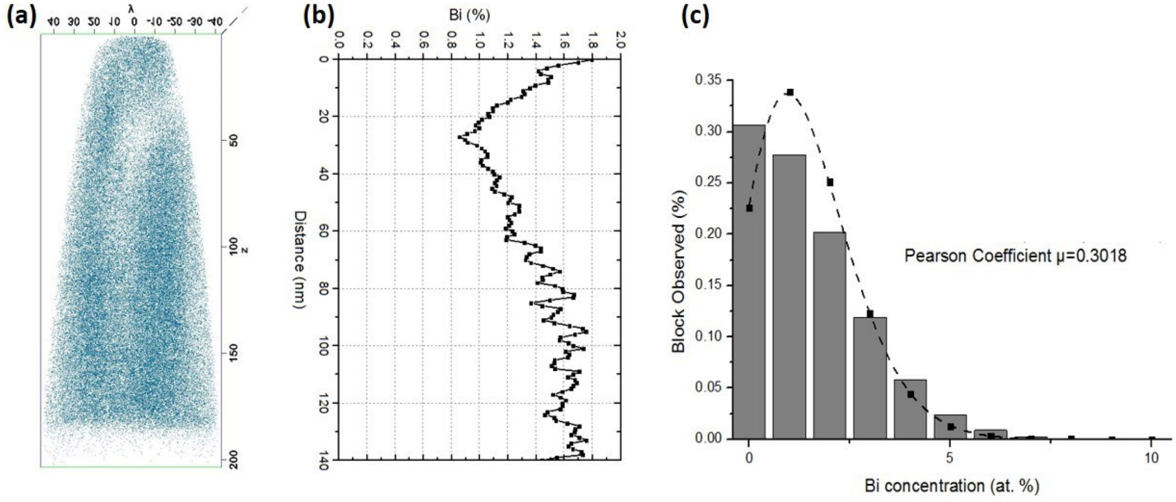

Figure 3-17. (a)APT reconstruction of sample D (2) 1D concentration profile of Bi along z axis of a cylindrical ROI.

Sample E, being grown with an even higher temperature, shows the smoothest surface among the three samples. Cross sectional TEM image does not show compositional modulation or defects. The APT reconstruction is in good agreement with the XRD scan and TEM image, showing a uniform Bi distribution with average concentration of 0.8%. (Figure 3-18)

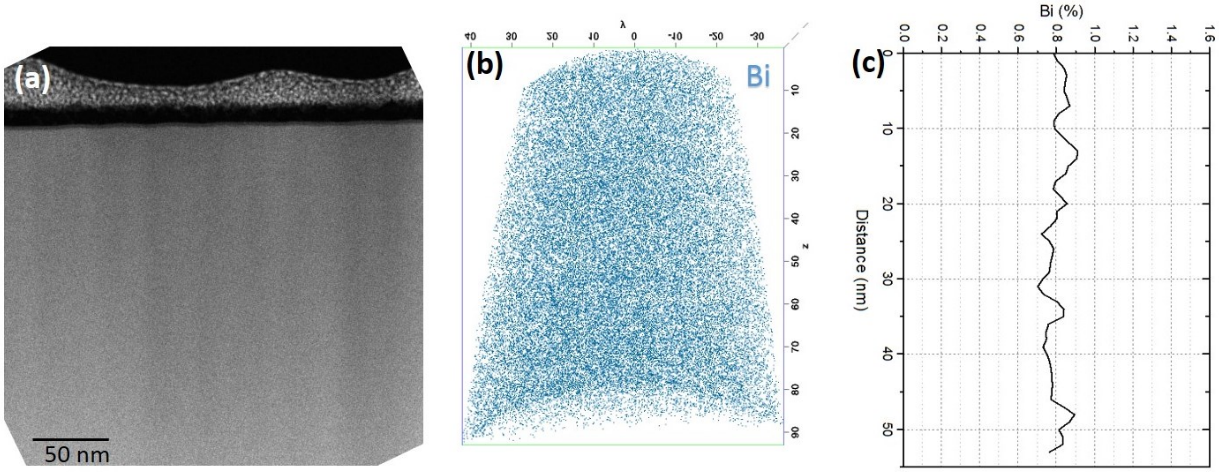

Figure 3-18. (a) Cross Sectional TEM image of Sample E (340 ^{0}C) (b) APT reconstruction with Bi atoms denoted in blue (c) 1D conecntration profile of a cylindrical ROI.

As mentioned before, Pearson coefficient is used to describe how homogeneous the film is, values for all data sets are calculated and shown in Table 3-3. Pearson coefficients among these five samples ranges from 0.02 to 1.0.

The Pearson coefficient is calculated with bin size of 100 ions. Both specimens for Sample A show Bi-rich stripes due to Ga droplets, the Pearson coefficient is calculated to be 1.0, even though the average Bi atomic percentage is different for two data sets. The Bi atomic percentage is calculated as the numerical average. Therefore, the Bi atomic percentage depends on the data set and region of interest used for averaging. Two data sets are also collected for Sample B, the data set that captured Bi-rich clusters shows significant higher Pearson coefficient that the other one that only captures lateral composition modulation. TEM data for Sample C indicates contrast that originates from annealing, while the APT data shows a uniform Bi distribution with Pearson coefficient close to 0. Data sets from Sample D have a similar Pearson coefficient value of ~0.3. Sample E, grown at the hottest temperature among all five samples, has a Pearson coefficient of 0.02.

Sample	Growth Temperature (°C)	Specimen	Bi Atomic %	Pearson Coefficient
Sample A	315	1	0.52	1.0
		2	1.05	1.0
Sample B	315	1	1.02	0.99
		2	0.96	0.37

Sample C	315	1	0.88	0.03
Sample D	325	1	1.48	0.30
		2	1.52	0.37
Sample E	340	1	0.88	0.02

Table 3-3. Pearson Coefficients and Bi atomic percentage for samples investigated.

SEM, XRD, TEM and APT assemble into a strong toolkit for investigating GaAsBi bulk layer compositional inhomogeneity. SEM, in particular, has an advantage of simple sample preparation and non-destructive examination. It gives preliminary results of these samples. XRD can be seen as a quick way to examine average crystal quality. Small compositional variation and features cannot be resolved by this technique. This is demonstrated in Sample B: the XRD scan gives a distinct peak at 2% Bi concentration, while lateral compositional modulation and precipitates are clearly observed when examined in TEM and APT. In examining compositional inhomogeneity microscopically, the combination of TEM and APT would be the best practice. The morphology information gathered from TEM complements the compositional profile from APT.

This chapter completes part of the first goal of this thesis. A more detailed summary will be included at the end of Chapter 3. This chapter compares and contrasts APT and STEM results for 2D layer compound semiconductor nanostructures. The two nanostructures examined above show that Atom Probe Tomography provides a unique insight of the composition inhomogeneities. The technique is useful in explaining the growth mode as well as answering clustering questions. APT is capable of distinguish various inhomogeneity situation from random alloy fluctuation, multilayer intermixing and nano-size clustering. The inhomogeneity issue can be described and compared using Pearson coefficient.

It might be difficult to accurately measure composition for small features such as nano-size clustering since they can be distorted due to trajectory aberrations caused by non-uniform evaporation. To better understand the nanostructures, it is beneficial to have multiple microscopy information at hand. It is best practice to partner APT with other microscopy techniques to understand the material behavior thoroughly.

3.3 References

1. Ho, I ‑ hsiu, and G. B. Stringfellow. "Solid phase immiscibility in GaInN." *Applied Physics Letters* 69.18 (1996): 2701-2703

2. Yu Karpov, S. Suppression of phase separation in InGaN due to elastic strain. *MRS Internet J. Nitride Semicond. Res* **3,** (1998).

3. Galtrey, M. J. *et al.* Response to 'Comment on "Three-dimensional atom probe studies of an In[sub x]Ga[sub 1−x]N/GaN multiple quantum well structure: assessment of possible indium clustering"' [Appl. Phys. Lett. 91, 176101 (2007)]. *Appl. Phys. Lett.* **91,** 176102 (2007).

4. Gerthsen, D. *et al.* Indium distribution in epitaxially grown InGaN layers analyzed by transmission electron microscopy. *Phys. Status Solidi C Conf.* **0,** 1668–1683 (2003).

5. Ruterana, P., Kret, S. & Poisson, M. A. Quantitative measurement of In fluctuation inside MOCVD InGaN QWs. *Materials Science and Engineering: B* 93.1 (2002): 185-188.

6. Mancini, L. *et al.* Composition of Wide Bandgap Semiconductor Materials and Nanostructures Measured by Atom Probe Tomography and Its Dependence on the Surface Electric Field Franc o Jean-Franc o. (2014).

7. Giddings, A. D. *et al.* Composition profiling of InAs quantum dots and wetting layers by atom probe tomography and cross-sectional scanning tunneling microscopy. *Phys. Rev. B* **83,** (2011).

8. Waugh, A. R., Boyes, E. D. & Southon, M. J. Investigations of field evaporation with a field-desorption microscope. *Surf. Sci.* **61,** 109–142 (1976).

9. Moody, M. P., Stephenson, L. T., Ceguerra, A. V & Ringer, S. P. Quantitative binomial distribution analyses of nanoscale like-solute atom clustering and segregation in atom probe tomography data. *Microsc. Res. Tech.* **71,** 542–50 (2008).

10. Pearson, K. On the theory of contingency and its relation to association and normal correlation; On the general theory of skew correlation and non-linear regression. (1904).

11. Frost, T., Banerjee, A., Sun, K., Chuang, S. & Bhattacharya, P. InGaN/GaN Quantum Dot Red (lambda = 630 nm) Laser. *IEEE J. Quantum Electron.* **49,** 923–931 (2013).

12. Frost, T. *et al.* High performance red-emitting multiple layer InGaN/GaN quantum dot lasers. *Jpn. J. Appl. Phys.* **55,** (2016).

13. Fluegel, B. *et al.* Giant Spin-Orbit Bowing in GaAs 1 − x Bi x. *Phys. Rev. Lett.* **97,** 67205 (2006).

14. Francoeur, S. *et al.* Band gap of GaAs1−xBix, 0<x<3.6%. *Appl. Phys. Lett.* **82,** 3874–3876 (2003).

15. Pettinari, G. *et al.* Bi-induced *p* -type conductivity in nominally undoped Ga(AsBi). *Appl. Phys. Lett.* **100,** 92109 (2012).

16. Lu, X., Beaton, D. A., Lewis, R. B., Tiedje, T. & Whitwick, M. B. Effect of molecular beam epitaxy growth conditions on the Bi content of GaAs1−xBix. *Appl. Phys. Lett.* **92,** 192110 (2008).

17. Rodriguez, G. V. & Millunchick, J. M. Predictive modeling of low solubility semiconductor alloys. *J. Appl. Phys.* **120,** 125310 (2016).

18. Tait, C. R. & Millunchick, J. M. Kinetics of droplet formation and Bi incorporation in GaSbBi alloys. *J. Appl. Phys.* **119,** 215302 (2016).

19. Wood, A. W. *et al.* Annealing-induced precipitate formation behavior in MOVPE-grown GaAs $_{1-x}$ Bi $_{x}$ explored by atom probe tomography and HAADF-STEM. *Nanotechnology* **28,** 215704 (2017).

20. Tixier, S. *et al.* Molecular beam epitaxy growth of GaAs1−xBix. *Appl. Phys. Lett.* **82,** 2245–2247 (2003).

Chapter 4 APT vs. STEM on Buried Quantum Dots Nanostructure[†]

Buried QD nanostructures have been characterized by both APT and STEM to get a better understanding of the growth mode of these material systems. The two characterization techniques are also compared to each other. Two nanostructures will be discussed in this chapter: Ge QDs in AlAs, and GaSb QDs in GaAs. Ge QDs are grown with an innovative high-temperature annealing method and characterized to understand the QD formation mechanism. For GaSb QDs, two samples with different growth modes are characterized and compared to understand the differences between Stranski-Krastanov (SK) growth mode and Droplet Epitaxy(DE).

4.1 Ge QDs in AlAs

A bridge between group IV semiconductors and III-V materials has been long pursued, and lattice matched Ge and (Al)GaAs has been extensively investigated before. [1, 2,3] So far, most Ge QDs are formed by the Stranski-Krastanov (SK) growth mode. SK growth mode is also known as the "layer plus island growth". [4] The problem with a wetting layer is that it breaks the continuity of zinc

---

[†] This chapter is based on the publication "Self-assembled Ge QDs Formed by High-Temperature Annealing on Al(Ga)As (001)", (W O'brien, et al., Journal of Electronic Materials) and "Structural differences between capped GaSb nanostructures grown by Stranski- Krastanov and droplet epitaxy growth modes", (M Dejarld, et al., Journal of Applied Physics) and has been reformatted to departmental guidelines

blende lattice and the subsequent III-V growth suffers from antiphase domains when transiting from diamond to zinc blende crystal structure [5] Besides, the strain between Ge and GaAs increase chance of defects formation.

Lateral epitaxial overgrown is one of the approaches that can form self-assembled QDs without forming antiphase domains. The Ge QD in AlAs nanostructure studied here is grown by MBE using high-temperature in-situ annealing method to achieve lateral epitaxial overgrown (Figure 4-1). As demonstrated below in the figure, the sample is first deposited GaAs buffer and a thin layer of AlAs. A thin layer of Ge is then deposited at a lower temperature (410 °C). The sample is brought to 690 °C for annealing. More AlAs is grown seamlessly over the Ge QDs, and the process can be repeated for multiple Ge QDs layers. For this specific sample, five layers of Ge QDs are grown using the method mentioned above.

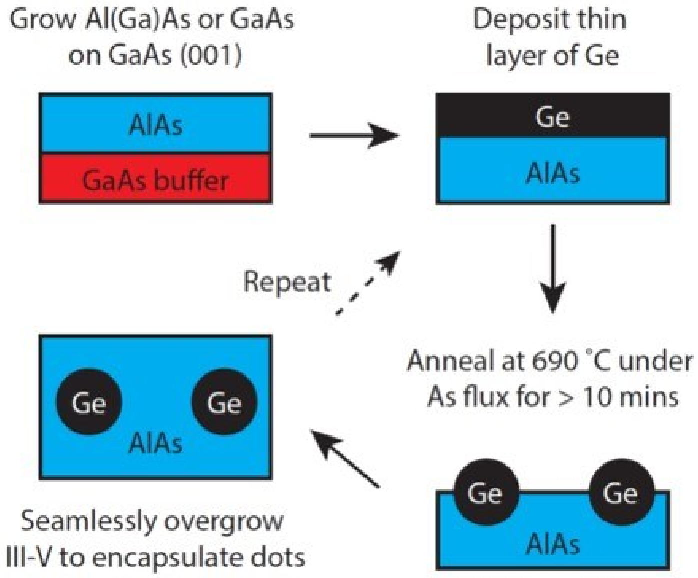

Figure 4-1. Process for Ge QDs formation using in-situ annealing

4.1.1 APT and TEM Results

Atom Probe data sets are collected with the specimen under a base temperature of 25 K and laser energy of 0.12 pJ. The laser energy is tuned for a Al/As ratio close to 1 to ensure most accurate determination of the composition.

Quantum dots are identified by iso-concentration surfaces. Figure 4-2 shows the histogram of size distribution of APT reconstructions, the number of Ge QDs vs. Volume (nm^3). The size is roughly estimated based on the dimension of these QDs. Approximately 100 QDs' sizes are accounted for. The majority of the QDs have a size smaller than 300 nm^3 with large QDs are occasionally observed. More than half of the QDs are seen having a size smaller than 100 nm^3. When focusing on these small QDs, a size distribution vs. volume is plotted and the frequency of observation decrease exponentially with the volume. The size distribution is commonly seen for APT data, for it is only able to examine a small volume.

A typical data set for Ge QDs in AlAs is shown in Figure 4-3. Al is denoted by cyan, while Ge is denoted by green. As shown in the figure, the Ge quantum dots have elliptical shape embedded in the overgrown AlAs. There is no distinct wetting layer formed on each layer of the Ge QDs. It is also noticed that there is two population of Ge QDs present. The ones with relatively large size are usually distributed in the destined region where Ge is deposited. Smaller Ge QDs also form between major layers. These small Ge QDs are barely visible in the TEM image (Figure 4-5).

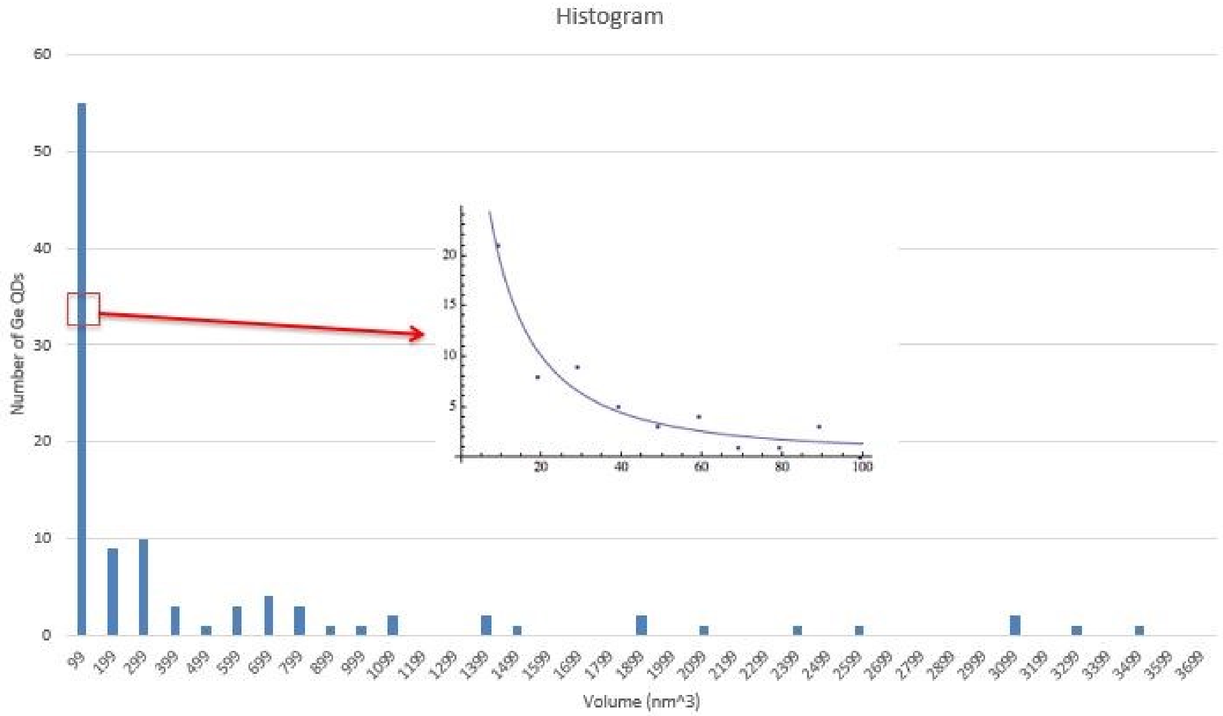

Figure 4-2. Size distribution of APT results: number of Ge QDs vs. Volume (nm^3)

It also appears there is Ge incorporation in the overgrown AlAs layer. A cylindrical ROI is cut out, located at the bottom AlAs layer before any Ge is deposited. The background signal for Ge concentration is found to be 0.015%. Cylindrical ROI that is placed in between three consecutive Ge QDs layers gives Ge concentration of 0.11% and 0.18%, almost 10 times of the background Ge concentration. Some Ge atoms got incorporated into the AlAs layers other than forming Ge QDs. A composition profile is taken on one of the constructed QD surfaces (Figure 4-4). the composition profile indicates these Ge QDs have a gradual interface of ~2nm thick. The core concentration is estimated using the rightmost data point. For this interface, the core concentration is estimated to be 65%, and the interface locates at where there is 32% Ge. Multiple composition profiles are calculated, and they show a core composition ranges from 16 % to 90 % without Ge concentration plateau at the QD core.

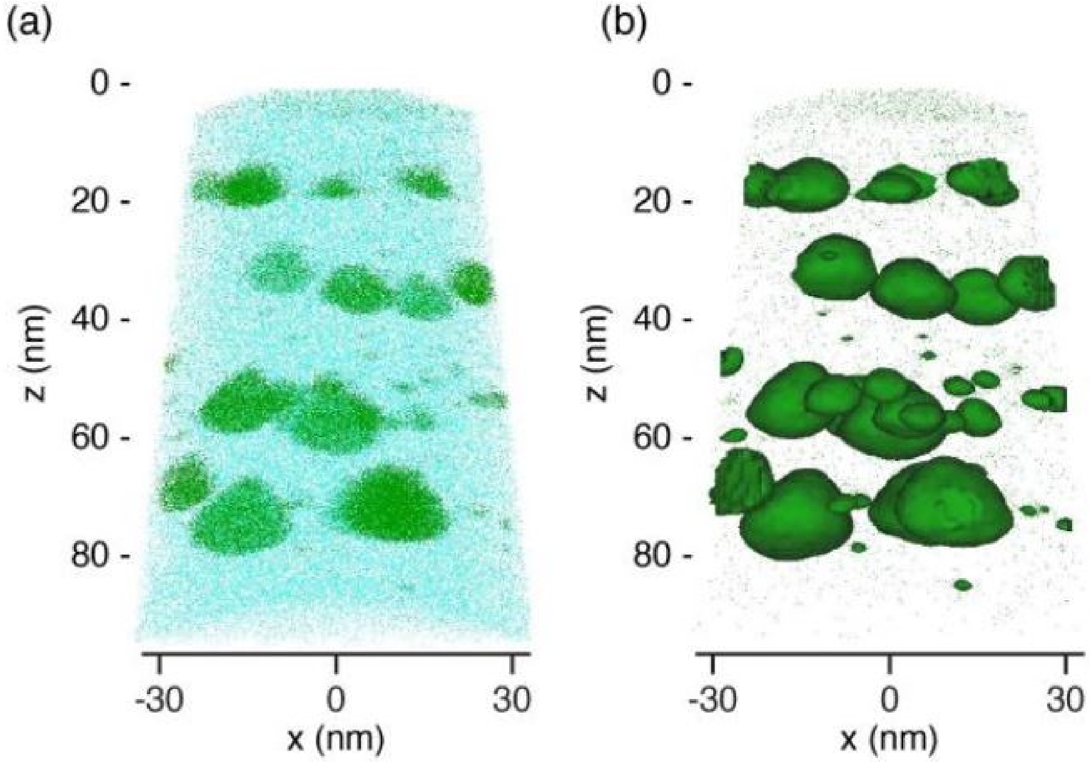

Figure 4-3. Atom Probe results of Ge(green) and Al(cyan) (b) iso-concentration surfaces are constructed using 6% Ge as a threshold.

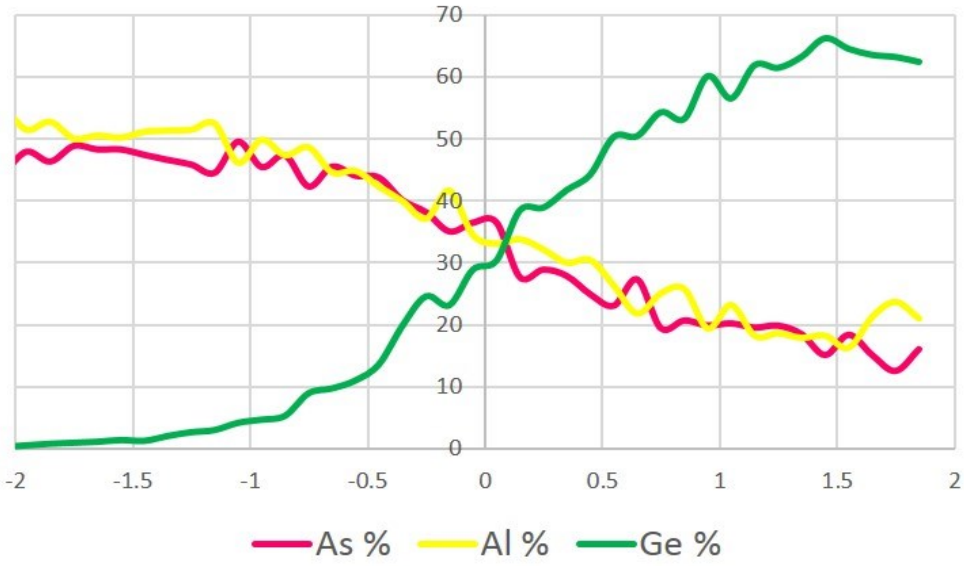

Figure 4-4. Compositional profile across one of the iso-concentration surface constructed

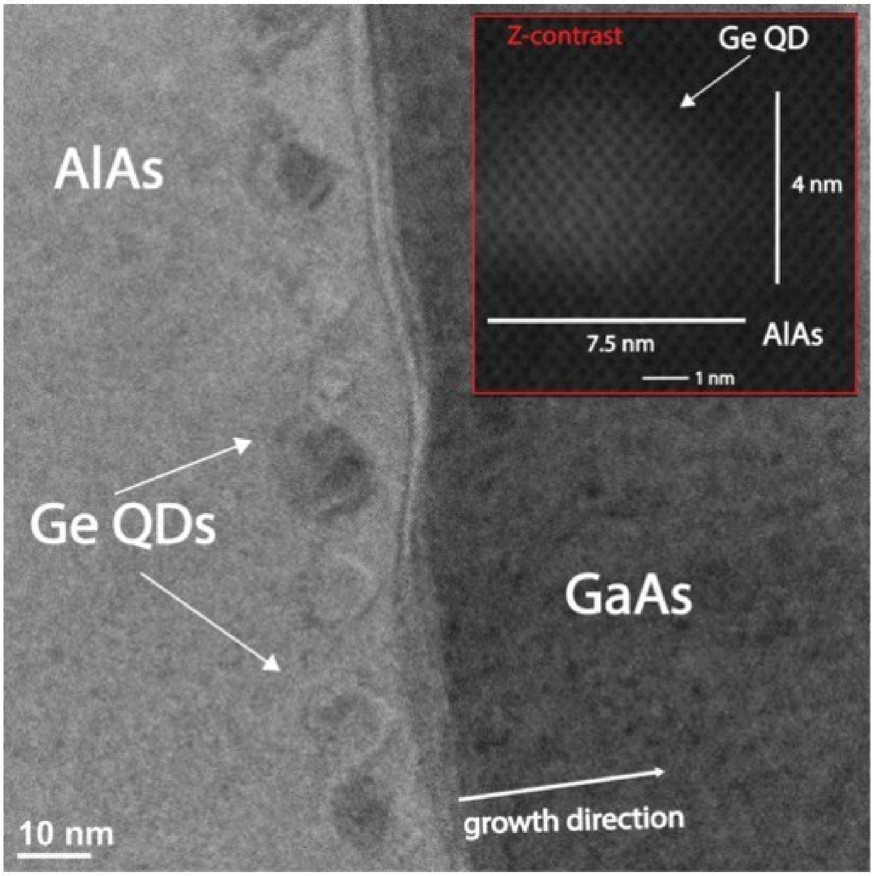

Figure 4-5. TEM micrograph of Ge QDs buried in overgrown AlAs. Inset of HAADF image of Ge QDs

Figure 4-5 is the TEM micrograph of a single layer of Ge QDs buried in AlAs. It can be observed that Ge QDs with diameter around 10 nm line up at the major layer. The inset of HAADF image shows a Ge QDs with diameter ~7.5 nm and 4nm in height. The TEM micrograph shows a shape closer to spherical compared to the APT results. Atomic Force Microscopy (AFM) measurement is also done, and the data suggest an almost spherical shape.[6]

Although APT results provide unique insights to the Ge QDs in AlAs, there remain issues with APT measurement and hopefully will be improved in the future. When working with small features like QDs, it is common to have trajectory aberrations. They usually arise due to the difference in evaporation field of the precipitates(QDs) than the matrix material. [7] Figure 4-6 illustrates how the trajectory aberration affects the density of the cross section due to the change in the surface curvature. When the precipitates have a lower evaporation field than the matrix, precipitates have a concave shape. Atoms within the precipitates would cast inwards and results in a higher density region where precipitates are. On the other hand, if the precipitates have a higher field than the matrix, atoms tend to fly outwards because of the locally convex shape. This leads to a lower density of ions at the precipitates region.

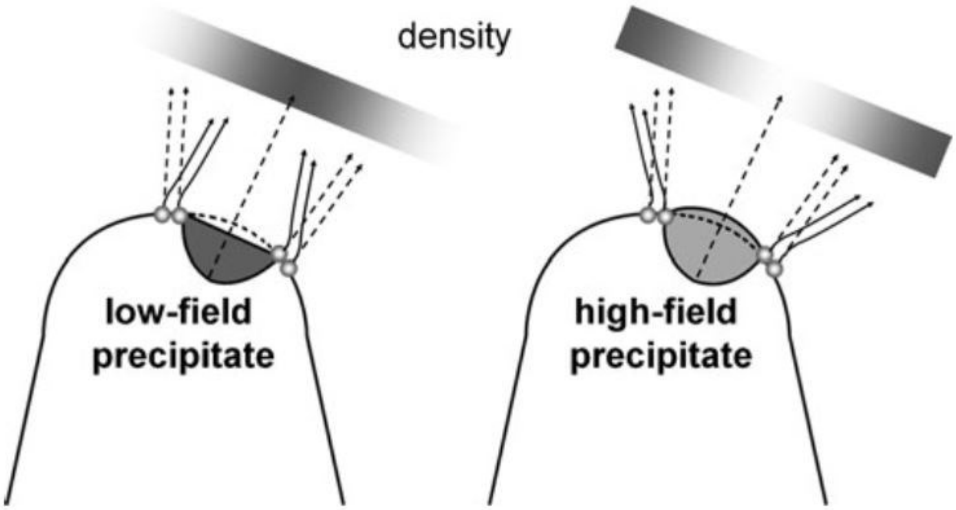

Figure 4-6. Trajectory aberrations and impact on the density due to changes in the surface curvature, low and high field precipitate.[17]

The 2D density is lower at the location of Ge QDs (Figure 4-7). Figure 4-7(a) shows the total atomic density for evaporation plane and Figure 4-7(b) shows the correlated density of Ge atoms. The ion density is much lower for regions where Ge QD resides, which fits the situation with the high field precipitate case in Figure 4-6. Therefore, it can be concluded that Ge has higher field than AlAs. Combined Figure 4-6 and Figure 4-7, the APT data gives the dimension of these QDs bigger than their real sizes. Therefore, the size distribution is subjected to the trajectory aberration.

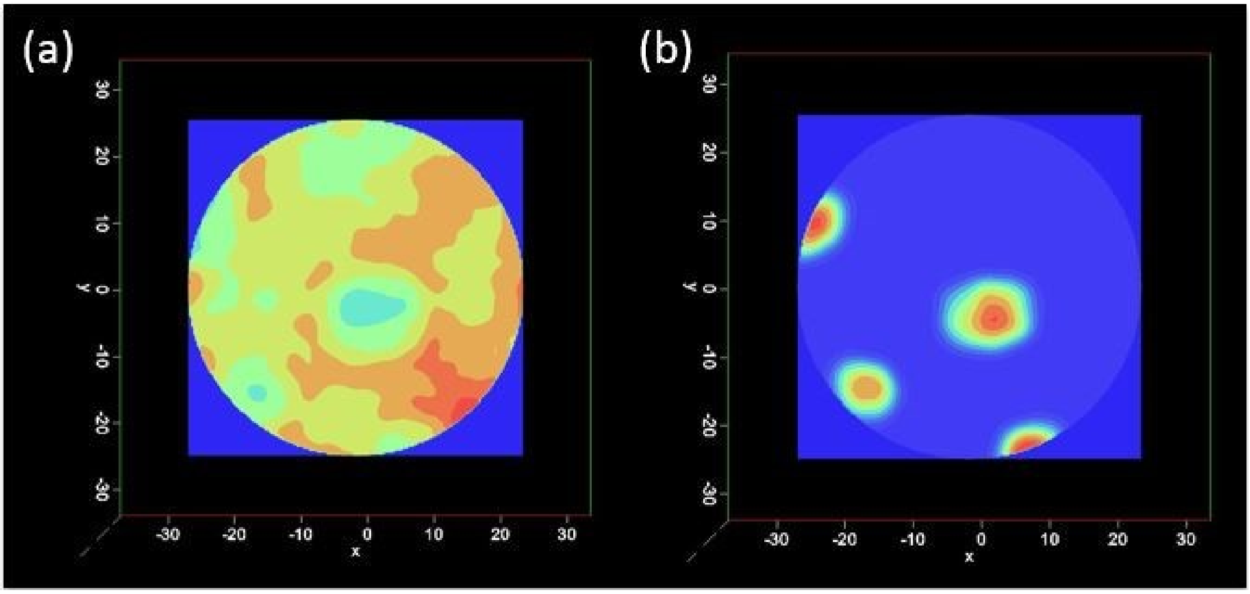

Figure 4-7. (a) 2D iso-density contour plot of Ge, Al and As ions. (b) Density plot of Ge ions

The aberration affects not only the observed size distribution of these QDs but also the measured core composition for these QDs. We have observed a core Ge concentration increases with the volume of QDs increases (Figure 4-8). The core Ge concentration ranges from 15% to 90%, with large fluctuation. However, the accurate core concentration is hard to estimate based on APT data only. It has been observed in other precipitation cases that the core concentration shows an increasing trend as the size grows. [8].

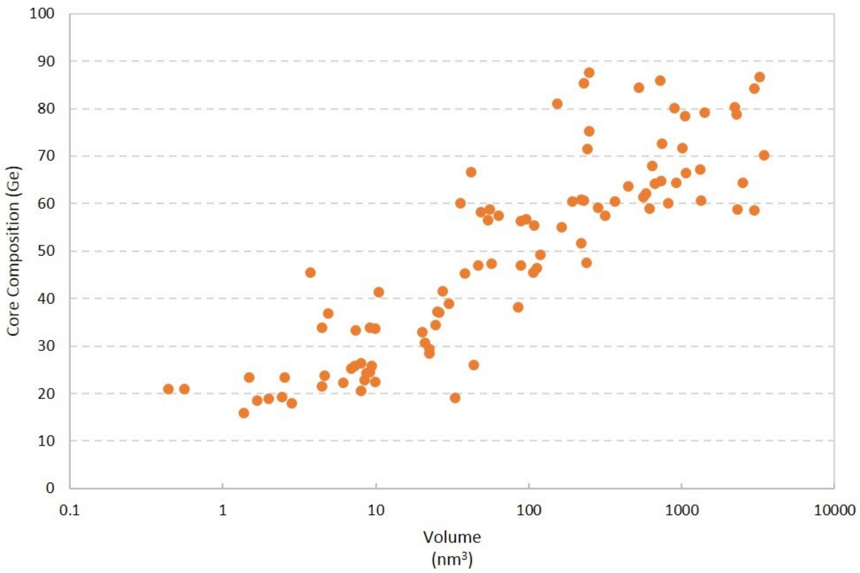

Figure 4-8. Core Concentration (Ge atomic %) vs. volume (nm^3)

Ge QDs are not formed by strain since there is merely any strain between Ge and AlAs (~0.17%). It is also observed longer annealing time would ripen the QDs into larger dots. With all characterization results in consideration, a possible formation mechanism can be proposed. The reason that Ge agglomerate on AlAs is to reduce surface free energy. Atomic-scale roughness present in AlAs can catalyze stable liquid phase Ge thin film formation at a lower temperature. When achieving 690 °C, small nuclei form and melts the layer. Droplets are formed to reduce the surface energy. Since AlAs is somewhat soluble in Ge, QDs can dissolve some of the underlying layers, and then crystallize upon cooling.

4.1.2 Ge QDs in AlAs Growth Study

The above section and results demonstrated a successful growth of Ge QDs in AlAs. However, many questions remain for this nanostructure. First, the role of As flux during the annealing process is not fully understood. Second, the optimal amount Ge deposited for QD formation remains a question. Third, it is unclear how much Ge etches into AlAs layers during annealing.

With these questions in mind, a sample has been grown. The sample is designed similarly to the previous one except that an additional GaAs marker layer will be inserted into each pair of superlattice made of Ge QDs and AlAs overgrown layer. Figure 4-9(a) shows a schematic of the nanostructure that is grown

The sample starts with GaAs buffer layer grown on (001) GaAs substrate. Each GaAs marker layer is 5 nm thick. Three stacks of superlattice structure are grown. Ge is deposited after 3 nm thick of AlAs layer has been grown. On top of the Ge QDs, 7 nm thick of AlAs is grown to cover the QDs. Different amounts of Ge are deposited for each superlattice to investigate how the amount of deposition affect the Ge QD size. The amount of Ge deposited ranges from 0.5 atomic layers to 1 atomic layers. The 2nd and 3rd Ge layer are annealed under except for the first one (0.5 atomic layers).

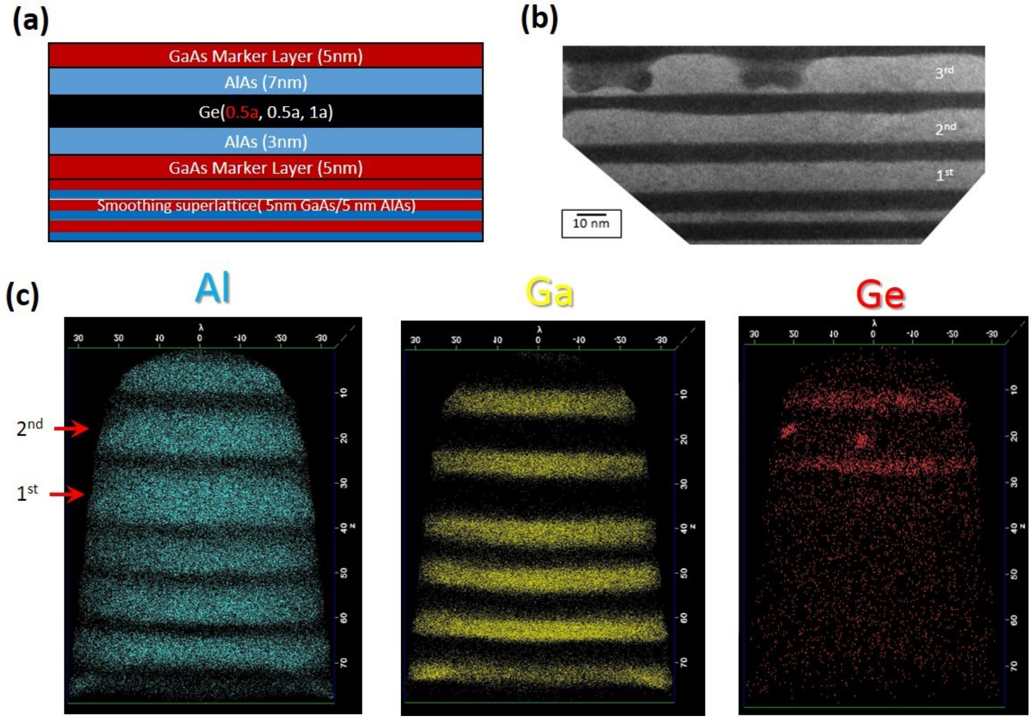

Figure 4-9. (a) schematic of Ge QDs growth study sample (b) DF TEM image of three Ge QDs layers (c) APT reconstruction with distribution of Al(cyan), Ga (yellow) and Ge (red).

Figure 4-9 (b) is the cross sectional Dark Field (DF) TEM image for the nanostructure. The three Ge QDs layers are labeled, and two pairs of Ge can be seen on the 3rd Ge QD layer. As it can be seen from the TEM image, no obvious Ge QDs formed in the first layer. It appears the 3rd layer is showing fair numbers of Ge QDs. Even though 7 nm thick of an overgrown layer is deposited on top of Ge QDs, the formation of Ge QDs has a strong effect on the smoothness of AlAs layer. The AlAs layers become rougher as more layers have been grown. Ge QDs did not etch deeply into the AlAs since Ge QDs are well separated from the lower GaAs layer.

The APT reconstruction shows there is no Ge QDs formed when it is annealed without the As flux (Figure 4-9 (c)). This suggests As flux is necessary for Ge QD formation. However, there is Ge incorporated into the GaAs marker layer on top of the 1st Ge QDs layer. After being exposed to As flux, there are small Ge QDs with a diameter of ~ 5 nm formed within the second AlAs layer. In this data set, two distinct Ge QDs are observed. However, it is also noticed Ge would segregate on top of the AlAs layer and preferentially incorporated into the following GaAs marker layer. The Ge segregation is also observed for the 2nd GaAs marker layer. It has been reported before that Ge would incorporate into GaAs. In fact, AlAs is claimed to be able to act as a barrier layer for Ge to incorporate into GaAs. [9] It is still unclear whether Ge etch into AlAs.

4.1.3 Summary

Both TEM and APT data indicate a success growth of Ge QDs in AlAs overgrown layer with high-temperature annealing method. It is proposed that these QDs form to reduce the surface energy. QD shape, size and core concentration can be distorted due to trajectory aberration. The size distribution follows an exponential decay function, but mainly due to its limitation of examining a larger volume. Concentration profile across the interface shows a gradual interface with core concentration lies in a wide range. The real interface might be more steep than observed since trajectory aberration can broaden the interfacial thickness. Core concentration increase as the size increase, which is consistent with APT results on other precipitates.

Further growth study proves it is important to anneal the Ge under As flux for the Ge QDs to form. The QD formation does not require a large amount of Ge. It is possible for QDs to form even with less than 1 atomic layer Ge being deposited. During growth process, Ge would segregate and incorporate into GaAs. With more layers of Ge QDs being grown, the AlAs surface becomes rougher.

4.2 GaSb QDs with GaAs Capping Layer

GaSb/GaAs nanostructure, having type II band offset, is particularly useful in solar cells because of its ability to increase carrier lifetimes and reduce recombination rates. [10,11] This nanostructure is typically grown using the Stranski-Krastanov (SK) method. The process starts with a thin layer of GaSb deposited on a GaAs substrate. Truncated pyramidal shaped QDs would form due to the large lattice mismatch between GaSb (6.09 Å) and GaAs (5.65 Å). [12] GaAs is then deposited as capping layer. It has been shown before that there is no intermixing and the strain cannot be relieved through capping [13, 14]. Instead, large GaSb quantum dots usually suffer from defects like disintegration: they would break into rings or clusters of QDs upon capping.

Droplet Epitaxy (DE) has been proposed as an alternative way to form III-V nanostructures. [15] Unlike the SK growth method, DE growth starts with liquid Ga deposited on the substrate. Droplets are then exposed to a Sb flux, from which GaSb QDs form. Various nanostructure morphologies are possible depending on the Sb flux and the substrate temperature .[16, 17] [18] This section focuses on examining QDs nanostructures as a result of these two deposition methods using both TEM and APT techniques to get a more complete picture of their formation.

Two samples are grown using MBE; one used the SK method, and the other used the DE method. The growth conditions are chosen to target similar QD dimensions. Both APT and STEM samples are prepared using FIB/SEM dual beam microscope. GaAs is a material that is prone to re-deposition and Ga damage during the FIB process. Therefore, low voltage (5 kV) and low current (4 pA) FIB needs to be used in the final milling step. For this study, APT and EELS are used for compositional characterization. For EELS characterization, long exposure to high electron voltage (300 kV) beam might induce strain and damage to the microstructure. Hence the exposure time is limited to under two minutes for spectra collection.

4.2.1 APT reveals Droplet Epitaxy QD Formation Mechanism

The APT data for SK and DE growth mode is shown in Figure 4-10. The Sb atoms are denoted by blue. For both samples, the APT data show there is a thin wetting layer of Sb. Iso-concentration surfaces are constructed with regions for x >18% Sb. For the SK sample, a single large QD with diameter of 15 nm and height of 4 nm is identified by the blue surface, consistent with AFM measurements (not shown) and other literature. [19, 20] The APT data for the DE growth mode shows pairs of small QDs even though AFM (not shown) suggests quantum rings formed on the surface.[16] The two pairs of dot-like nanostructure have diameter of 4± 1 nm with 2.5 ± 0.5 nm in height. They are separated from each other for 11 ± 1 nm.

The cross-sectional view of APT data provides 2D contour plots for Sb concentration for these samples. A thin slab cutting through the center of both QDs are shown. As it can be seen from the contour plots, SK QD have a much higher core concentration than the DE dots. Line profiles of

QDs and wetting layers for both samples are also shown in Figure 4-11(c) and (d). The wetting layers appear to have similar Sb concentration while the QDs show different Sb concentration.

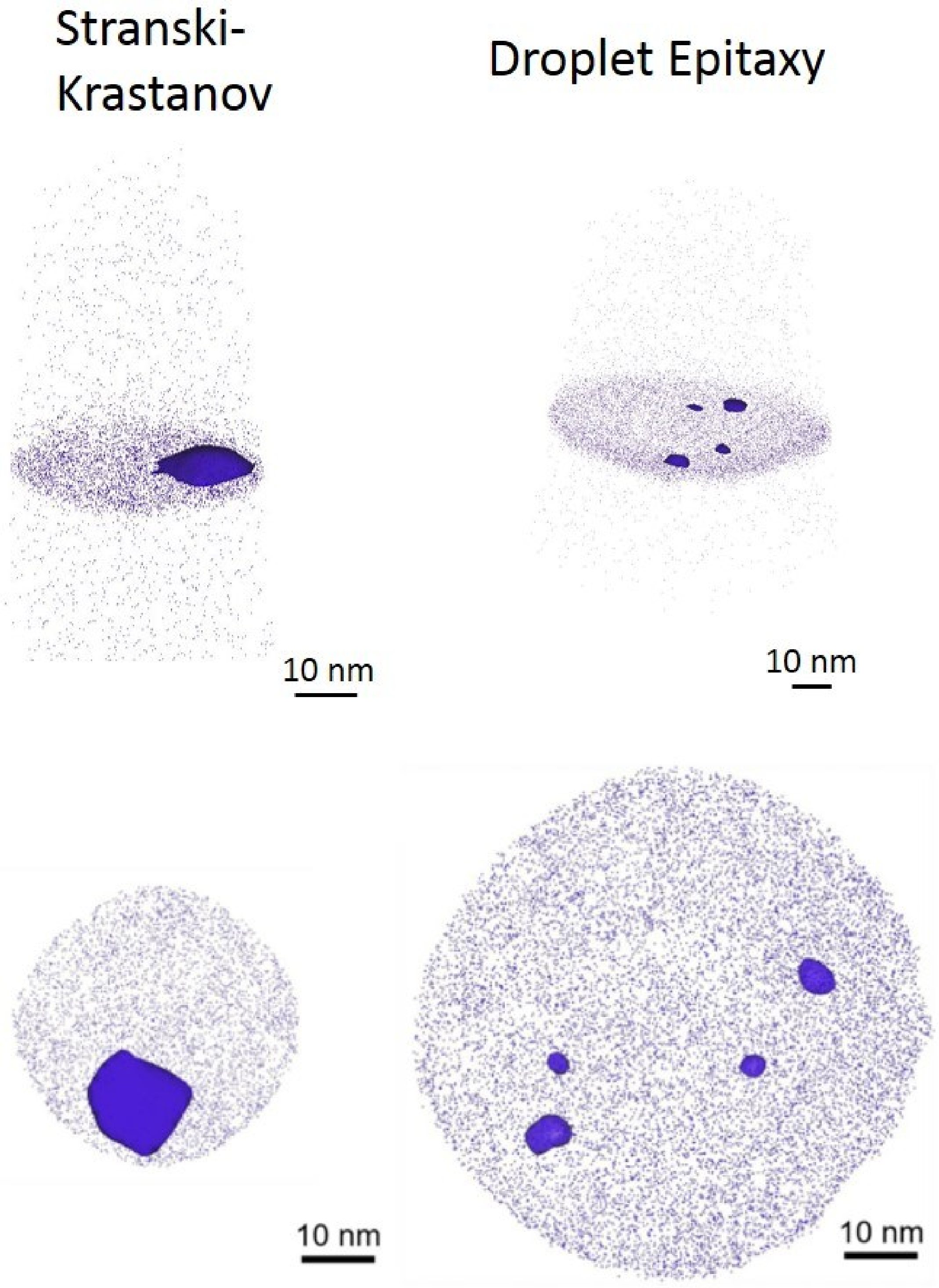

Figure 4-10. APT reconstruction of side view(top) and top view(bottom) of APT data for SK growth (left column) and DE growth (right column).

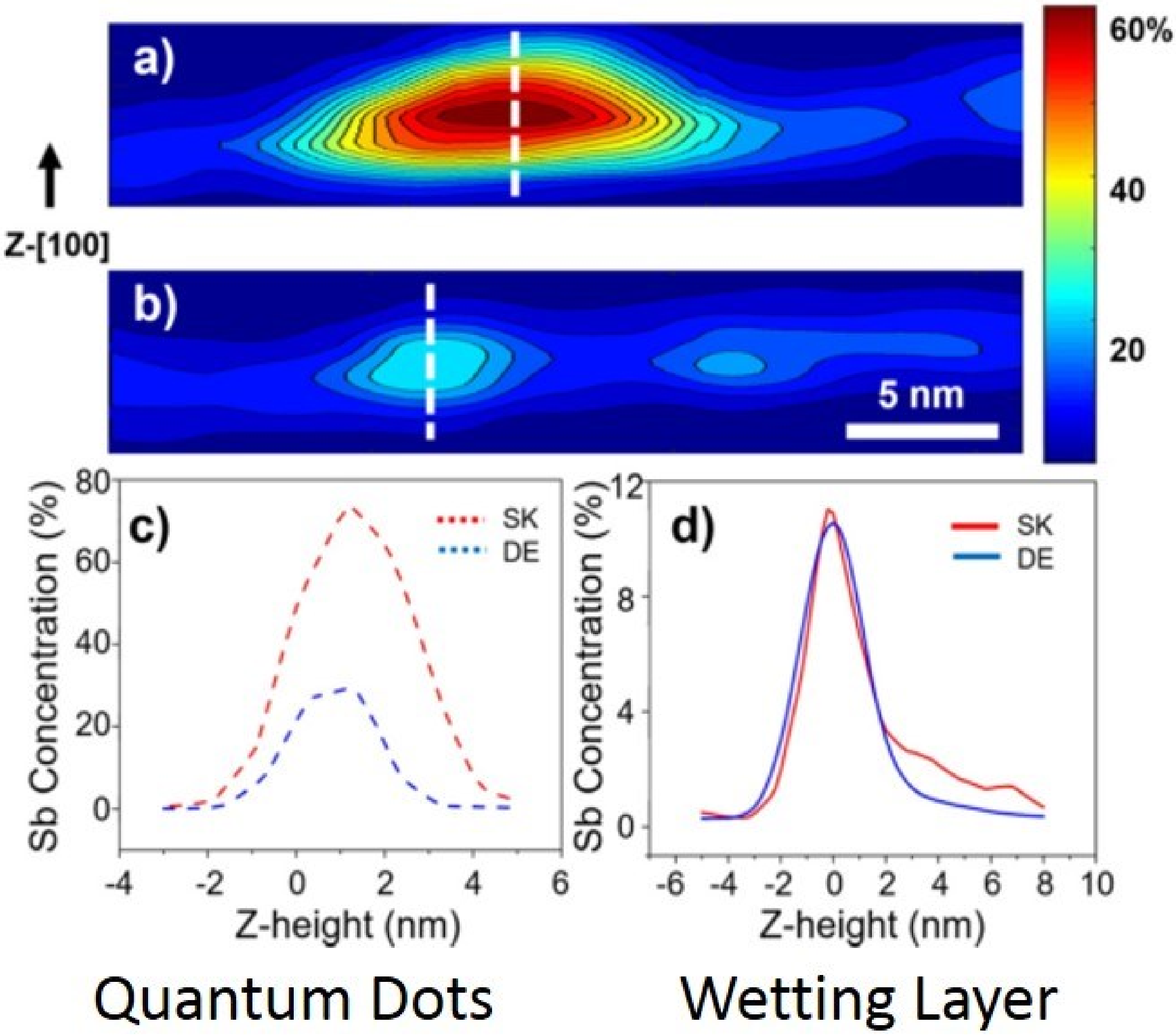

Figure 4-11. Cross sectional profile of (a) SK QD and (b) DE QDs. Linear Sb composition profile of (c) QDs and (d) wetting layer.

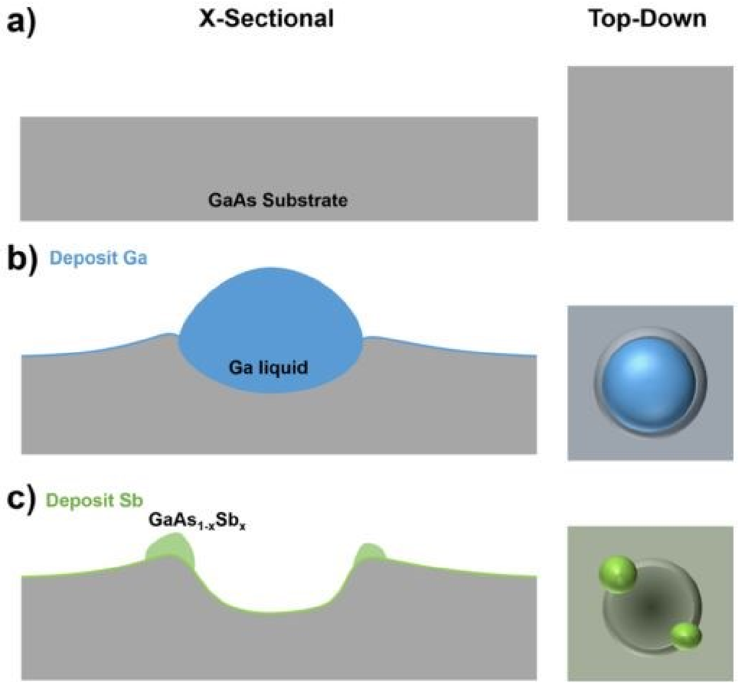

Figure 4-12. Schematic detailing the (a) initial substrate, (b) droplet and ring formation, and (c) quantum dot formation stages of droplet epitaxy

Based on these observations, a possible formation mechanism for QD in the DE method is proposed, as shown in the schematic in Figure 4-12. The growth starts with a planar GaAs substrate and Ga droplets form on the surface. The Ga droplet can partially dissolve the GaAs substrate [18]. Part of the displaced substrate material migrates to the perimeter of the droplet. When exposed to the Sb flux, $GaAs_{1-x}Sb_x$ formed isolated QDs that nucleated on the opposite sides of the droplet to minimize their strain energy.

4.2.2 STEM Imaging and EELS

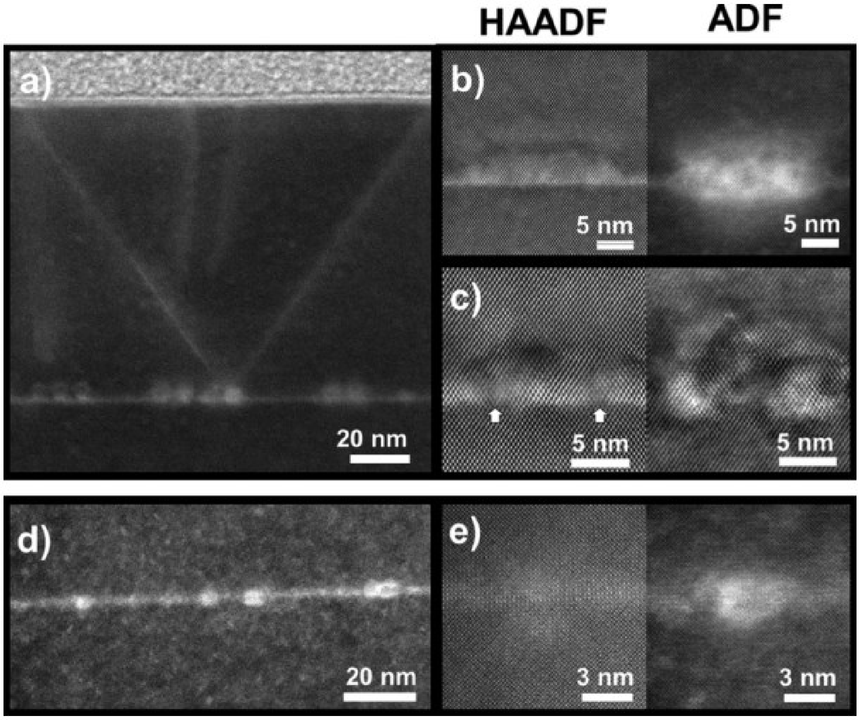

Figure 4-13. Cross-sectional TEM images of capped (a)–(c) SK and (d) and (e) DE nanostructures. High-resolution images of an (b) intact SK dot, a (c) defected SK dot and a (e) DE ring.

STEM is further utilized to characterize the morphology of both growth modes. Selected STEM images are shown in Figure 4-13. The low magnification image clearly shows a thin wetting layer of GaSb (Figure 4-13(a)); it also indicates GaAs capping layer can induce disintegration of GaSb QDs. The dislocation can propagate from the GaSb QD layer all the way to the surface of the sample. Figure 4-13(b) shows HAADF image and ADF for the same QD; this is a well-defined QD that was not broken by the capping layer. HAADF image shows the dimension of 20 nm in diameter and 5 nm in height. ADF image shows a contrast that is more affected by the lattice mismatch strain. On the other hand, Figure 4-13(c) shows HAADF and ADF image of a disintegrated GaSb QDs. Two dislocations are clearly observed at the interface between the GaAs substrate and GaSb QDs. ADF image shows the strain is larger due to the insertion of dislocations.

For DE growth sample, the low magnification TEM image shows the thin wetting layer with small QDs can be seen located on aligned on the wetting layer. The HAADF image does not show prominent shape of QDs because of its dimension is much smaller than SK QDs. ADF image gives a slight stronger contrast due to the strain introduced by these QDs.

Another major compositional analysis technique integrated with STEM is Electron Energy Loss Spectrum (EELS), which is also used to analyze the relative elemental composition of both samples. Figure 4-14 shows the EELS line profile cutting across the core of both kinds of QDs. The count for Ga remains constant across the data collection line, while there is a significant increment of Sb signal and a gradual decline after it reaches its peak value. The rise and fall of the Sb signal directly correlates to the QD nanostructure. For DE, the EELS spectra show a smaller peak(pit) of Sb(As). A rough estimation of EELS spectra gives the Sb composition of 80 ± 10% for SK QDs and 40 ± 10% for DE QDs.

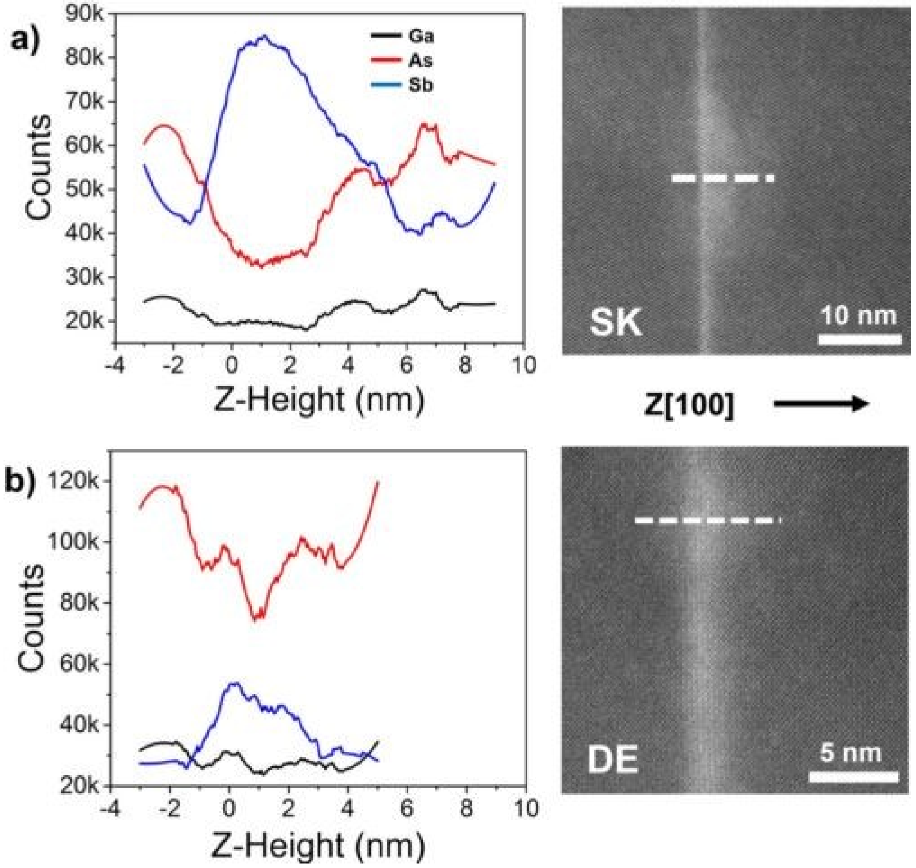

Figure 4-14. EELS profiles along lines shown in the TEM images for the (a)SK and (b) DE quantum dots

4.2.3 Summary

For this project, APT, TEM, and EELS are all applied to characterize the GaSb QD structure, presenting their strengths and weakness. APT is particularly useful in getting information in three dimensions. It is sensitive to concentration as low as 1 %. APT has its advantage of showing compositional profile only. DE growth mode QD sample is a great example for demonstrating this point: it only shows pairs of QDs located on the perimeter of rings and is not subjected to structural contrast like STEM. It helps clear the question of how the quantum rings form. On the other hand, the dimension of QDs and core concentration suffer from artifacts. As discussed earlier, heterostructure QDs data sets have trajectory aberration issue. QD dimensions in X and Y direction seems to be subjected to larger aberration than in Z direction for this case.

4.3 Combining APT and STEM in Nanostructure Characterization

Chapter 2 and 3 compare and contrast APT with STEM in studying the compositional inhomogeneities in multiple semiconductor nanostructures.

HAADF imaging in STEM is strong at giving precise atomic resolution structural information, while APT is inaccurate when profiling interfacial composition. This is proved in the investigation of thin layer samples as well as buried quantum dot samples. The 30-nm thick InGaN bulk layer sample has proved that APT would give an interfacial thickness of 1.5 nm even though HAADF indicates an atomic abrupted interface. The interfacial thickness measured in APT probably originates from the *roll-up effect*, which is inevitable during the evaporation of atoms. This *roll-up effect* also affects the FWHM of the In peak in In(Ga)N thin layer sample. For GaSb QDs, only HAADF STEM image can give precise cross sectional structural information. Dislocations and wetting layers can be clearly seen. For GaAsBi bulk layer sample grown under low temperature, HAADF STEM image gives a clear triangular shape for Bi-rich precipitates and gives atomic resolution structural information on pores formed on the surface. APT is only capable of telling there is lateral compositional modulation and elliptical shape Bi-rich precipitates.

It is shown that APT is capable of distinguish composition fluctuation due to random alloy fluctuation, clustering, and intermixing. The absolute value of the average composition as well as its error changes with different data sets. A reliable method to determine composition fluctuation situation in APT would be using the Pearson coefficient. A case with mainly random alloy composition fluctuation gives a Pearson coefficient of 0.1 and the sample presenting nano-size clustering gives value of 0.3. Multi-thin layer InGaN/GaN sample is investigated and found that APT can also be used to determine the existence of intermixing. The intermixing of In during the growth of multiple InGaN layers present as asymmetric peak shape and In ion density projected over the cross sections.

The accuracy of the APT results in buried QDs nanostructures can be affected by trajectory aberration, which mainly due to the difference in evaporation field for different materials. The total ion density for the cross section is lower at the position of Ge QDs, indicating Ge has a higher evaporation field than the AlAs matrix. The nonuniform evaporation can cause shape, size and QD core concentration distortion. Indeed, it is observed that Ge QDs in APT have an elliptical shape even though STEM images suggest a spherical shape. The size distribution measured by APT for these QDs is also largely limited by the small volume that is possible to be measured. Within these QDs, Ge core concentration ranges from 16% to 90% based on their size.

However, APT has its own advantages. Firstly, the data set shows 3D compositional contrast. This is illustrated in the comparative growth study of GaSb QDs with GaAs capping layer. While AFM of DE QDs suggests quantum ring, the APT data reveals it forms pairs of two small QDs residing on the perimeter of these rings. Secondly, APT has higher sensitivity in small compositional fluctuation compared to STEM. A sample might seem uniform under the STEM image while APT tells a different story. This is demonstrated in GaAsBi bulk layer sample. The fact that HAAD STEM image seems uniform might be due to its small variation and STEM image is projecting the 3D compositional information onto the 2D plane. However, APT indicates a non-uniform Bi incorporation, with minor lateral composition modulation and Bi-rich precipitates possible.

For a better understanding of compositional inhomogeneities within buried QD nanostructures, APT and STEM results should be combined. APT is sensitive to composition variation with higher spatial resolution in 3D. The disadvantage of APT is that it only examines a small area, usually smaller than 100 nm * 100 nm *500 nm. On the other hand, STEM data are particular useful in determining the feature size accurately. The atomic resolution HAADF image makes it possible to precisely measure the feature size while imaging a larger area, the area of examination can go up to a few square microns. However, the resolution for compositional analysis in STEM can largely affected by experiment conditions and data analysis. EDS mapping usually has a resolution of 2 nm, and these maps are compositional information in 3D projected on the 2D plane. Using EELS might achieve higher resolution, but precise estimation of composition requires calibration and advanced EELS data analysis skills.

4.4 References

1. Petroff, P. M., Gossard, A. C., Savage, A. & Wiegmann, W. Molecular beam epitaxy of Ge and Ga1−xAlxAs ultra thin film superlattices. *J. Cryst. Growth* **46,** 172–178 (1979).

2. Kuan, T. S. & Chang, C. -a. Electron microscope studies of a Ge–GaAs superlattice grown by molecular beam epitaxy. *J. Appl. Phys.* **54,** 4408 (1983).

3. Hudait, M. K., Zhu, Y., Jain, N. & Hunter, J. L. Structural, morphological, and band alignment properties of GaAs/Ge/GaAs heterostructures on (100), (110), and (111)A GaAs substrates. *J. Vac. Sci. Technol. B, Nanotechnol. Microelectron. Mater. Process. Meas. Phenom.* **31,** 11206 (2013).

4. Venables, John. *Introduction to surface and thin film processes*. Cambridge University Press, 2000.

5. Morizane, K. ANTIPHASE DOMAIN STRUCTURES IN GaP AND Gabs EPITAXIAL LAYERS GROWN ON Si AND Ge. *J. Cryst. Growth* **3,** 249–254 (1977).

6. O'Brien, W. A. *et al.* Self-assembled Ge QDs Formed by High-Temperature Annealing on Al(Ga)As (001). *J. Electron. Mater.* **44,** 1338–1343 (2015).

7. Gault, B., Moody, M. P., Cairney, J. M. & Ringer, S. P. *Atom Probe Microscopy*. **160,** (2012).

8. Mulholland, M. D. & Seidman, D. N. Nanoscale co-precipitation and mechanical properties of a high-strength low-carbon steel. *Acta Mater.* **59,** 1881–1897 (2011).

9. Kawai, T., Yonezu, H., Yoshida, H. & Pak, K. Ge segregation and its suppression in GaAs epilayers grown on Ge(111) substrate Ge segregation and its suppression in GaAs epilayers grown on Ge(lll) substrate. *Cit. Appl. Phys. Lett* **61,** (1992).

10. Hatami, F. *et al.* Radiative recombination in type ‑ II GaSb/GaAs quantum dots. *Appl. Phys. Lett.* **67,** 656–658 (1995).

11. Hatami, F. *et al.* Carrier dynamics in type-II GaSb/GaAs quantum dots. *Phys. Rev. B* **57,** 4635–4641 (1998).

12. Nowozin, T. *et al.* Linking structural and electronic properties of high-purity self-assembled GaSb/GaAs quantum dots. *Phys. Rev. B - Condens. Matter Mater. Phys.* **86,** 1–6 (2012).

13. Smakman, E. P. *et al.* GaSb/GaAs quantum dot formation and demolition studied with cross-sectional scanning tunneling microscopy. *Appl. Phys. Lett.* **100,** 142116 (2012).

14. Martin, A. J. *et al.* The disintegration of GaSb/GaAs nanostructures upon capping Atom probe tomography analysis of different modes of Sb intermixing in GaSb quantum dots and wells The disintegration of GaSb/GaAs nanostructures upon capping. *Cit. Appl. Phys. Lett. Appl. Phys. Rev. Appl. Phys. Lett. J. Appl. Phys.* **102,** 113103–21302 (2013).

15. Liang, B. *et al.* GaSb/GaAs type-II quantum dots grown by droplet epitaxy. *Nanotechnology* **20,** 455604 (2009).

16. Dejarld, M., Reyes, K., Smereka, P. & Millunchick, J. M. Mechanisms of ring and island formation in lattice mismatched droplet epitaxy. *Appl. Phys. Lett.* **102,** (2013).

17. Lin, W.-H., Wang, K.-W., Lin, S.-Y. & Wu, M.-C. Temperature-dependent photoluminescence and carrier dynamics of standard and coupled type-II GaSb/GaAs quantum rings. (2013). doi:10.1016/j.jcrysgro.2012.12.069

18. Reyes, K. *et al.* Unified model of droplet epitaxy for compound semiconductor nanostructures: Experiments and theory. *Phys. Rev. B - Condens. Matter Mater. Phys.* **87,** 1–14 (2013).

19. Kawazu, T., Mano, T., Noda, T. & Sakaki, H. Optical properties of GaSb/GaAs type-II quantum dots grown by droplet epitaxy. *Appl. Phys. Lett.* **94,** (2009).

20. Martin, A. J. *et al.* Atom probe tomography analysis of different modes of Sb intermixing in GaSb quantum dots and wells. *Appl. Phys. Lett.* **103,** 122102 (2013).

Part II Impact of Composition on Crystal Shape, Defect Formation and Optical Properties

Chapter 5 From Pure GaN nanowires to InGaN/GaN Heterostructure Nanowires[‡]

5.1 Motivation and Background

GaN-based heterostructures are excellent candidates for a variety of electronic and optoelectronic devices. In addition to the direct bandgaps and high carrier mobilities, alloys of III-nitrides offer bandgap tenability from infrared (InN = 0.7eV) to ultraviolet (GaN = 3.4eV) photon energies. [1] However, the growth of InGaN alloy is a challenge, the bulk InGaN film is known for its high threading dislocation density and phase separation nature. Despite all the defects, it is still possible to exhibit intense electroluminescence (EL) or photoluminescence (PL) peaks from them. [2, 3]

[‡] This chapter is based on the publication "Structural and optical properties of disc-in-wire InGaN/GaN LEDs", (L Yan, et al., Nano Letters) and has been reformatted to departmental guidelines

More than ten years ago, people started to grow III-Nitride nanowires, trying to prevent dislocation formation due to lattice mismatch between InGaN alloy and planar substrate. [4,5,6] Nitride nanowires can be tailored into both axial or radial heterostructure. They are excellent nanostructured materials both regarding nanowire devices as well as physical structure for other complex geometries. Electronic homojunctions and heterojunctions can be generated either radially or axially. InGaN/GaN axial nanowire provides a promising option. [7] Defects such as threading dislocations, screw dislocations and mixed dislocations arising from the coalescence of slightly disorientated growing grains. In fact, NWs can be viewed as an ensemble of vertically-elongated grain of high quality material. [8] Unlike quantum dots, the axial nanowire Light-Emitting Diodes (LEDs) facilitate lateral strain relaxation so that higher Indium incorporation is possible. It has been theoretically predicted that NW structure might drastically increase the critical thickness of lattice-mismatched heterostructures. [9] Thus far, high quality III-Nitride Nanowires have been successfully fabricated in multiple groups using MBE. [10,11,12,13,14,15,16,17,18,19,20]

This chapter focuses on the structural and optical properties of InGaN nanowire heterostructure. This study examines the role of composition inhomogeneity in defect formation, and the resulting optical properties of InGaN/GaN nanowire LED structures on Si (111). Results for pure GaN nanowires will be first presented, for there is no compositional inhomogeneity issue. TEM data for nanowires grown with different coverage are then examined. Cathodoluminescence (CL) measurements show that all heterostructure nanowire samples exhibit broad emission around the intended energy, 1.95eV (635nm). While the absolute emission intensity is difficult to compare for CL measurement, the bandgap emission ~3.4eV (365 nm) coming from the GaN root is more pronounced as coverage of nanowires decreases, which has less coalescence formation. The width of the emission peak is likely due to variations in the morphology of the InGaN discs within the wires, as faceted layers with different thicknesses and quantum dots are observed by Transmission Electron Microscopy. Non-epitaxial 6-fold symmetric lateral branching, called "nanocrowns," emanate from stacking faults within the active regions. These features likely reduce optical emission as a result of grain boundaries between the nanocrown and nanowire.

The optical properties are examined via Cathodoluminescence (CL) microscopy on an FEI Quanta FEG SEM equipped with a Gatan MonoCL4 at an accelerating voltage of 5kV. The spectrum and wavelength filtered images are collected under room temperature. It is hard to compare the absolute value of the CL spectrum intensity since the height of from the sample to the pole piece is adjusted to acquire enough counts for the CL detector. All spectra are analyzed and fitted using Optical Fit 15.02. The structures of the nanowires are studied using a JEOL 3011 High-Resolution Transmission Electron Microscope (HRTEM) at 300kV. The TEM sample is prepared using the scratch-off and disperse method mentioned in Chapter 2.

5.2 Pure GaN Nanowires

GaN nanowires grown by plasma-assisted molecular beam epitaxy (PA-MBE) have been well studied before. [21,22] These nanowires are grown on a Si (111) substrate using PA-MBE as described previously. [23] The nanowire growth is initiated under N-rich conditions. Pure GaN nanowires are grown using a Ga flux of $1.46\text{x}10^{-7}$ Torr and 800 °C for 250 mins (Sample A).

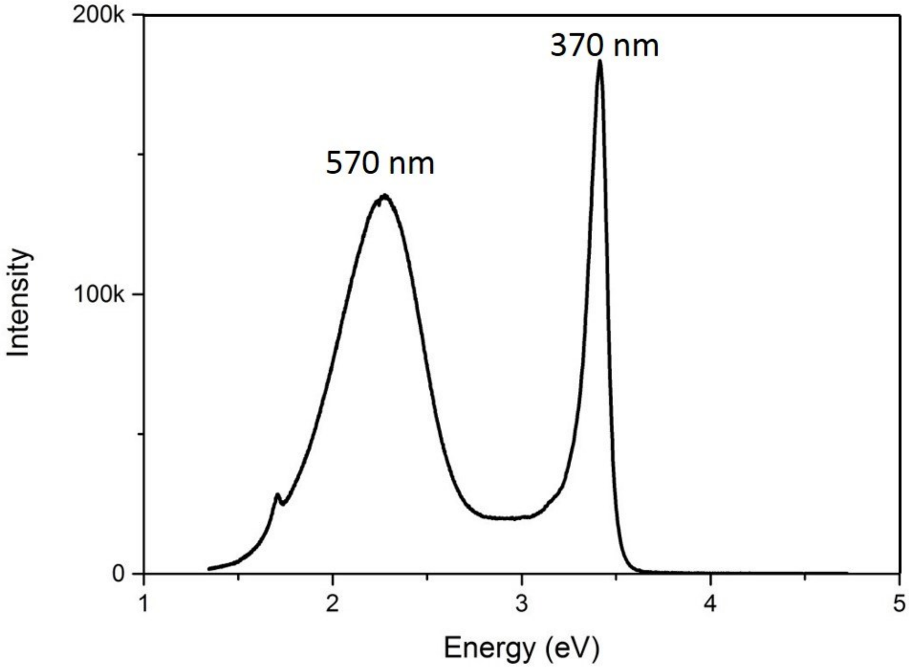

Figure 5-1. CL Spectrum of pure GaN nanowires (Sample A).

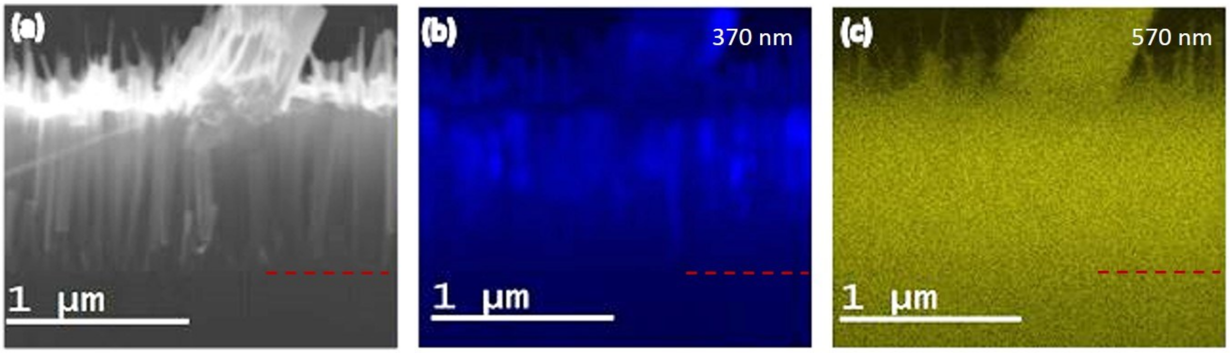

Figure 5-2. (a) Cross sectional SEM image of pure GaN nanowires (b) mono wavelength CL image at 370 nm (c) mono-wavelength CL image at 570 nm.

The room temperature CL spectrum is shown in Figure 5-1. GaN bandgap emission is located at 3.38 eV (366.8 nm) with small FWHM of about 0.1 eV, in which the value is consistent with room temperature GaN bandgap value (3.4 eV). The bandgap emission shows an asymmetric shape with the side peak at 3.21 eV (386 nm), which is 0.17eV separated from the identified GaN bandgap emission. Another broad peak is fitted at 2.16 eV (574 nm), with FWHM of ~ 0.7eV. GaN bandgap emission being the most intense emission in the CL, whose peak intensity of ~1.2 times of intensity from the broad peak. Mono wavelength CL images (Figure 5-2) are shown next to the cross-sectional SEM image for E = 3.4eV (~370 nm) and E = 2.17eV (~570 nm). The interface between the substrate and nanowire is labeled with red dash lines. Pure GaN nanowires have strong emission at the upper half of these nanowires. GaN emission is quenched at the lower half of these nanowires due to the high density of defects at the interface between the substrate and nanowires [24]. Emission at 2.17eV (570 nm), distributes uniformly among the nanowires, are likely due to defects within the nanowires. [25]

Both low magnification and high magnification Bright Field TEM images are shown in Figure 5-3. The arrow in Figure 5-3(a) indicates the growth direction of these nanowires. Low-mag TEM image shows GaN nanowires have a uniform diameter of less than 100 nm. Occasionally, stacking faults across the nanowire can be seen and is pointed out by an arrow in the high resolution TEM image (Figure 5-3 (b)).

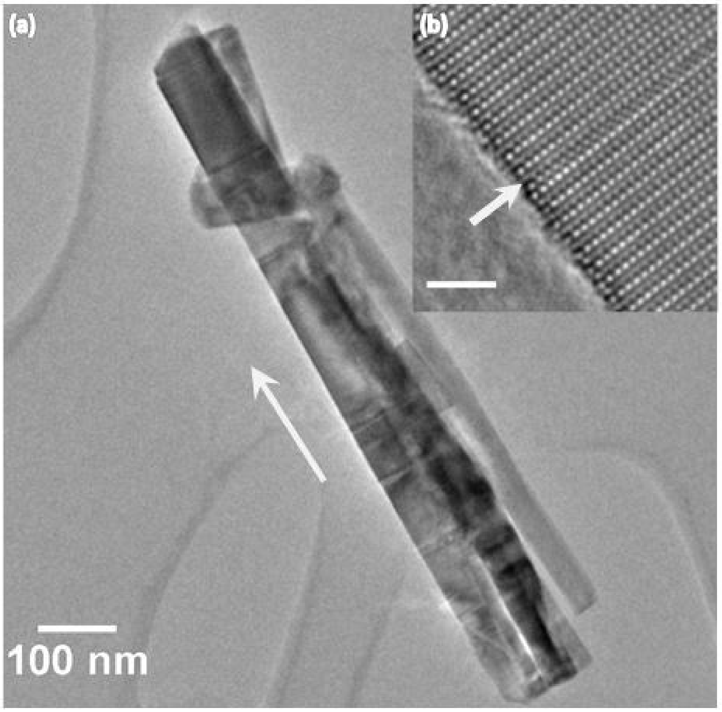

Figure 5-3. (a) Low Magnification Bright Field TEM image of pure GaN nanowire showing several stacking faults. (b) High Resolution Bright Field TEM image is showing the atomic structure of the stacking fault. The scale represents length of 2nm.

To identify the peak with emission at 2.17 eV (570 nm), another pure GaN nanowire sample (Sample A2) is grown with a much lower growth temperature at 550 °C at the upper half of the nanowires, while the lower half used high growth temperature of 800 °C. The CL spectrum collected is shown in Figure 5-4(a). Compared to Sample A, the intensity of the GaN bandgap emission is much weaker. The intensity of the nanowire emission at 2.17 eV (570 nm) is about ten times of the GaN bandgap emission. Fitting results show the GaN bandgap peak locates at 3.4 eV (370 nm), and slightly broaden to an FWHM of 0.15 eV. The broad peak is fitted at 2.1 eV (590 nm), with the same FWHM of 0.7 eV.

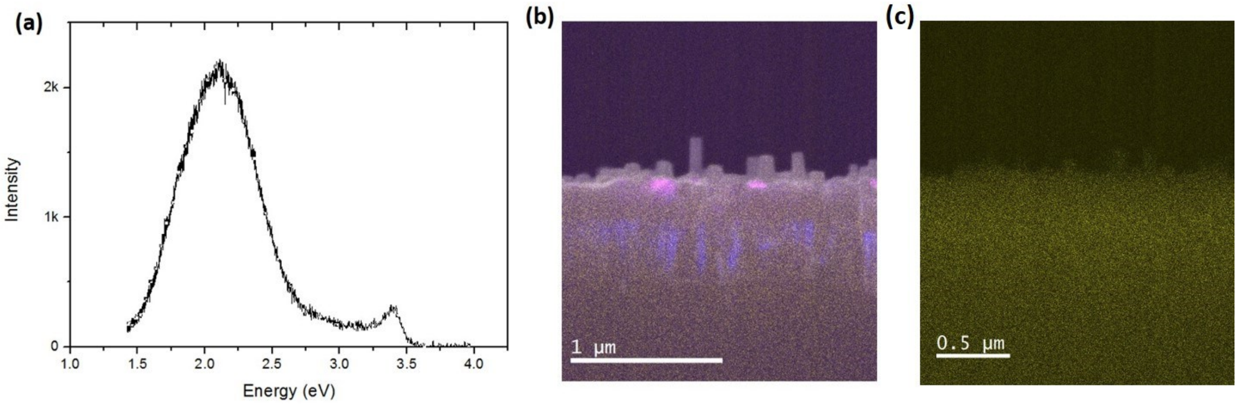

Figure 5-4. (a) CL Spectrum of GaN nanowire sample grown at 550°C (Sample A2) (b) Cross sectional over layered CL image with SEM image (c) monowavelength CL image with filter centered at 2.14 eV (570 nm)

Figure 5-4 (b) shows the 365nm emission locates at the lower half where nanowires are grown with 800 ℃, denoted by blue. The mono wavelength CL image for 2.17 eV (570 nm) is diffused all over the whole nanowire area, similar to Figure 5-2(c). It is also noticed that there is a weak emission which peaks at 3eV (400 nm), denoted by pink color in the over layered CL image. The mono wavelength CL image pins this emission at the very tip of some nanowires. It is possible that peak arises due to a specific facet on the nanowire tip. [26]

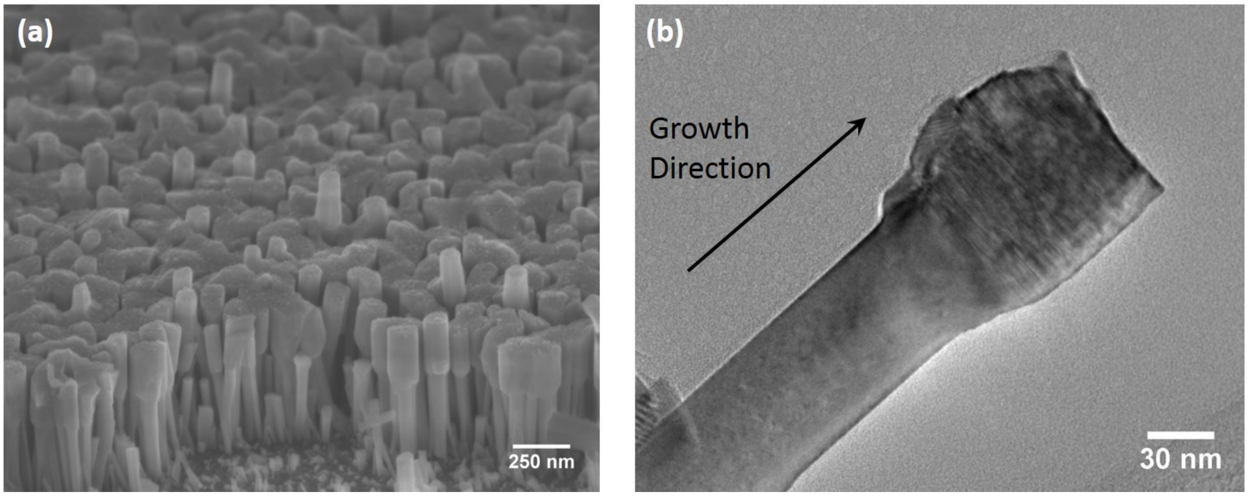

Figure 5-5. (a) 52 tilted SEM image of sample A2. (b) low magnification TEM image of sample A2.

Figure 5-5 (a) is the tilted SEM image showing the morphology of nanowires in Sample A2. The upper half section of these nanowires, grown at 550°C, is much wider than the lower half section. The diameter increases due to the enhanced radial growth when grown at a lower temperature. The promoted radial growth increases the chance for nanowire coalescence, leading to a connected film. Indeed, it has been reported as a technique to create high quality GaN substrate. The nanowire-templated lateral epitaxial growth (NTLEG), uses vertical GaN arrays to relieve the strain between the sapphire substrate and bulk GaN, make it possible to grow low dislocation density GaN film. [27] A Growth study on pure GaN nanowire has been conducted before by Fernández-Garrido et al. on samples grown with varying Ga flux. [28] They found that an increase in Ga flux significantly promotes radial growth without affecting axial growth, this leads to a drastic increment of the nanowire diameters. They interpret this observation using a kinetic model in which nanowire axial growth rate is limited by the number of N atoms available, which can be controlled by altering III/V ratio. On the other hand, the radial growth is limited by a combination of the Ga adatom diffusion length and the number of N atom available.

The TEM image (Figure 5-5 (b)) shows high resolution of a single nanowire. It can be seen from the TEM image that upper half portion of the nanowire has a much higher density of stacking faults. This observation also suggests that GaN nanowire radial growth is kinetically limited; the Ga adatoms do not diffuse as far as at a higher temperature. Secondary growth of incoherent 3D islands on the nanowire sidewall is also observed, suggesting that the lowered growth temperature can also induce lateral branching.

5.3 InGaN/GaN heterostructure nanowire LEDs

The LEDs based on InGaN/GaN heterojunctions are designed to emit light at about 1.95 eV (635 nm). They consist of 300 nm of n-type GaN grown at ~800 °C, followed by eight periods of ~2-3 nm InGaN layers with a composition of nominally 53%. The EDS measurements Indium composition ~46%. The InGaN disks are separated by 12 to 15 nm thick GaN barriers grown at 545- 560 °C. The final capping layer includes 200 nm thick p-type GaN grown at 700 °C. The Ga flux used for the growth of GaN regions in the nanowire LED heterostructure varied between 1.46 $<F_{Ga}<1.94 \times 10^{-7}$ Torr, while the In flux used for growth of active region is approximately 8×10^{-8} Torr. The fluxes are adjusted to maintain a flux ratio of approximately 43% (Table 5-1).

Sample	Ga flux	In flux	Nanowire Morphology	
	Torr	Torr	% Coverage	Average Diameter（nm）
A	1.46×10^{-7}	--	53	90±13
B	1.94×10^{-7}	8.8×10^{-8}	72	84±12
C	1.64×10^{-7}	8.3×10^{-8}	46	96±7
D	1.46×10^{-7}	8.1×10^{-8}	30	140±14

Table 5-1. Growth parameters and morphologies of InGaN/GaN heterostructure nanowire

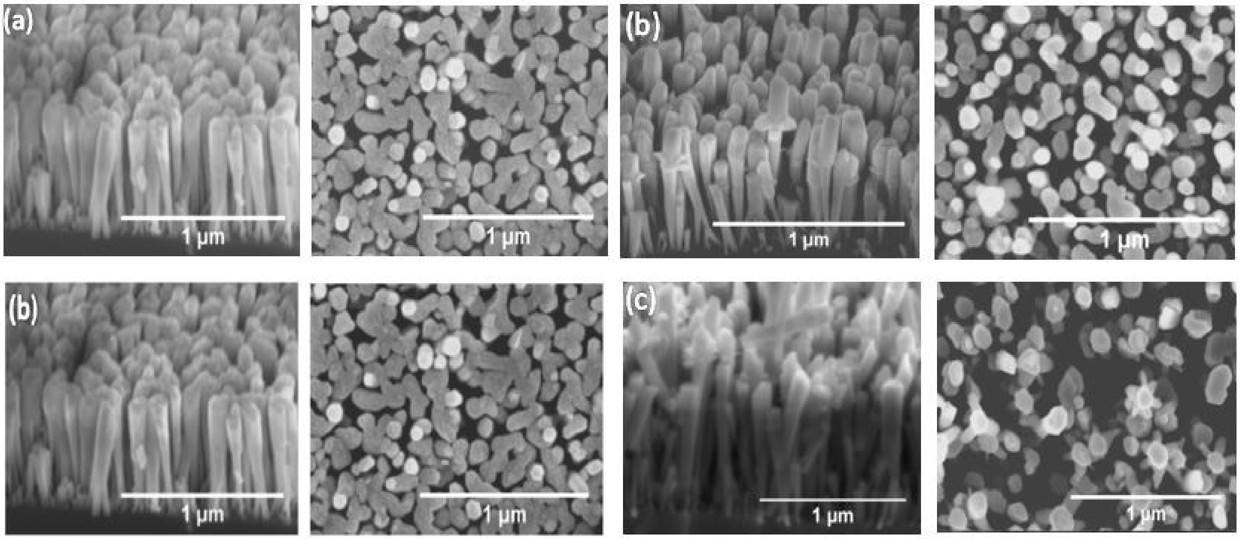

Figure 5-6. Side and top view SEM images of InGaN/GaN nanowire LED structures grown at 800 °C and with a Ga flux of (a) 1.46 × 10-7 Torr grown of pure GaN nanowire (b) 1.94× 10-7 Torr (Sample C) (c) 1.64 × 10-7 Torr (Sample C), and (d) 1.46× 10-7 Torr (Sample D) with substrate temperature of 800 °C.

Figure 5-6 shows edge-on and plan-view Scanning Electron Micrographs (SEM) of nitride nanowires grown under various Ga and In fluxes (see Table 5-1). Sample A consists of pure GaN wires with an average areal coverage of 53%. The wires have a hexagonal cross section, as expected for plasma-assisted MBE of these structures [29] and have a diameter of 90±13 nm. Examination of the base of the nanowires shown in Figure 5-6 shows that narrow wires form initially that coalesce into larger diameter wires with increasing length. Samples B-D are full LED structures grown under various Ga fluxes, which has the effect of altering the coverage of the wires, as seen in Table 5-1. In general, decreasing the Ga flux decreases the coverage of wires and increases their diameters. [30] For instance, decreasing the Ga flux from $1.94\text{x}10^{-7}$ Torr to $1.46\text{x}10^{-7}$ Torr, results in a decrease of the coverage of 72% to 30%, and increases the average nanowire diameter of from 84±12nm to 140±14nm.

Room temperature CL is taken for three nanowire LED samples in order to study the local optical properties. The CL spectrum can be seen as the combination effect coalescence defects, which quench the emission, and the absolute number of nanowires, which tends to boost the emission. Also, the absolute emission intensity can be affected by the crystal quality and efficiency of light extraction. Figure 5-7 shows the CL spectrum with the cross-sectional SEM image and their corresponding layered CL image. CL spectrum for Sample B has only one broad peak located at ~2 eV (620 nm), which is close to the target wavelength. SEM and layered CL image indicate major emission from the active region. For Sample C, the broad peak at target wavelength split, with a weak emission at 3.4 eV (365 nm). Emission centered at 1.95 eV (620 nm) is false colored red and the emission at 3.4 eV (365 nm) is colored blue in the overlayered CL images. The sample with most sparse nanowires, has strong emission at the target wavelength as well as a still weak emission at 3.4 eV (365 nm). There is no GaN bandgap emission for Sample B, weak emission for Sample C and strongest emission for Sample D. A possible explanation for this is that coalescence during nanowire growth, and the accompanying defects, play a major role. The sample with the highest nanowire coverage has the highest degree of coalescence, and thus the highest number of defects that act as nonradiative recombination centers that decrease the GaN bandgap emission. While Sample D, with the lowest nanowire coverage, has the strongest relative bandgap emission because of the low degree of coalescence.

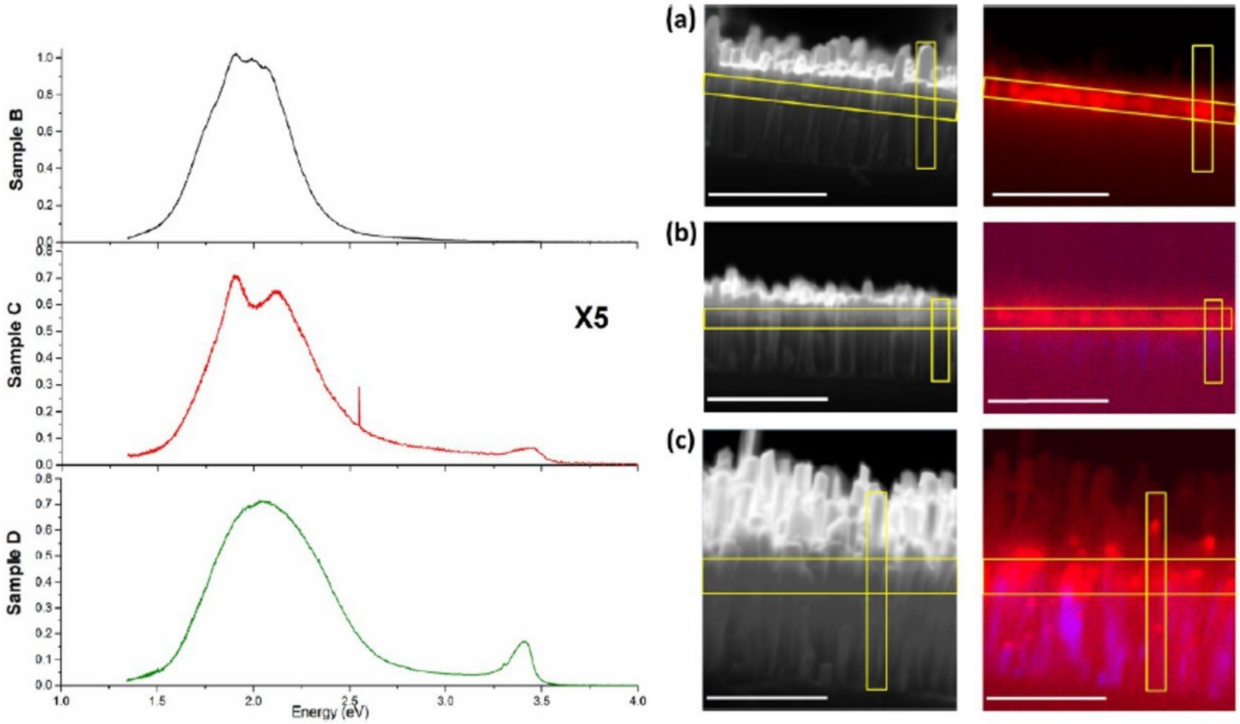

Figure 5-7. Cathodoluminescence spectrum of InGaN/GaN nanowire LED structures (left) and Cross section over layered CL image (left) and SEM image (right) of InGaN heterostructure-nanowire (a) Sample B (b) Sample C and (c) Sample D (right). The scale bar represents the length of 1 μm.

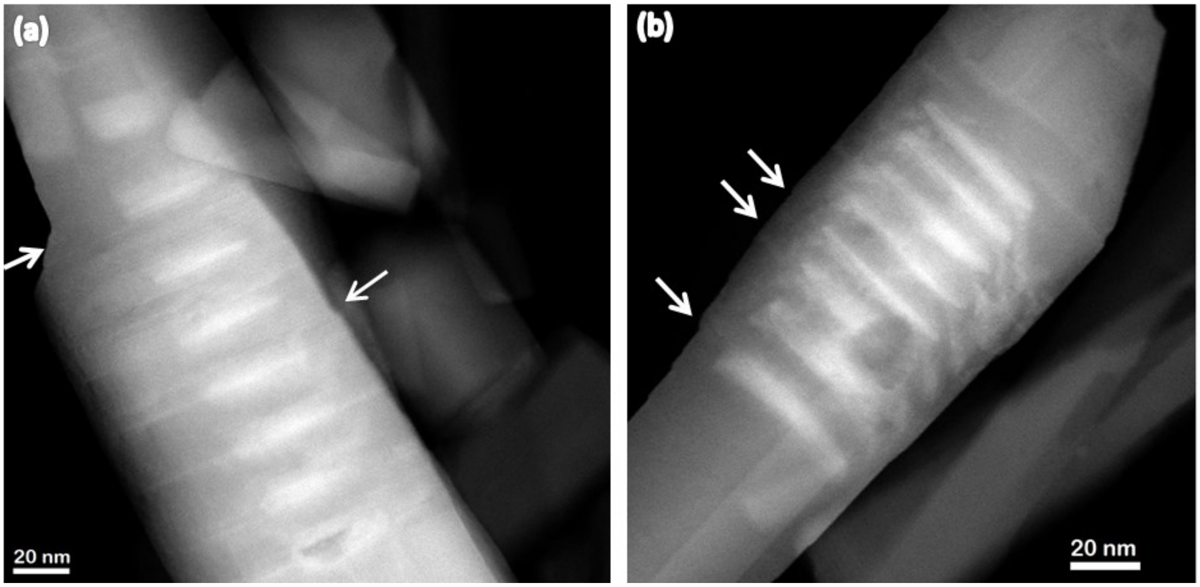

Figure 5-8. HAADF image of InGaN heterostructure wire structures. (a) strain-driven InGaN quantum dots with faceting (arrowed). (b) Faceted InGaN layers (arrowed)

High Angle Annular Dark Field STEM is performed on InGaN heterostructure wire heterostructures to study the compositional homogeneity. The diameter of both nanowires increases along their length via faceting of the sidewalls (indicated in Figure 5-8) either due to the introduction of In or to the reduced growth temperature at this region. Figure 5-8(a) shows a nanowire that contains a series of InGaN/GaN multilayers with aligned quantum dots running through the center of the wire. While it is well known that nanowires are highly efficient at relieving lattice mismatch strain [9], the amount of strain relaxation depends on the lattice mismatch and the diameter of the wire. For instance, it is expected that for a lattice mismatch of 5%, the mismatch between the InGaN and GaN layers in these structures can be completely accommodated for nanowires less than 80nm in diameter. The average size of the nanowires studied here are somewhat larger (Table 5-1). Therefore, it is likely that the dimensions of the wire alone cannot accommodate the strain, resulting in strain-driven quantum dot formation.

Figure 5-8 (b) shows a nanowire from Sample D that has faceted interfaces at the InGaN interfaces. This morphology is observed somewhat more often than the quantum dots. Thinner InGaN is observed on the facet faces (arrowed), with thicker InGaN on the basal plane in the center of the wire. Faceting has been previously reported in this system, both for pure GaN growth and for InGaN growth, [27,28] and arises to reduce the polarization at the surface. The difference in the thickness between these layers occurs due to different growth rates on the two planes, and has been shown to result in distinct emission wavelengths in CL spectra. [7, 29] The variation in thickness, and possibly composition, of the InGaN layers arising due to these different interfacial structures contribute to the shape of the CL peaks. It is likely that each of these features emits at slightly different energies, and that the observed peak is the sum of these contributions. However, because these features (faceted disks and dots) appear in all of the samples to some degree, it is difficult to determine precisely which energy is associated with which morphology.

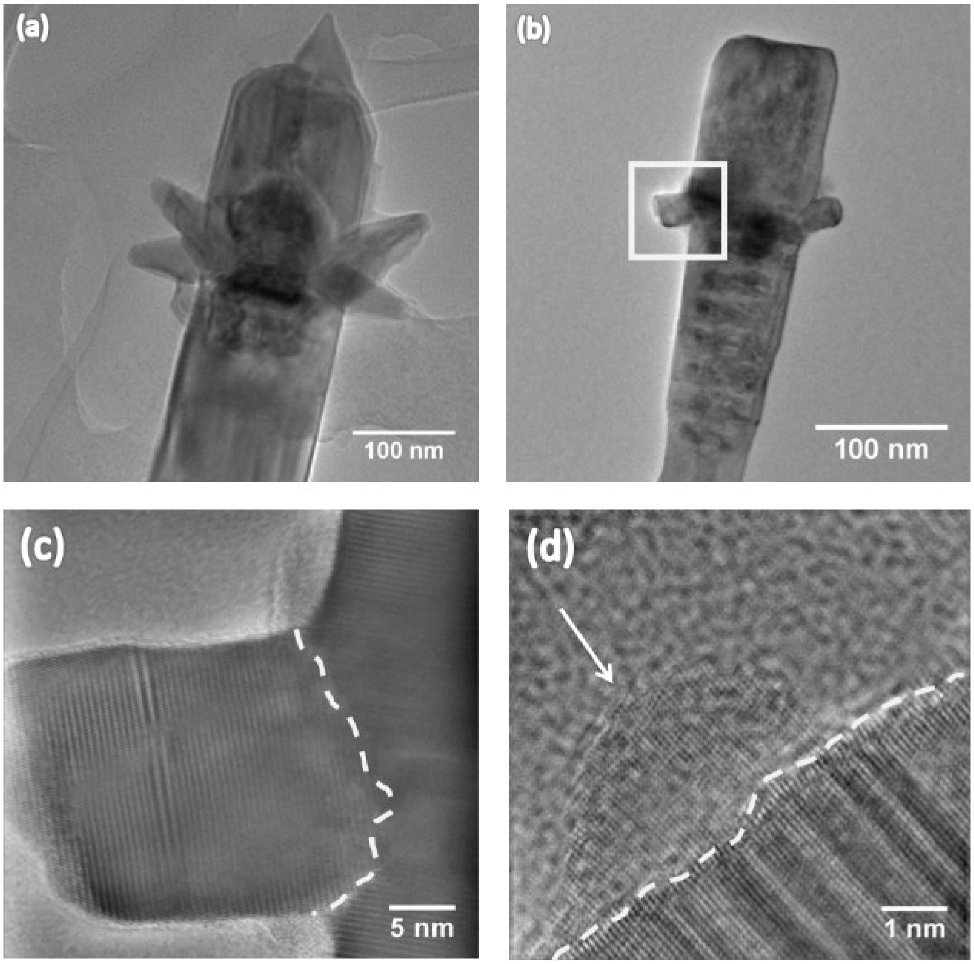

Figure 5-9. (a) Low magnification Bright Field image of a nanocrown (Sample D). (b) Low Magnification Bright Field image of a nanocrown in its early stages of formation (Sample C). (c) High Magnification Bright Field image of the feature boxed in (b) the arrows point out the grain boundary between the nascent nanocrown and the nanowire. (d) High Resolution Bright Field image of a nucleus that will develop into a nanocrown taken from Sample B.

The lowest coverage wires (Sample D) also exhibit 6-fold symmetric pyramidal structures on their sidewalls that we call “nanocrowns” (see Figure 5-6 & Figure 5-9(a)). But TEM shows that even the high-coverage samples exhibit nascent nanocrowns, suggesting that the formation of these structures does not depend on the Ga flux used, but instead form as long as the sidewall is accessible. Figure 5-9(b) shows a nanowire from Sample C, and shows faceted nubs within the active regions. Figure 5-9(c) is a higher resolution image of one of the nubs, and shows that it is not epitaxial with respect to the nanowire. That is, the basal plane of the nub is oriented perpendicular to its axis, not in registry with the nanowire. There is a clear grain boundary between the nub and the nanowire, as indicated by dashed line in Figure 5-9(c). Figure 5-9(d) is a high-resolution image of a nucleus on the sidewall taken from Sample D that is situated on stacking faults within the active region. Based on the observation so far, the lowered growth temperature and presence of In promote stacking faults occurrence. Facet nubs are formed on the sidewalls of these nanowires due to secondary growth. Lateral branches further develop from the facet nubs.

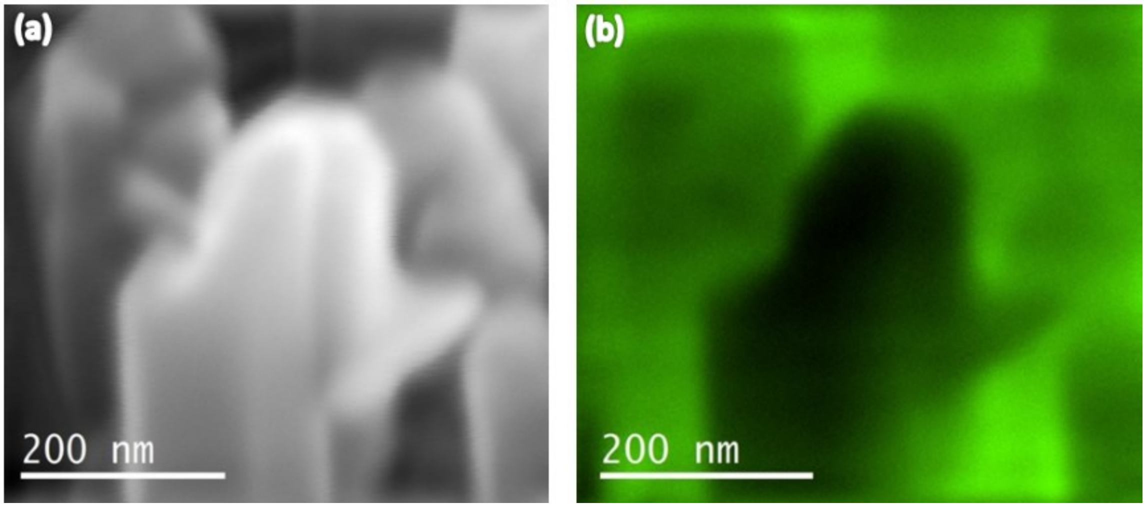

Figure 5-10. (a) SEM image of nanocrown and (b) CL image of the same area for wavelength range from 310 to 850nm.

The impact of the nanocrowns on the optical emission is studied using CL as well. Figure 5-10(a) shows a SEM micrograph of a nanocrown for a sample grown with a Ga Flux of 1.48×10^{-7} Torr and T= 800°C, that shows a nanocrown. Figure 5-10(b) shows the corresponding $310 < \lambda < 850$nm multiwavelength CL image and clearly demonstrates that the nanowire decorated with the nanocrown does not emit at all within the expected wavelength range. This indicates that the defects associated with the nanocrowns, most likely the grain boundaries, are a source of the deep electron and hole traps observed in temperature-dependent photoluminescence measurements. [31] It remains to be seen if these structures could emit light for larger nanocrowns, or by encapsulating them to form core-shell structures. A potential application of the nanocrowns could be to achieve horizontally interconnected nanowire arrays.

5.4 Summary

This chapter studies how structural defects and compositional inhomogeneities in InGaN/GaN nanowire affects the local optical properties.

Pure GaN nanowires have a distinct emission at 3.4 eV (~370 nm), which is consistent with GaN bandgap energy, and broad peak at 2.17eV (~570 nm). Mono wavelength CL image targeted at this wavelength shows a diffused distribution. Lowering the growth temperature would enhance radial growth. The stacking faults inserted also increases the chance of secondary growth on the nanowire sidewall. The CL image confirms coalescence defects quench GaN bandgap emission. The faceted tip surfaces contribute the emission around 3.1 eV (400 nm).

InGaN/GaN heterostructure nanowire LEDs emit at 1.95eV (635 nm), the intensity of the emission depends on the relative number of coalescence defects and the absolute number of emitting nanowires. TEM shows that the morphology of the InGaN layers varies from wire to wire, consisting of either quantum dots or faceted layers. This variation in the InGaN morphology likely results in the broad emission observed from the nanowires. TEM additionally shows that the nanowires also have stacking faults within the active regions, upon which a 6-fold finned structure referred to as “nanocrowns” may form. The nanocrowns themselves are not epitaxial, with respect to the nanowire, but nucleate as separate grains on the nanowire sidewalls. The crowned nanowires are shown not to be optically active under room temperature, suggesting that the grain boundaries are a source of the deep electron and hole traps.

The InGaN/GaN nanowires have present an interesting morphology with embedded quantum dots, facet layers as well as lateral branching. To achieve a better luminescence, it is recommended to take measures to decrease the appearance of faceted layers and lateral branching. This might be achievable with lower the growth rate or raising the growth temperature.

5.5 References

1. Wu, J. *et al.* Superior radiation resistance of alloys: Full-solar-spectrum photovoltaic material system *J. Appl. Phys.* **94,** 143502–132117 (2003).

2. Nakamura, S., Mukai, T. & Senoh, M. Candela-class high-brightness InGaN/AlGaN double-heterostructure blue-light-emitting diodes. *Appl. Phys. Lett.* **64,** 1687–1689 (1994).

3. Yamamoto, N. Development of Cathodoluminescence (CL) for Semiconductor Research , Part I : TEM – CL Study of Microstructures and Defects in Semiconductor Epilayers. 37–51 (2002).

4. Zhong, Z., Qian, F., Wang, D. & Lieber, C. M. Synthesis of p-type gallium nitride nanowires for electronic and photonic nanodevices. *Nano Lett.* **3,** 343–346 (2003).

5. Kuykendall, T., Ulrich, P., Aloni, S. & Yang, P. Complete composition tunability of InGaN nanowires using a combinatorial approach. *Nat. Mater.* **6,** 951–956 (2007).

6. Dong, Y. J., Tian, B. Z., Kempa, T. J. & Lieber, C. M. Coaxial Group III- Nitride Nanowire Photovoltaics. *Nano Lett.* **9,** 2183–2187 (2009).

7. Qian, F. *et al.* Gallium nitride-based nanowire radial heterostructures for nanophotonics. *Nano Lett.* **4,** 1975–1979 (2004).

8. Daudin, B. *et al.* Growth, structural and optical properties of GaN/AlN and GaN/GaInN nanowire heterostructures. *Phys. Procedia* **28,** 5–16 (2012).

9. Glas, F. Critical dimensions for the plastic relaxation of strained axial heterostructures in free-standing nanowires. *Phys. Rev. B* **74,** 121302 (2006).

10. Sanchez-Garcia, M. A. *et al.* The effect of the III/V ratio and substrate temperature on the morphology and properties of GaN- and AlN-layers grown by molecular beam epitaxy on Si(1 1 1). *J. Cryst. Growth* **183,** 23–30 (1998).

11. Yoshizawa, M., Kikuchi, A., Mori, M., Fujita, N. & Kishino, K. Growth of Self-Organized GaN Nanostructures on $\bf Al_{2}O_{3}(0001)$ by RF-Radical Source Molecular Beam Epitaxy. *Jpn. J. Appl. Phys.* **36,** L459–L462 (1997).

12. Araki, T., Chiba, Y., Nobata, M., Nishioka, Y. & Nanishi, Y. Structural characterization of GaN grown by hydrogen-assisted ECR-MBE using electron microscopy. *J. Cryst. Growth* **209,** 368–372 (2000).

13. Calleja, E. *et al.* Molecular beam epitaxy growth and doping of III-nitrides on Si(1 1 1): layer morphology and doping efficiency. at <www.elsevier.com/locate/mseb>

14. Kusakabe, K., Kikuchi, A. & Kishino, K. Characterization of Overgrown GaN Layers on Nano-Columns Grown by RF-Molecular Beam Epitaxy. *Jpn. J. Appl. Phys.* **40,** L192–L194 (2001).

15. Tu, L. W. *et al.* Self-assembled vertical GaN nanorods grown by molecular-beam epitaxy. *Appl. Phys. Lett. J. Appl. Phys.* **82,** (2003).

16. Kikuchi, A., Kawai, M., Tada, M. & Kishino, K. InGaN/GaN Multiple Quantum Disk Nanocolumn Light-Emitting Diodes Grown on (111) Si Substrate. *Jpn. J. Appl. Phys.* **43,** L1524–L1526 (2004).

17. Bertness, K. a. *et al.* Catalyst-free growth of GaN nanowires. *J. Electron. Mater.* **35,** 576–580 (2006).

18. Cerutti, L. *et al.* Wurtzite GaN nanocolumns grown on Si(001) by molecular beam epitaxy. *Cit. Appl. Phys. Lett* **88,** (2006).

19. Van Nostrand, J. E. *et al.* Molecular beam epitaxial growth of high-quality GaN nanocolumns. *J. Cryst. Growth* **287,** 500–503 (2006).

20. Calarco, R. *et al.* Nucleation and Growth of GaN Nanowires on Si(111) Performed by Molecular Beam Epitaxy. doi:10.1021/nl0707398

21. Sã Anchez-Pã Aramo, J., Calleja, J. M., Sã Anchez-Garcã, M. A., Calleja, E. & Jahn, U. Structural and optical characterization of intrinsic GaN nanocolumns. *Phys. E* **13,** 1070–1073 (2002).

22. Calleja, E. *et al.* Luminescence properties and defects in GaN nanocolumns grown by molecular beam epitaxy. *Phys. Rev. B - Condens. Matter Mater. Phys.* **62,** 16826–16834 (2000).

23. Jahangir, S., Mandl, M., Strassburg, M. & Bhattacharya, P. Molecular beam epitaxial growth and optical properties of red-emitting (λ = 650 nm) InGaN/GaN disks-in-nanowires on silicon. *Appl. Phys. Lett.* **102,** 71101 (2013).

24. Hersee, S. D., Rishinaramangalam, A. K., Fairchild, M. N., Zhang, L. & Varangis, P. Threading defect elimination in GaN nanowires. *J. Mater. Res.* **26,** 2293 (2011).

25. Li, Q. & Wang, G. T. Spatial distribution of defect luminescence in GaN nanowires. *Nano Lett.* **10,** 1554–8 (2010).

26. Gibart, P. *et al.* Gallium nitride heterostructures on 3D structured silicon Metal organic vapour phase epitaxy GaN-based light-emitting diodes on various substrates: a critical review. (2008). doi:10.1088/0957-4484/19/40/405301

27. Li, Q., Lin, Y., Creighton, J. R., Figiel, J. J. & Wang, G. T. Nanowire-templated lateral epitaxial growth of low-dislocation density nonpolar a-plane GaN on r-plane sapphire. *Adv. Mater.* **21,** 2416–2420 (2009).

28. Fernández-Garrido, S., Grandal, J., Calleja, E., Sánchez-García, M. a. & López-Romero, D. A growth diagram for plasma-assisted molecular beam epitaxy of GaN nanocolumns on Si(111). *J. Appl. Phys.* **106,** 2009–2011 (2009).

29. Lethy, K. J., Edwards, P. R., Liu, C., Wang, W. N. & Martin, R. W. Cross-sectional and plan-view cathodoluminescence of GaN partially coalesced above a nanocolumn array. *J. Appl. Phys.* **112,** 23507 (2012).

30. Consonni, V., Knelangen, M., Trampert, a., Geelhaar, L. & Riechert, H. Nucleation and coalescence effects on the density of self-induced GaN nanowires grown by molecular beam epitaxy. *Appl. Phys. Lett.* **98,** 71913 (2011).

31. Jahangir, S. *et al.* Red-Emitting (lambda = 610 nm) In0.51Ga0.49N/GaN Disk-in-Nanowire Light Emitting Diodes on Silicon. *IEEE J. Quantum Electron.* **50,** 530–537 (2014).

Chapter 6 Shape Evolution of High Lattice-Mismatched InGaN Nanowire Heterostructures[§]

6.1 Background

In-rich InGaN nanowires are an attractive solution for long wavelength emission. The high aspect ratio is proven to be effective in elastic strain relaxation, allowing more In to be incorporated while limiting extended defects. This chapter discusses how increment in In would affect the morphology, defect formation, and thereby the optical properties for these nanowires.

The growth of pure InN nanowire was first reported by Calleja et al. and the further investigated by Sarwar et al.. [1, 2] InN has a particular problem related to the fact that their growth is affected by significant In desorption. Under growth temperatures above 550°C, metallic In droplets would form on the substrate surface. Too low an Indium flux results in low growth rate. But increasing the Indium flux may only lead to thin InN layers with In droplets at the surface [1]. More recently,

---

[§] This Chapter is based on future publication "Shape Evolution of High Lattice Mismatched InGaN Nanowire Heterostructure", (L Yan et al., Journal of Electronic Materials) and has been reformatted to follow department guidelines growth studies show InN nanowire tapering is determined by temperature, III/V ratio and density of the nuclei. It is desirable to use optimized growth temperature, low III/V ratio and low density.

It is well known that In alters the crystal shape of nanowires. For low In concentrations, nanowire heterostructures growth occurs axially on the basal plane, resulting in disc-in-nanowires heterostructures (as seen in Chapter 5 and reference 3 [3]), which is shown schematically in Figure 6-1(a). As the In concentration increases the lattice mismatch also increases, such that the growth mode of the In-rich region may transition from layer-by-layer to 3D island nucleation within the nanowire [4] (Figure 6-1(b)), analogous to SK growth of quantum dots in planar epitaxial systems. Decreasing the substrate temperature has been shown to promote In incorporation, as well as the radial growth of nanowires. [5] Reducing the growth temperatures, while simultaneously increasing the In composition, shifts the primary growth directions away from the basal plane to pyramidal planes (Figure 6-1(c)). For example, it has been shown that pure InN nanowires can have their diameter increase largely during growth, resulting in inverted pyramids or pinhead structures. [6,7,8,](Figure 6-1(d)). The growth of $In_{0.8}Ga_{0.2}N$ on top of GaN nanowires similarly results in a drastic increase in diameters, which often leads to coalescence of the individual nanowires. [9]

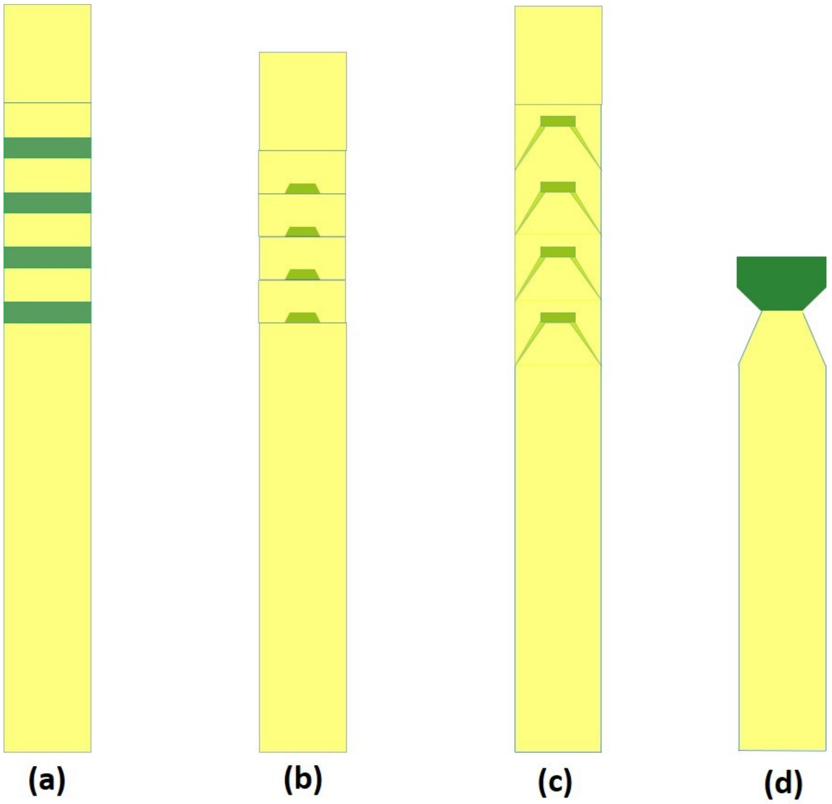

Figure 6-1. Schematics of nanowire heterostructure morphologies (a) disc-in-nanowire heterostructure (b) 3D island nucleation within nanowire (c) Quantum dot forming caused by pyramidal growth (d) pin head structure.

To date, the details about the structure of high lattice-mismatched InGaN nanowire heterostructures has not been fully understood. However, it is expected that the interaction of composition and temperature induced morphological changes and strain relaxation will have a high impact on the final shape and compositional distribution across the resulting nanowire arrays.

6.2 InGaN Nanowire Heterostructure

To understand the behavior of In-rich InGaN nanowire heterostructure, several nanowire samples are grown using Plasma Assisted Molecular Beam Epitaxy (PAMBE) using similar growth parameters to prior work. [10] Both nanowire heterostructures are grown on n-type (001) Si substrates. The growth temperature for Sample A are kept at 710 °C, the Ga flux is kept at 1.46

$\times 10^{-7}$ Torr while In flux is turned to 8 $\times 10^{-8}$ Torr for growth of InGaN disks and 0 for growth of GaN barrier layer. The final capping layer, a 200-nm thick GaN layer, is grown on the top of the active region. To incorporate more In, Sample B is designed with a 150-nm thick graded buffer layer after the GaN root. The GaN root is grown at 819 °C and the graded buffer layer is achieved by decrease the growth temperature from 819 °C to 631 °C in 10 steps. The active region is grown at temperature as low as 442 °C, $In_{0.85}Ga_{0.15}N$ disks are grown with In flux of 3×10^{-8} Torr and Ga flux of 1×10^{-8} Torr. The $In_{0.4}Ga_{0.6}N$ barrier layers are grown with In flux of 6 $\times 10^{-8}$ Torr and Ga flux of 2×10^{-8} Torr. The active region is then topped with 150 nm thick of GaN. Growth temperature and group III elements' fluxes used for Sample C are shown in Figure 6-2(a), and the intended nanowire structure assuming that the growth occurs entirely on the basal plane, is shown in Figure 6-2(b). The 260-nm thick n-GaN are grown under a nitrogen-rich condition with a substrate temperature of 819 °C, and Ga flux kept at $1.17\text{x}10^{-7}$ Torr. A graded $In_xGa_{1-x}N$ buffer layer, where the intended composition ranged from $0 < x < 0.4$, is achieved by lowering the substrate temperature from 819 °C to 631 °C in 10 steps, while Ga and In flux are held constant at $1.1\text{x}10^{-7}$ Torr and $4.3\text{x}10^{-8}$ Torr, respectively. During the growth of the active region, the substrate temperature is lowered to 433 °C, and the In flux is kept at $4.01\text{x}10^{-8}$ Torr during the growth of the whole active region. The barriers are grown by exposing the substrate to an additional Ga flux of $1.35\text{x}10^{-8}$ Torr. Sample C has four InN disks in the active region and a 150-nm thick p-GaN capping layer grown at 819 °C and a Ga flux = $9.63\text{x}10^{-8}$ Torr. Sample D is grown with six InN disks in the active region and omits the p-GaN capping layer. Transmission Electron Microscopy (TEM) samples are prepared either by removing the nanowires from the substrate and dispersed with water on a lacy carbon film mesh Cu TEM grid, or by Focused Ion Beam milling. In this case, the TEM sample is final polished using low voltage (2kV) and current (4pA) to avoid Ga damage.

Transmission Electron Micrographs and X-ray Energy Dispersive Spectroscopy (EDS) data are collected by JEOL JEM 2100 Scanning Transmission Electron Microscope (STEM) with a CEOS probe corrector and EDAX 100mm^2 SSD detector attached. The microscope is run in STEM mode with the lens settings defined at a probe size of about 0.15 nm for HAADF imaging and a detector collection inner angle of about 75mrad. The EDS mapping data are collected with Ga K peak at 9.24 kV and In L peak at 3.28 kV. For the EDS line profile, the distance between each data point is set at 2nm.

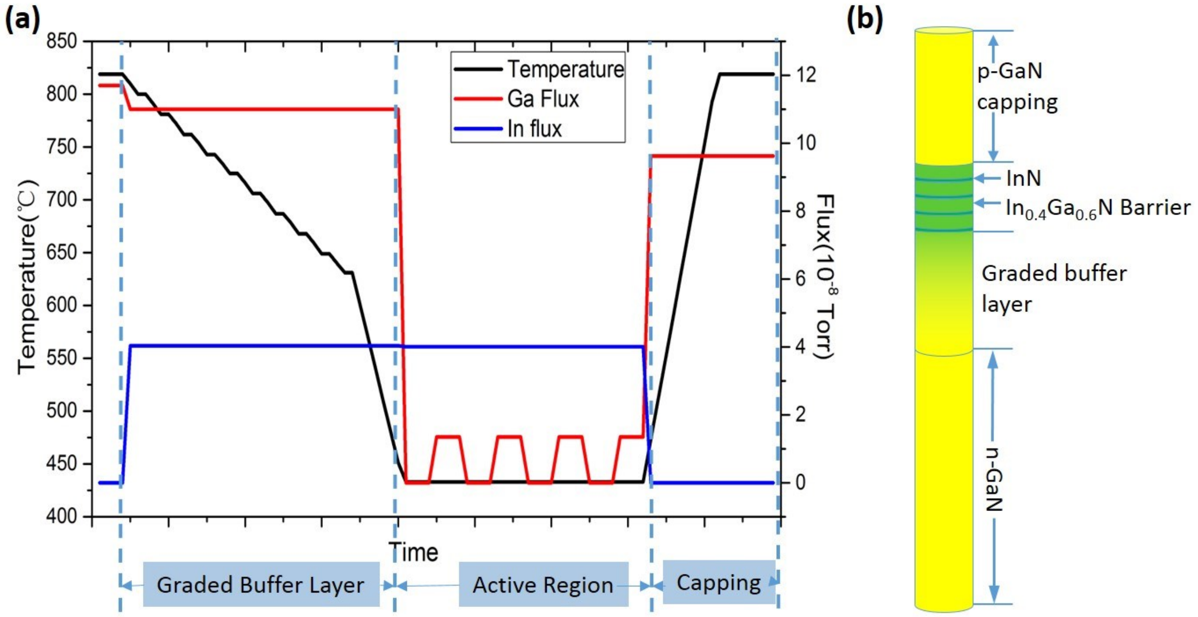

Figure 6-2. (a) Demonstrate of growth temperature(black) and group III fluxes used for Sample C (red for Ga and blue for In).

The shape of the nanowires can be altered by tuning the growth conditions and Indium composition. Figure 6-3 demonstrates the shape evolution observed. The prismatic shape is clear for low In Nanowire heterostructures with slight tapering at the top. The top view image (Figure 6-3(a))shows nanowires have hexagonal cross sections that tend to coalesce with increasing thickness, in agreement with other reports [11]. Protrusions occasionally observed, usually originating from the active region. As the Indium composition increases above 85% In, there is a drastic change in the nanowire shape compared to the lower composition nanowire heterostructures described in the Chapter 5. The top view SEM image (Figure 6-3 (d)) shows a primarily hexagonal cross sectional shape with a high density of protrusions. Looking at the side view SEM image (Figure 6-3(e)), these nanowires have more than one layer of protrusions. Pointy tips are commonly observed for these nanowires, but flat tops are also seen. The BF TEM image (Figure 6-3 (f)) also indicates voids present within these nanowires. As the Indium ratio increases to 1, the morphology becomes more complicated. Side view SEM image (Figure 6-3 (h)) shows the unique bimodal morphology. These nanowires no longer have hexagonal cross sections, and majority of nanowires have facetted tips.

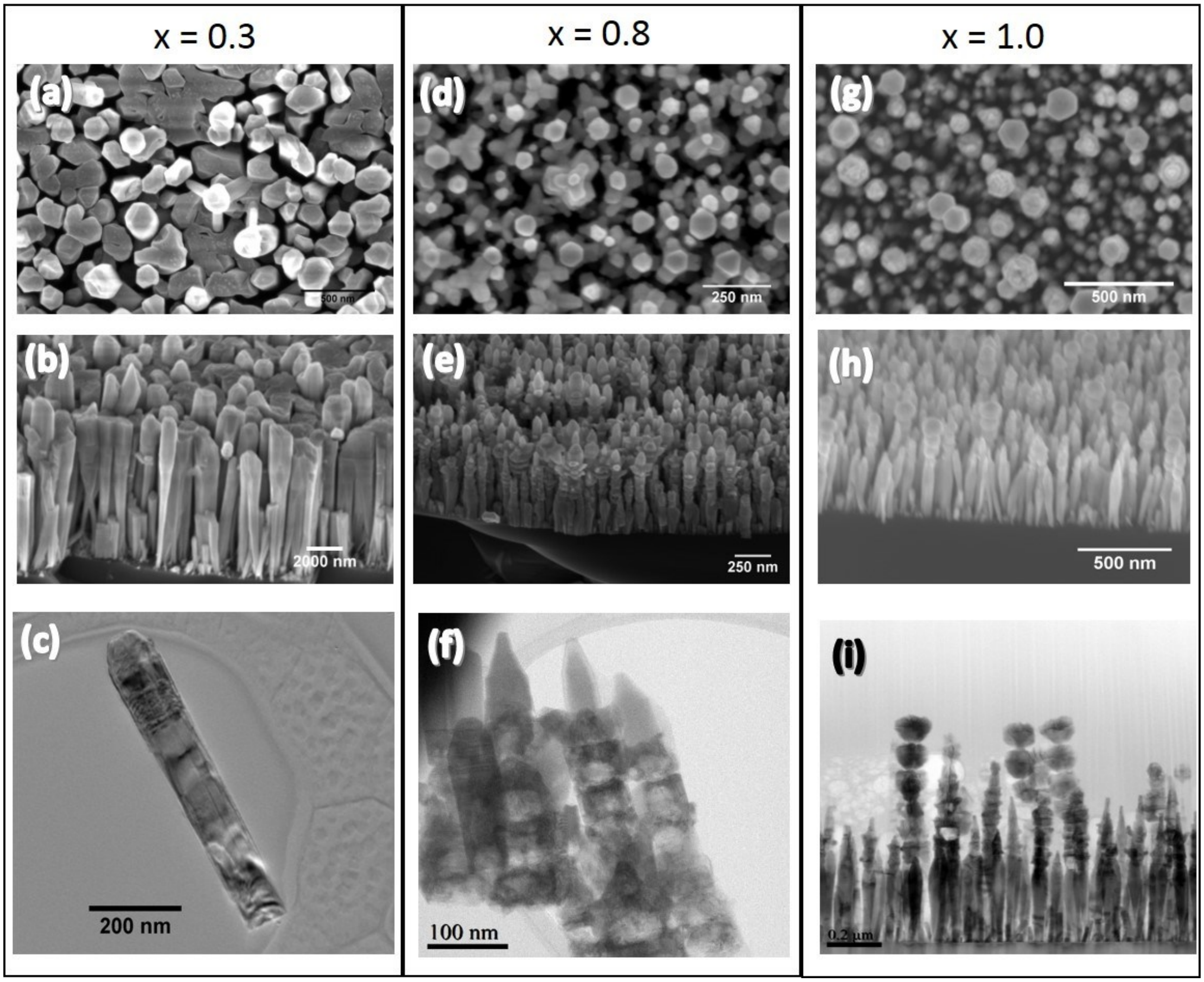

Figure 6-3. SEM and TEM images for InxGa1-xN heterostructure Nanowires (a) x = 0.3 (b) x = 0.85 (c) x = 1.0.

6.3 InN/InGaN Nanowire Bimodal Morphology

Figure 6-4 (a) shows a scanning electron micrograph (SEM) of the InGaN nanowire heterostructures for Sample C. The average length of the nanowires in sample C is ~500 nm, though the length varies from wire to wire. Instead of presenting a prismatic shape as reported for lower In composition nanowires heterostructures[12], these nanowires exhibit two distinct morphologies: a pointed pencil-shape and rounded polyhedral bead shape morphology. Figure 6-4(b) shows a cross section STEM image prepared by FIB cross-sectioning of the nanowire array with the two types indicated. Both pencil- and bead-like nanowires have complex morphologies. The pencil-like wires, which constitute ~60% of the array, sometimes exhibit periodic spike-like protrusions in the In-rich regions, in agreement with reports of $In_{0.4}Ga_{0.6}N$ disc-in-nanowires. [13] The bead-like wires, on the other hand, are comprised of highly faceted polyhedra. As can be seen from the image, the polyhedral bead shape nanowires are much taller than the pencil shape nanowires. The average height of pencil shape nanowire is ~400 nm while polyhedral bead shape nanowires are usually ~600 nm long. The size of the beads increase along the growth; lower beads have a diameter of ~50 nm while the topmost bead has a diameter of ~100 nm. For Sample D, a similar morphology separation is observed. The average height of the nanowires is ~700 nm with pencil shape nanowire of ~600 nm tall and bead shape nanowire of ~800 nm in height.

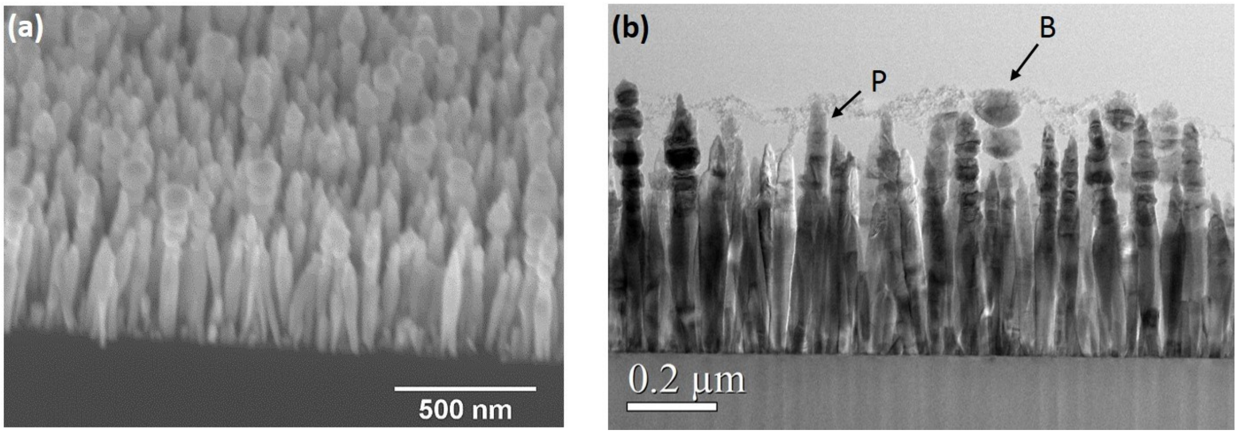

Figure 6-4. (a) SEM image of nanowire morphology for Sample C at 52°tilted, nanowires with pencil shape and polyhedral bead morphology are observed (b) Cross section STEM image of nanowires for Sample C.

Occasionally, nanowires possessing aspects of both pencil-shapes and bead-shaped nanowires occur. Figure 6-5(a) is a low magnification HAADF image of dispersed nanowires showing the top 400 nm of such a nanowire. Since the collection angle is kept at 75 mrad to reduce the contribution of thickness, the contrast is primarily determined by the composition of the region of interest. Thus, bright regions indicate higher In concentration. As it can be seen from Figure 6-5(a), this nanowire exhibits a structure different from the intended structure (Figure 6-5 (b)) in several aspects. According to the growth sequence, there ought to be 150 nm of p-GaN at the top of the nanowire. However, the HAADF images show that the topmost In-rich layer is less than 50 nm from the tip of the nanowire. Furthermore, the active region, intended to be comprised of four 6nm-thick InN layers separated by four 12 nm-thick $In_{0.4}Ga_{0.6}N$ barrier layers, is ~180 nm long, or three times the intended length. This suggests that there is a great deal of migration of Ga and In adatoms along the sidewalls, altering the effective growth rate of the nanowires. Figure 6-5(b)-(e) shows higher resolution images of the individual InN layers. Figure 6-5(b) shows the topmost layer, which closely resembles a nanodisk having a thickness of ~10 nm. Figure 6-5(c) shows the 2nd In-rich layer. The contrast in the image indicates that a large amount of In has been incorporated into this region, and shows an elongated hexagonal bipyramidal shape. Bright dots a few nanometers in diameter are also observed, as indicated in Figure 6-5(c), which could either indicate In-clusters within the In-rich region, 3D islands that have nucleated on the sidewalls. Figure 6-5(d) shows the 3rd region from the top, which displays evidence of a faceted In-rich nanodisk. This image also shows that there is a central and an outer portion of the nanowire exhibiting similar contrast. This effect is even more pronounced in Figure 6-5(e), where the central nanowire appears to be encased in an incommensurate 10-nm-thick shell. Thus, we propose that the majority of the p-GaN capping layer is distributed along the sidewalls of the nanowire. The 4th In-rich region from the top is also apparent in Figure 6-5(e), as indicated by the inverse tapering. [14] While there is some contrast visible due to In incorporation, it is much lower than in the other layers. The fact that there is apparently less In incorporated into the In-rich regions at the bottom of the structure than at the top strongly suggests segregation of In during the growth of the nanowire.

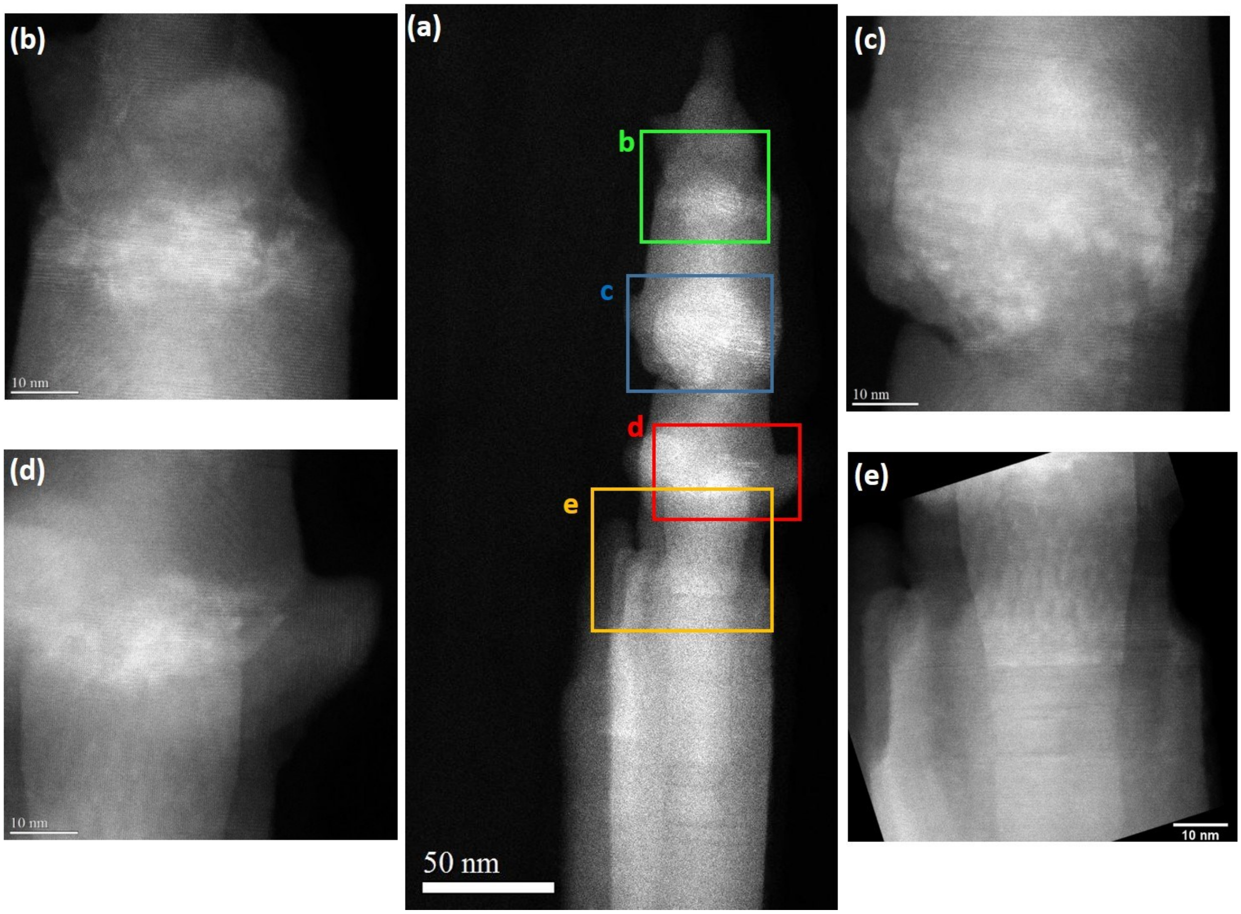

Figure 6-5. (a) HAADF STEM micrograph of a nanowire carrying features with both pencil shape and bead shape morphologies, with zoomed in micrographs from the top to the bottom of the active region. (b) Top most layer of InN nanodisk: intra dot formed within the nan nanowire (c) 3rd InN nanodisk region, octahedral shape bead formed (d) 2nd InN nanodisk region, facet formed and material latter being deposited could grow into branches on sidewall (e) 1st InN nanodisk region, diameter increase after In is introduced. A core-shell structure formed with n-GaN as the core and p-GaN as the shell.

Figure 6-6 presents a HAADF image a pair of pencil shaped nanowires dispersed on a Cu grid, along with the EDS mapping results for the Ga (Figure 6-6 (b)) and In distributions (Figure 6-6 (c)) within them. These images show that a Ga-rich shell wraps around each In-rich region. Figure 6-6(d) shows the line profile of the Indium composition for the line indicated in Figure 6-6(a). The composition is calculated based on the assumption that the total amount of group III elements (In and Ga) equals the amount of group V element (N), and the In composition is obtained by dividing the total number of In counts by the total number of counts for the group III elements. Four In-rich regions can be identified. The composition of the In-rich regions increases with increasing thickness, from ~60% in the bottom-most layer to ~80% for the topmost layer, in agreement with the qualitative observation of In segregation in Figure 6-6. Similarly, the composition of the barrier layers increases from ~0.2 for the layer just below the bottom-most layer, to ~0.3 for the layer above the topmost layer, again confirming strong In-segregation. The ratio of the InN disk/barrier layer has an average of 0.5 ± 0.2, while the intended ratio is 0.5.

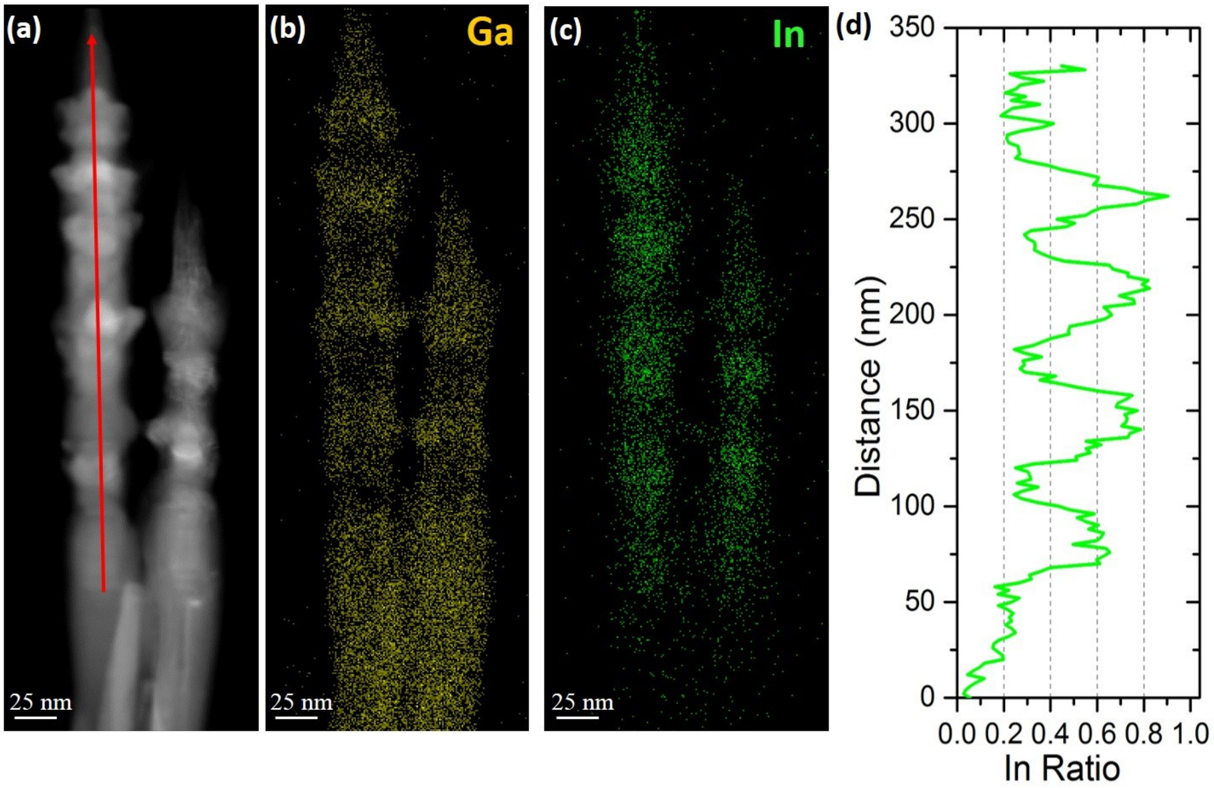

Figure 6-6. (a)-(d) EDS mapping results of a pencil shape nanowire (a) field of view with line indicating direction of line profile (b) Ga-rich region (c) In-rich region (d) line profile of calculated In ratio.

Figure 6-5 demonstrates the fairly complex morphology that results from a full p-i-n structure. Of particular concern is the p-GaN shell that envelops the core nanowire. To mitigate this issue, we also studied a structure of six layers of InN layers and omit the topmost p-GaN (sample D). Despite these modifications, the morphology of this sample is similar to Sample C shown in Figure 6-4(a) and (b); namely, it consists of a population of both pencil-shaped and polyhedral bead nanowires. Figure 6-7(a) shows a HAADF STEM image of a representative bead-like nanowire in sample D prepared by scratching nanowire off the substrate and dispersing them on the Cu TEM grid. Five polyhedral beads are visible in this nanowire, and the active region has a total length of ~300 nm. The bead diameter increases from ~50 nm to ~100 nm along the nanowire, which is comparable to the diameters observed in sample C. The two bottom-most beads are fairly narrow and largely obscured by a GaN shell despite the fact that there is no p-GaN top cladding layer. This suggests that there is a great deal of Ga-migration along the sidewalls even during growth of the barrier layers. In fact, it is likely that the 6th bead, the first one to be deposited, is entirely obscured by the GaN-shell. Figure 6-7(b) shows a higher resolution image of the 3rd bead from the top, and shows that the In-rich region (brighter contrast) forms the "pinhead" structure frequently observed for higher In concentration layers on GaN nanowires (Figure 6-1(d)). [8] A Ga-rich 37 nm thick barrier layer is observed on top of the pinhead, and a 5-15 nm thick Ga-rich shell surrounds the central InGaN region. The GaN shell is non-uniform and appears to have several surface steps and/or facets along its edge. Figure 6-7(c) is a higher magnification image of the 2nd bead from the top. The In-rich region is somewhat wider, 97 nm, and again forms a pinhead structure encapsulated with a non-uniform Ga-rich shell. The Ga-rich barrier layer exhibits contrast modulation parallel to the growth surface. Figure 6-7(d) shows the topmost bead, again comprised of an even wider 107 nm InGaN region, a striated Ga-rich barrier layer, but only a very thin (>5nm) GaN shell. The tip of the nanowire ends in a point. Figure 6-7(e) shows an atomic resolution HAADF STEM image near the tip, and shows that the basal planes are no longer perpendicular to the axis of the nanowire. Stacking faults are observed, and contrast variations on the order of 10-nm in diameter are apparent that may be related to In-clustering or 3D islands on the nanowire sidewalls.

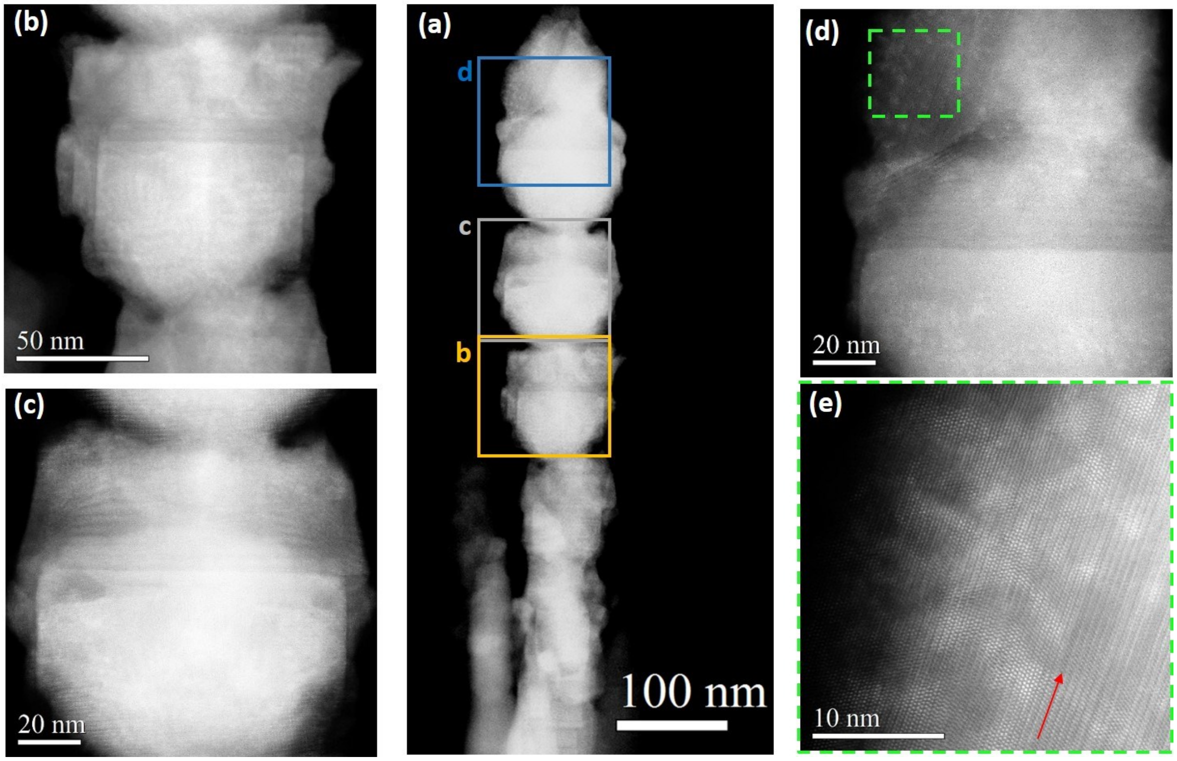

Figure 6-7. HAADF STEM micrograph of the half laser structure (Sample B) with zoomed in micrograph of the active region.

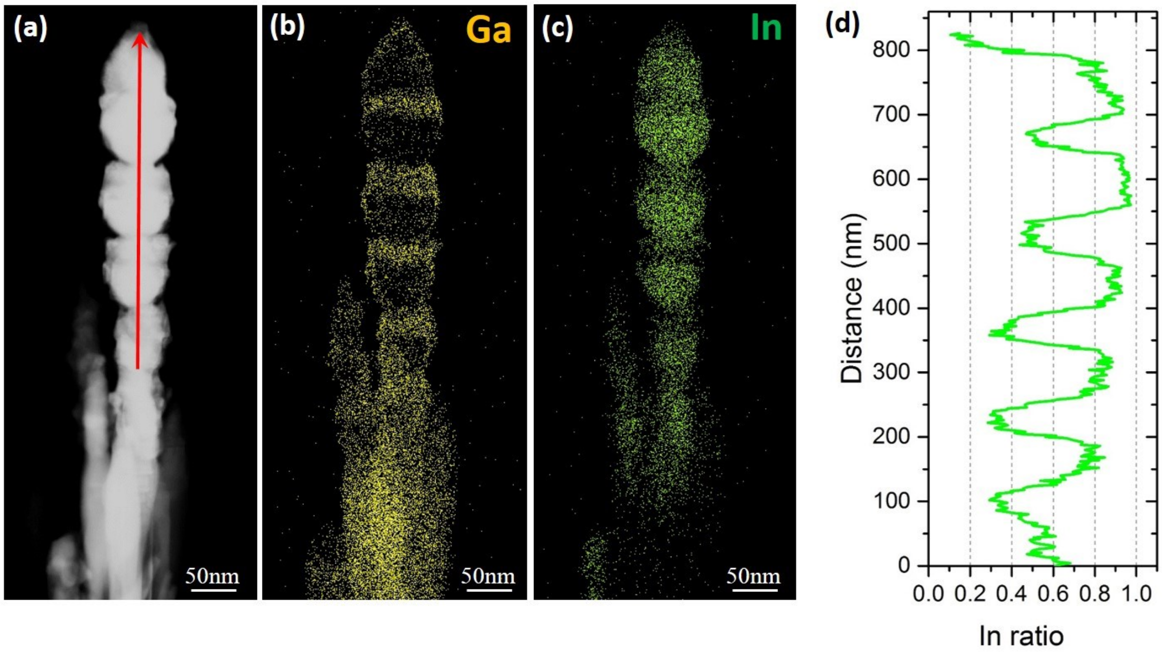

Figure 6-8. EDS Mapping results of a nanowire with half laser structure. (b) Ga-rich region (c) In rich region (d) Line profile of calculated In ratio.

Figure 6-8 presents the EDS data for the nanowire seen in Figure 6-7 both qualitatively and quantitatively. Figure 6-8(a) is the STEM image of the EDS data mapping area. The spatial distribution of Ga rich region and In rich region is shown in Figure 6-8(b) and (c). Figure 6-8(d) shows the line profile of In ratio calculated using the same method as Figure 6-6(d). As can be seen from the EDS results, a Ga shell is again apparent and is thicker for the lower beads. Similar to the pencil-like nanowires, the In composition of the bottom bead is ~65%, and increases monotonically with each bead, reaching a nominal composition of 90% for the topmost bead. The difference is that the In-rich regions for the bead-like nanowires are ~2x as thick, suggesting that the In layers have a higher growth rate than the pencil-like nanowires. The ratio of the InN disk/barrier layer has an average of 1.7±0.4 even though the intended value is 0.5. The Ga-rich barriers for these nanowires also increase in In concentration along the axis of the nanowire, however, the composition is somewhat higher than in the pencil-like wires, starting with 30% at the first barrier and increasing to 50% between the last bead and the apex of the wire. The nanowire-tip is In-rich in the center, with a thin GaN shell on its topmost surface. These data together again show that there is a strong driving force for In segregation along the axis of the nanowire, and migration of Ga along the sidewalls, in agreement with other reports.

The development of two different nanowire morphologies is unexpected. It is tempting to attribute the formation of the shorter wires due to shadowing of the taller wires; that is, the taller nanowires capture a higher fraction of the incoming flux thus starving out the smaller ones. Typically, this occurs when the flux impinges on the surface at an angle, with respect, to the growth axis of the nanowires [15], which is not the case in these growths. It is interesting to note that in addition to the length, the total amount of In in the bead-like wires is higher, especially in the barrier layers (see Figure 6-6(d) and Figure 6-8(d)). These observations suggest that there is higher In incorporation in the bead-like nanowires. Differences in the incorporation of In may be related to the polarity of the crystal structure in the nanowire. For instance, Zhang *et al.*[8] reported that InGaN layers only form on top of GaN nanowires that are entirely N-polar, and that nanowires having Ga-polar cores did not exhibit any In incorporation. The polarity of the initial GaN nanowires examined here could not be determined in these nanowires, due to the core-shell structure that develops as more InN-InGaN barrier layer pairs are deposited.

6.4 Bimodal Morphology Formation Mechanism

In order to determine the evolution of the nanowire morphology, an initial stage sample is grown. Figure 6-9(a) shows the intended structure: a 120-nm thick graded InGaN buffer layer on top of the 260-nm thick GaN root. As described before, the growth starts with substrate temperature of 819 °C and then decreased to 631 °C.

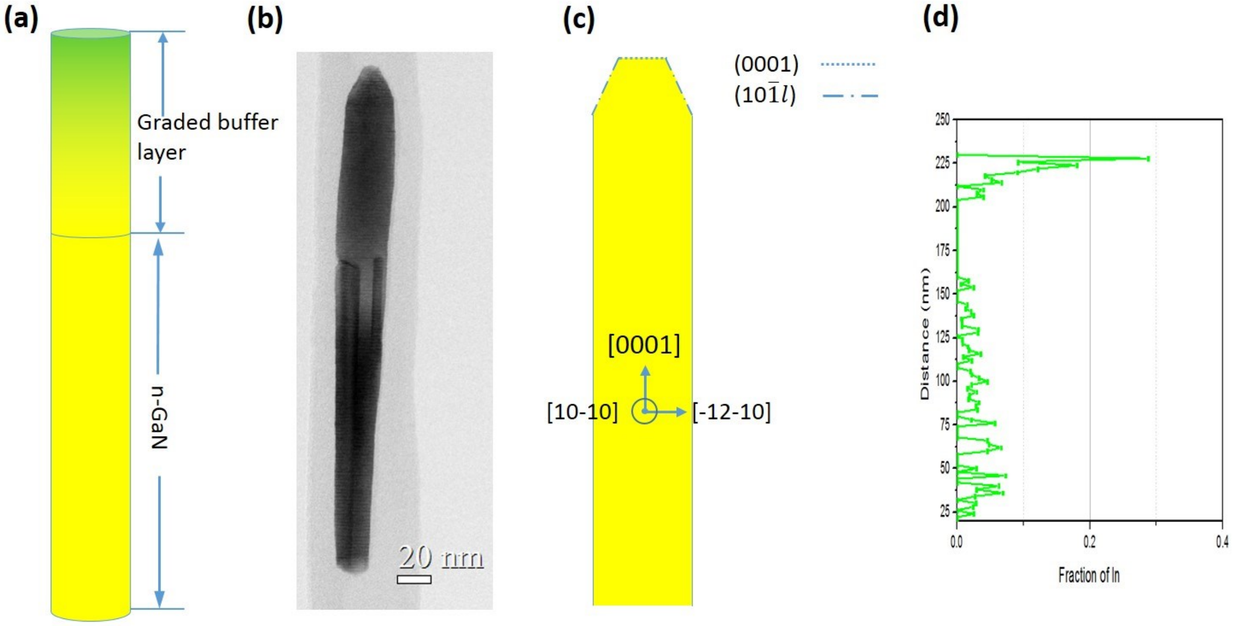

Figure 6-9. (a) Schematic showing the Initial stage nanowire structure (b) BF TEM image of a initial stage nanowire (c) schematic showing observed crystal planes for initial stage nanowires (d) line profile of In composition along the growth direction

During the decrease in temperature, the nanowire is exposed to In flux. The BF TEM image (Figure 6-9 (b)) shows that this nanowire starts with several skinny nanowires and coalescence at ~200 nm. The total length of the nanowire is measured to be 320 nm, which is slightly shorter than the intended height. The initial stage nanowires $(10\bar{1}l)$ faceted tips, where 1< l < 3, in agreement with prior report Kehagias et al.. [16] A schematic is shown in Figure 6-9(c) to crystal shape as well as the planes observed. Figure 6-9(d) shows the fraction of In from the EDS line profile. It can be seen that In incorporation is much lower than the intended composition (40%).

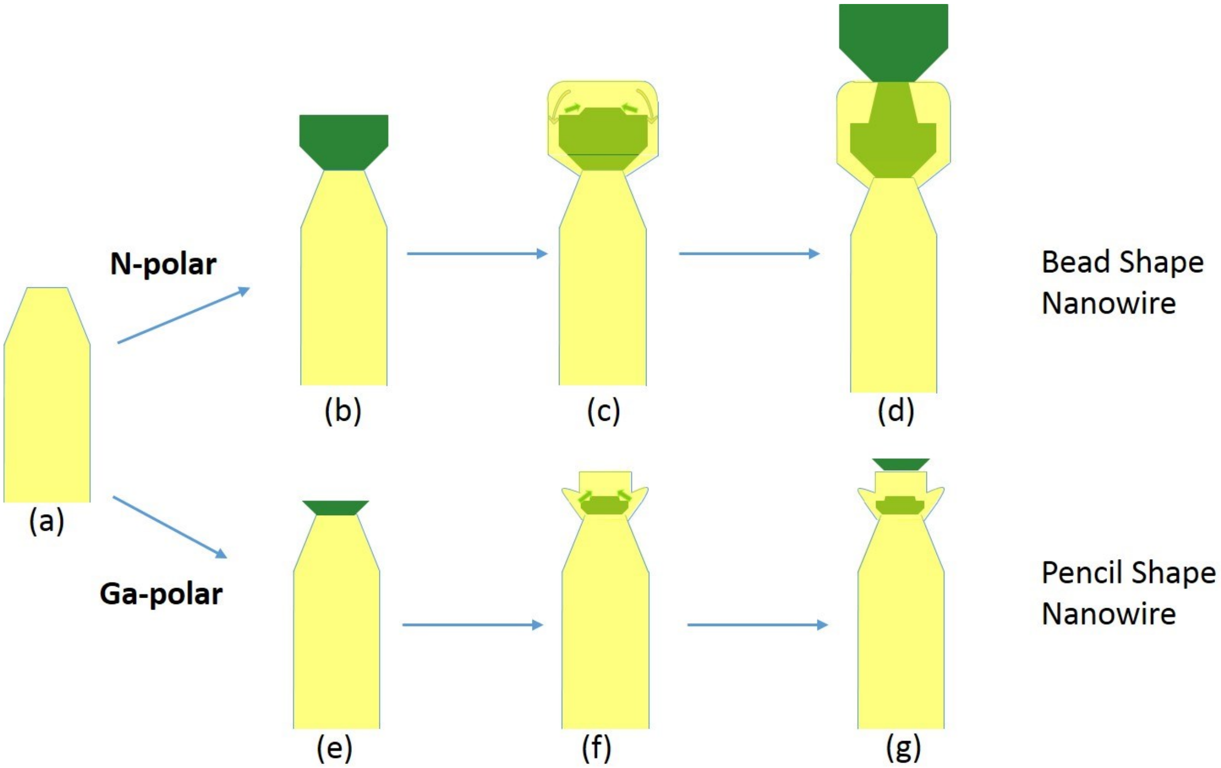

Figure 6-10. Schematic illustrating the formation of two morphologies.

The development of the two morphologies can be explained by variation in the In-incorporation rate, as illustrated schematically in Figure 6-10. The growth front of the InGaN graded layer is prismatic (Figure 6-10 (a)). Upon deposition of InN, the width of the nanowire initially increases until a new equilibrium width is reached, resulting in a pinhead structure (Figure 6-10 (b)).

Deposition of the Ga-rich InGaN barrier layer again proceeds prismatically, with a narrower basal plane region. At the same time, Indium tends to migrate towards the center and up the nanowire, and Ga tends to migrate away and down along the sidewalls, thus forming the Ga-rich shell (Figure 6-10 (c)). This process repeats for each InN-InGaN pair, resulting in a bead-like structure with a thicker Ga-rich shell towards the lower portion of the active region, and larger more In-rich beads towards the top of the active region (Figure 6-10 (d)). We propose that the pencil-like structure develops the same way, except that the lower In-incorporation rate results in thinner In-rich layers such that the pinhead structure does not form, resulting instead in an inverted pyramid shape (Figure 6-10 (e)). As the InGaN barrier layers are deposited, the Indium again migrates up and towards the center of the wire, with Ga migrating away and down. The spikey protrusions that form arise from the misorientation of GaN-shell in response to stacking faults in the In-rich layer. [17]

6.5 Optical Properties of InN/InGaN nanowire Heterostructure

Despite the complex composition profiles observed in these structures, the optical properties are surprisingly robust. Temperature dependent photoluminescence (PL) measurements are performed by placing the full-laser nanowire sample in a He cryostat and excited at 325 nm by a He-Cd laser. The PL analysis is performed by an Acton Spectrometer with a resolution of 0.03 nm, and the optical signal is detected with a liquid nitrogen cooled Ge detector. The temperature dependent PL spectra measured with an excitation intensity of 50 kW/cm^2 are shown in Figure 6-11(a). The emission peak at room temperature is at ~0.7 eV (1.75 μm), in reasonable agreement with the expected value for pure InN.[18] The variation of the PL emission peak energy with temperature, shown in Figure 6-11(b), can be fit using the Varshni equation [19]with the parameters aα = 0.37

meV/K and βb = 418K. The energy vs. temperature dependence does not show any S-type behavior, which suggests that the emission is not influenced by compositional inhomogeneities. [20] An approximate value of the internal quantum efficiency of 28% is obtained, from the ratio of the PL intensity at room and cryogenic temperatures at an excitation level of 50 kW/cm^2. This low value can be attributed to defects in the nanowire and disk regions that can either be caused by coalescing of nanowires during epitaxy, either due to misorientation, or due to increasing nanowire diameter at the low temperature of epitaxy. [11] These defects behave electronically as non-radiative deep levels. [21] Defects can also be created due to the lattice mismatch between the disk and barrier regions, and as a result of the Ga-rich shell enveloping the In-rich nanodisks.

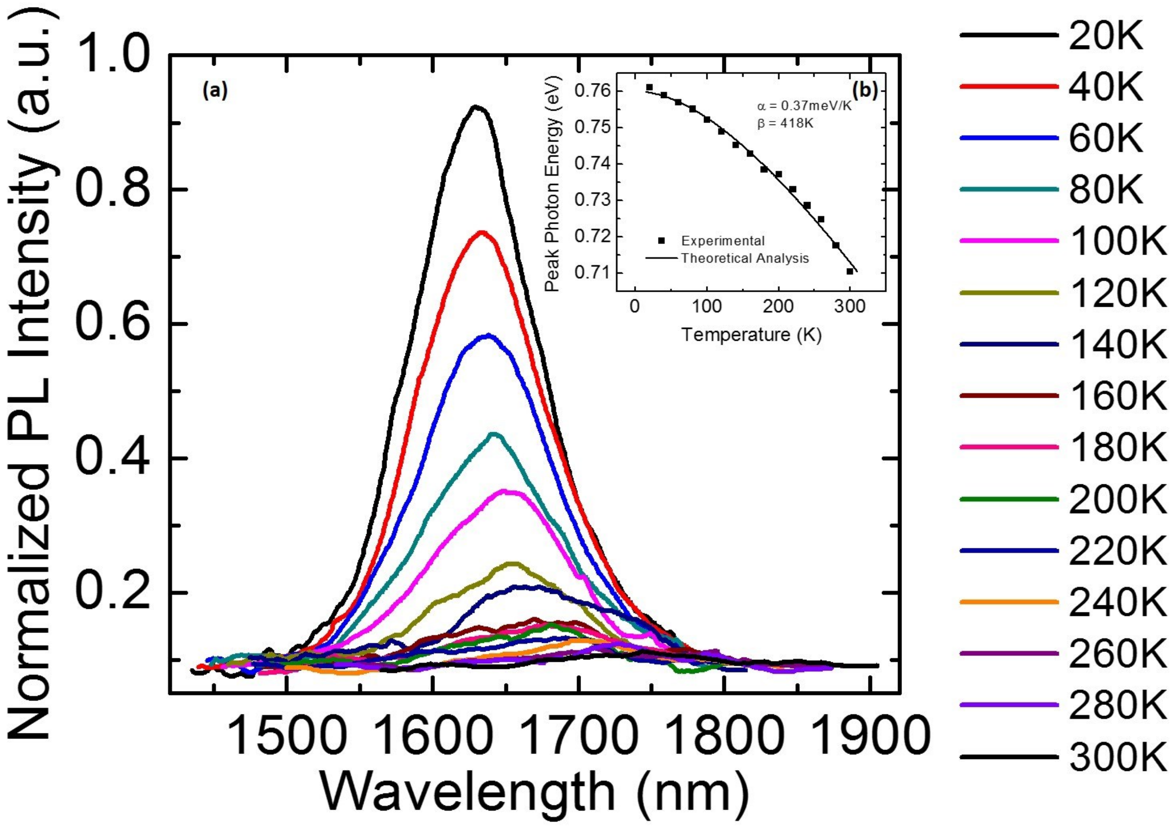

Figure 6-11. PL results of Sample A. Low temperature to room temperature (a) PL intensity and (b) Peak photon energy, both experimental data point and fitted curve. (Courtesy of Arnab Hazari)

6.6 Defects in InN/InGaN nanowires

Even though the small lateral dimensions are known to relieve strain [22], defects still occur in these nanowires. Multiple papers have reported defects, such as stacking faults and zinc blende domains for zero and low In (In)GaN nanowires.[23,14] Here secondary growth and zinc blende domains are also observed. In addition, defects such as cracks and dislocations are observed to relieve the high lattice mismatch strain between InN and InGaN.

6.6.1 Phase Switching & Secondary Growth

Phase switching originates from basal plane stacking faults, and they are considered a major source of non-radiative recombination. The type of stacking faults in these nanostructures is identified as I1, with the ABABCBCB…stacking sequence. [14] [16] The I1 type stacking faults are not considered to be strain-induced, but more of a result of kinetic during growth because formation energy is only 10 meV/unit cell area.[24] Consecutive basal stacking faults result in a zinc blende region. It has been shown that these zinc blende regions can act as quantum wells, resulting in a blue shift with increasing excitation power. [25]

Figure 6-12 shows High Angle Annular Dark Field (HAADF) and Bright Field (BF)TEM images of the nanowire array prepared by FIB for a similar nanowire on Sample C. The low-magnification DF image (Figure 6-12 (a)) shows the contrast modulation parallel to the basal plane, but the corresponding BF image (Figure 6-12 (b)) and high resolution image (Figure 6-12 (c)) clearly shows that this contrast results from stacking faults. In this case, the brighter regions correspond to higher density zinc blende phase, while the darker regions correspond to lower density wurtzite phase. It is interesting that the phase switching all seems to appear in the InGaN barrier layers, suggesting that stacking fault injection may be associated with specific In concentrations. Further research needs to be done to understand this observation.

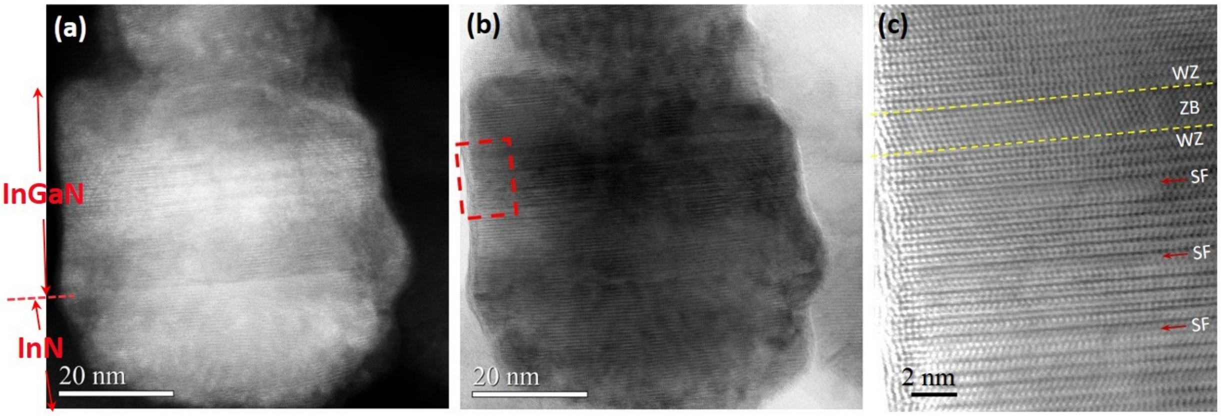

Figure 6-12. (a) HAADF STEM image of the active region in Sample C, InN and InGaN region being pointed out (b) BF STEM image of the same region (c) BF image of the region circled out the region in (b). Switching between wurtzite (WZ) and zinc blende (ZB).

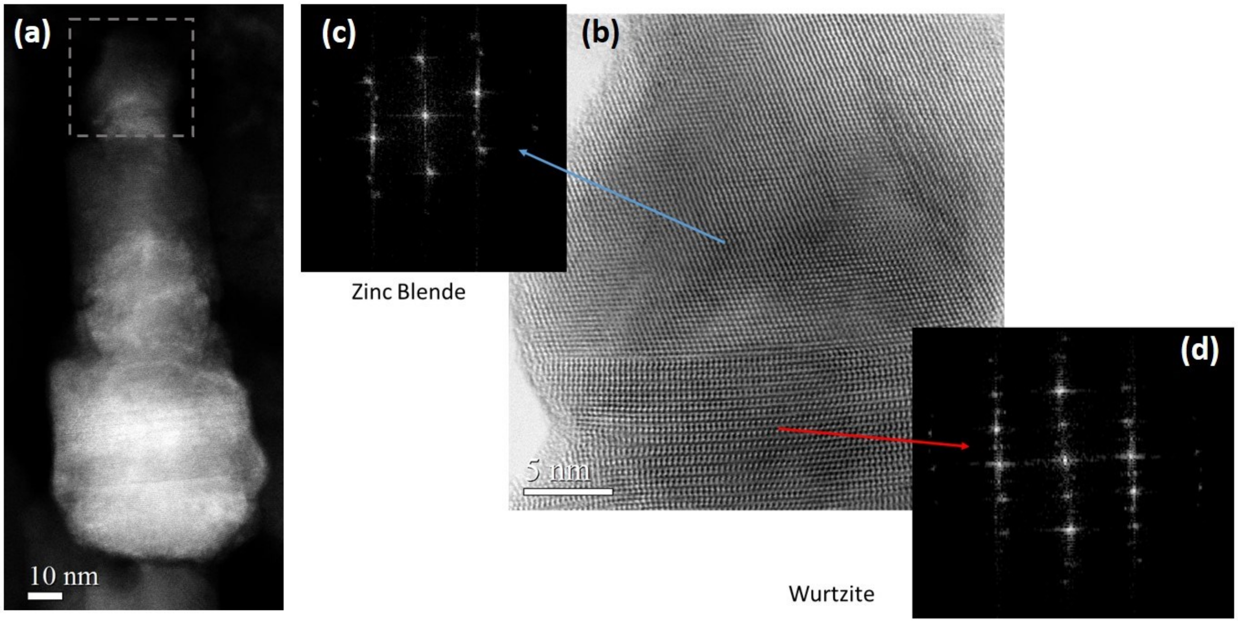

Figure 6-13. (a) HAADF STEM image of a bead shape nanowire, with region zoomed in (b) circled out. (b)BF TEM image showing change of growth front change upon phase switching (c) FFT diffraction pattern of zinc clende(ZB) region (d) FFT diffraction pattern of wurtzite(WZ) region.

As the zinc blende region grows, the growth front does not always return to the (0001) direction. Figure 6-13(a) is the HAADF TEM micrograph of a nanowire and the region where a significant zinc blende region is circled out. Figure 6-13(b) is the high resolution TEM micrograph of that region. The nanowire has the wurtzite crystal structure initially, then switches into zinc blende crystal structure. The basal plane of the wurtzite phase can re-nucleated on any (111) zinc blende plane, and in this case, it nucleated on a (111) plane not parallel to the original growth direction. As a result, the zinc blende region took on a tetrahedral shape. Schuster et al. observed nano-tripods show three-fold symmetry, and further investigation showed that tetrahedral zinc blende GaN at their core. [26] Here we propose the facets present with zinc blende regions can also further develops into angled lateral branching. Indeed, it is observed that lateral branching form upon zinc blende nanowire core. Figure 6-14(a) shows a low magnification BF TEM image for a nanowire with a pair of lateral branches, the circled region is shown in Figure 6-15(b). As it can be seen from this image, zinc blende nanowire core can act as a base for lateral branching.

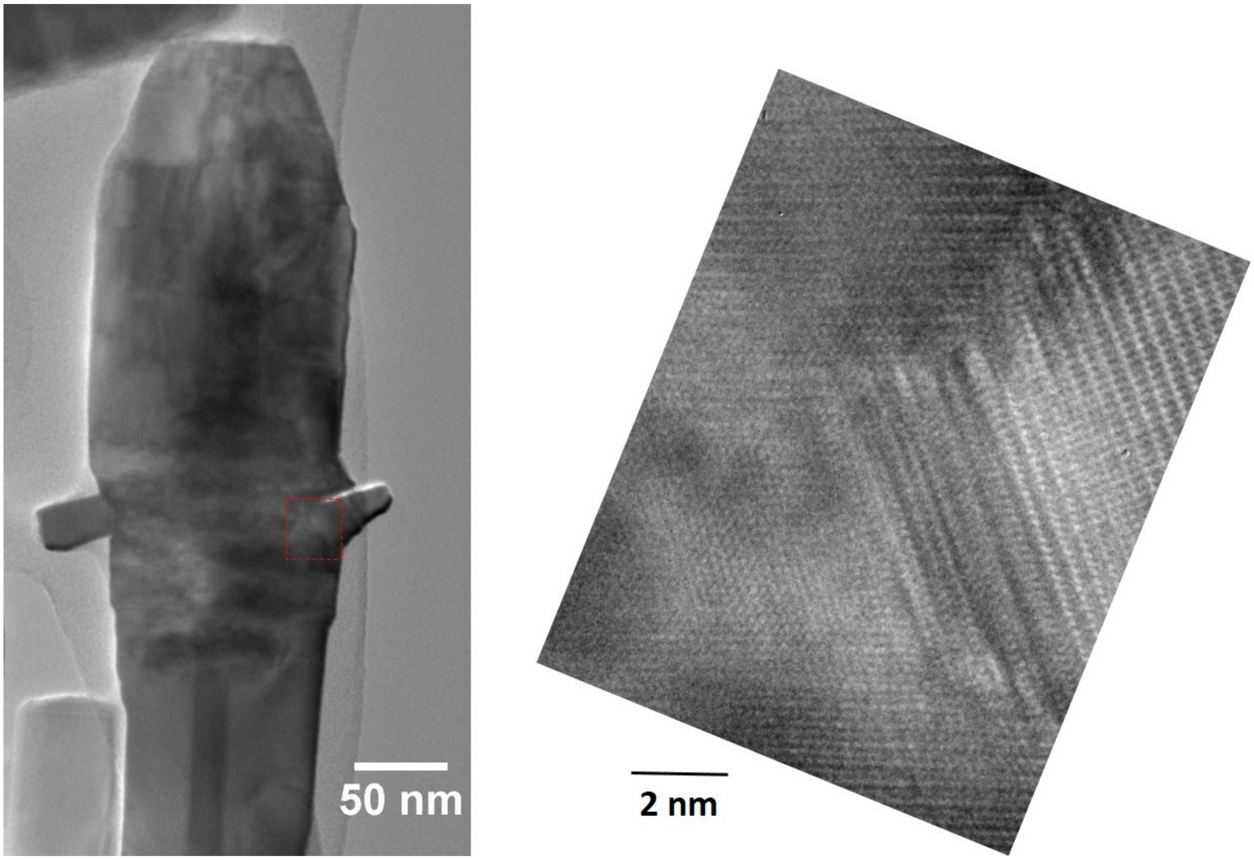

Figure 6-14. (a) BF TEM image of $In_{0.5}Ga_{0.5}N$ nanowire (b) HRTEM image of lateral branching upon zinc blende regions.

Secondary growth is commonly seen on the nanowire sidewall. Occasionally, twinning precipitates can be observed. Figure 6-15 shows the HAADF image where two twinning precipitates grown on the side wall of the nanowire. Both precipitates, including the nanowire, has wurtzite crystal structure. A dislocation can be seen at the interface of the nanowire and one of the precipitates. The dislocation is introduced to relive the strain between the precipitate and the nanowire. Figure 6-15 (b) is the Fast Fourier Transform(FFT) of the whole TEM image and (c) is FFT of the area circled by a red square, indicates twinning precipitates combined. The angle between the twins is 125 ^{o}.

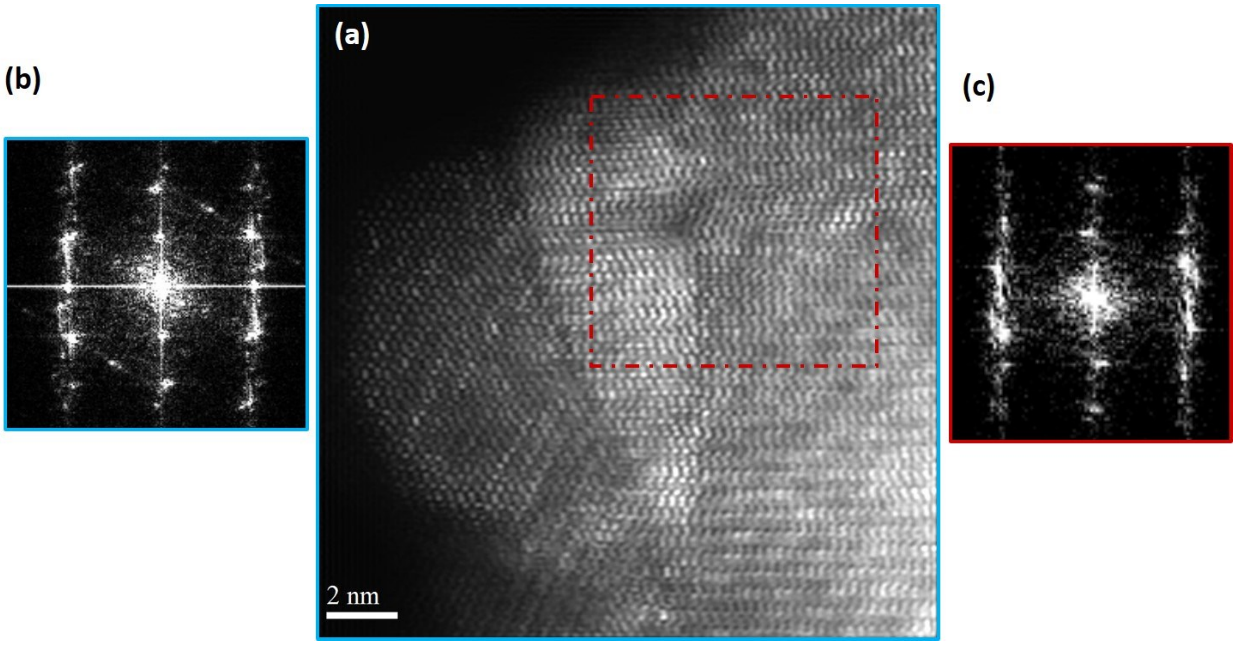

Figure 6-15. (a) HAADF TEM image showing twinning precipitates nucleate on nanowire sidewall (b) FFT of the entire image, twinning can be seen. (c) FFT of the area circled out with the red square area.

6.6.2 Cracks

The InN/$In_{0.4}Ga_{0.6}N$ nanowires contain a high lattice mismatch strain within the structure (>0.06). Rather than forming strain relieving 3D islands as in the wires with lower In content (see Figure 6-1(b)), the bead-shaped nanowires formed cracks along their diameter. Figure 6-16 shows the HAADF TEM images of one of the cracked beads. As can be seen, the region above the crack is slightly tilted with respect to the region beneath, and the surface along the crack is rough. Nanowire cracking was reported by Laskar et al. [27] and Tourbot et al.[28] before. Laskar reported cracks occur only when wire composition graded from InN to GaN (tensile strain). But growth in the reverse grading, from GaN to InN, would not result in cracking. The cracks appear probably due to large lattice mismatch cannot be sufficiently relieved by other mechanisms. Tourbot et al. reported cracks observed in GaN to InGaN interface, which is in compressive strain. They proposed that elastic and plastic strain relaxation can both happen for InGaN nanowires. Elastic strain relaxation is associated with In-rich cluster formation, while plastic relaxation has been found to result from interfacial dislocation formation. The dislocation formed between the interface would result in cracking between InGaN/GaN interface. [28]

The length of the cracks (in nm) and the thickness for the whole beads for eight cracks along the diameter are measured and plotted in Figure 6-17. The bead thickness is either around 50 nm thick, or around 120 nm thick. The length of the crack is mostly within the range of 12 nm to 20 nm. It can be seen from the Figure 6-17 that the crack length seems to increase with larger bead size, though not a clear trend can be concluded without further investigation.

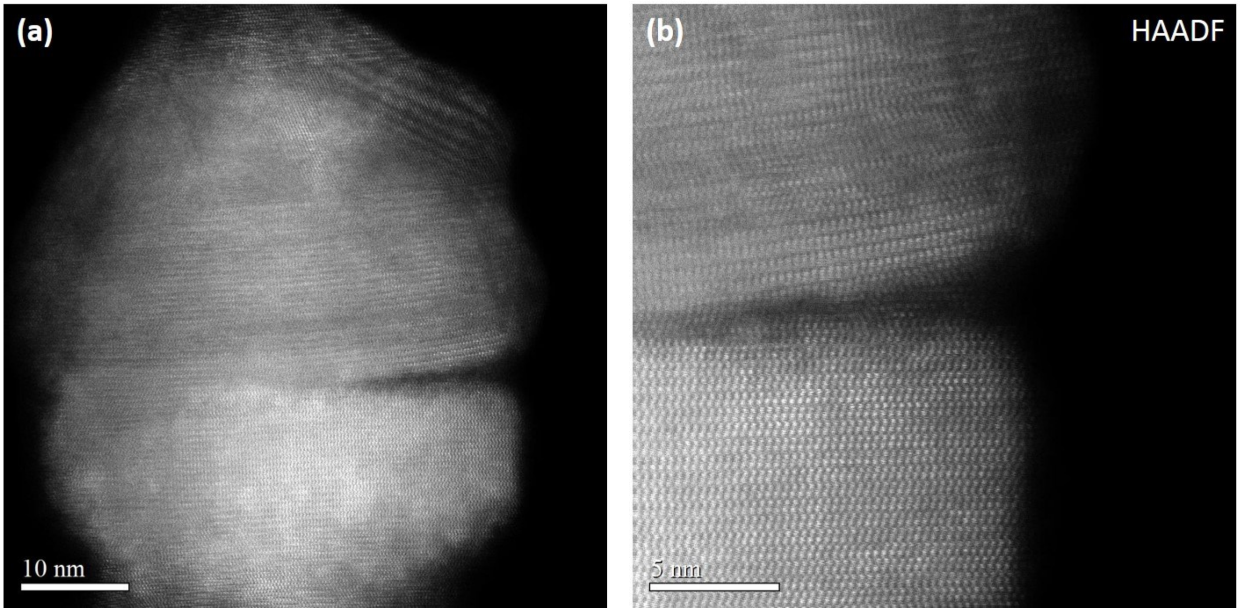

Figure 6-16. HAADF TEM image of a bead with cracks on the right side (b) zoomed in high resolution image

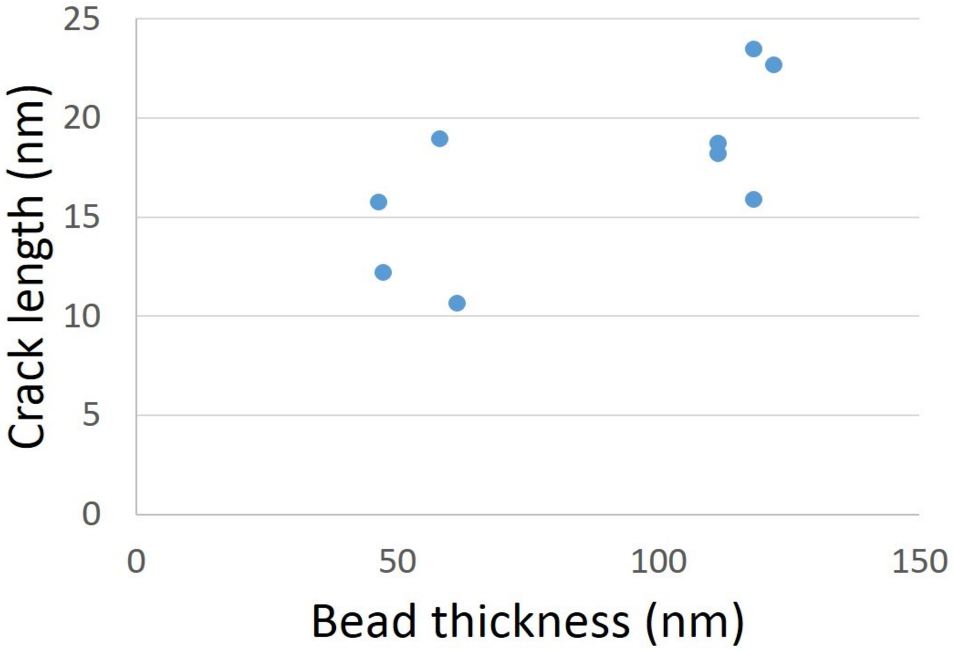

Figure 6-17. Measured crack length vs. the thickness of the whole beads.

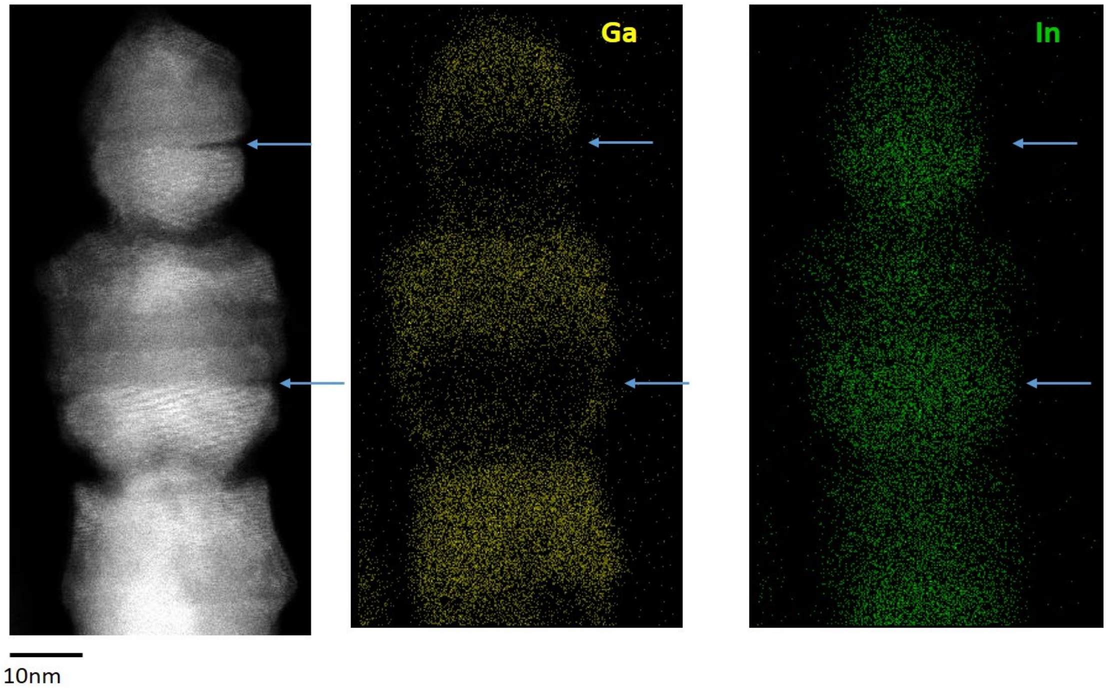

Figure 6-18. HAADF TEM image (left) of a bead shape nanowire with the position of the cracks pointed out. (b) EDS mapping of Ga in the area (b) EDS mapping of In in the area.

Figure 6-18 is the HAADF image of the same nanowire, combined with EDS mapping of Ga and In. The position of the cracks has been pointed out. Cracks do not always happen at the interface between In-rich bottom half and Ga-rich upper half. Sometimes, the crack is located below the InN/InGaN interface. Elastic constants for InN and GaN indicate that InN is much softer than GaN, therefore cracks tend to form in the InN region.

6.7 Summary

In conclusion, this chapter shows that the shape of these InGaN heterostructure nanowires can change drastically with increasing amount of In incorporated. The growth of high lattice matched InN-InGaN heterostructure nanowires would result in two distinct morphologies: shorter sharp-tipped pencils and longer rounded beads. This dual morphology may be explained by a wire-to-wire variation in the In incorporation rate, possibly due to variation in the polarity of the underlying crystal structure. The bead-like wires tend to be longer, overall, and have thicker In-rich layers than the pencil-like wires. The composition of the In-rich regions in both types are nominally the same, but the In composition of the barrier layers is higher for the bead regions. Both types of wires show evidence that there is significant Indium segregation up and towards the center of the wire, and Ga migration away and down along the wire sidewalls of the wires. The Ga-shell is not always epitaxial grown the underlying crystal, possibly due to the low growth temperature, stacking faults, or lattice mismatch. Despite the complex morphologies, the optical properties of these structures are very good, with strong emission at energies consistent with homogeneous InN layers. Investigation of the initial stage nanowires reveals the graded buffer layer induces a tapering shape. The formation of both pencil shape and bead shape nanowires are illustrated, combining the observation from this work as well as other publications.

Due to the high lattice mismatch, various kinds of defects have been observed. Stacking fault insertions occur on the basal plane. Consecutive layers of stacking fault would form zinc blende regions in the nanowires. The facets originating from zinc blende regions can switch back in to wurtzite structure, and this might be one major source of lateral branching for these nanowires. Twinned precipitates can nucleate on the sidewall of these nanowires and misfit dislocations are also observed. To relieve the strain between In-rich and Ga-rich regions, cracks would form on or below the interfaces.

Future work can be done on building a model to obtain a better understanding of the phase switching. With the ability to predict phase switching and being able to reduce their occurrence, the luminescence can be greatly improved in the near future.

6.8 References

1. Calleja, E. *et al.* Growth, morphology, and structural properties of group-III-nitride nanocolumns and nanodisks. *Phys. Status Solidi* **244,** 2816–2837 (2007).

2. Sarwar, A. T. M. G. *et al.* Self-assembled InN micro-mushrooms by upside-down pendeoepitaxy. *J. Cryst. Growth* **443,** 90–97 (2016).

3. Guo, W., Zhang, M., Bhattacharya, P. & Heo, J. Auger recombination in III-nitride nanowires and its effect on nanowire light-emitting diode characteristics. *Nano Lett.* **11,** 1434–1438 (2011).

4. Deshpande, S. *et al.* Formation and Nature of InGaN Quantum Dots in GaN Nanowires. *Nano Lett.* 150209130609008 (2015). doi:10.1021/nl5041989

5. Deshpande, S., Heo, J., Das, A. & Bhattacharya, P. Electrically driven polarized single-photon emission from an InGaN quantum dot in a GaN nanowire. *Nat. Commun.* **4,** 1675 (2013).

6. Fernández-Garrido, S., Grandal, J., Calleja, E., Sánchez-García, M. a. & López-Romero, D. A growth diagram for plasma-assisted molecular beam epitaxy of GaN nanocolumns on Si(111). *J. Appl. Phys.* **106,** 2009–2011 (2009).

7. Grandal, J., Sánchez-García, M. a., Calleja, E., Luna, E. & Trampert, a. Accommodation mechanism of InN nanocolumns grown on Si(111) substrates by molecular beam epitaxy. *Appl. Phys. Lett.* **91,** 21902 (2007).

8. Zhang, X. *et al.* InGaN nanowires with high InN molar fraction: growth, structural and optical properties. *Nanotechnology* **27,** 195704 (2016).

9. Wang, T. Topical Review: Development of overgrown semi-polar GaN for high efficiency green/yellow emission. *Semicond. Sci. Technol.* **31,** 93003 (2016).

10. Qian, F. *et al.* Multi-quantum-well nanowire heterostructures for wavelength-controlled lasers. *Nat. Mater.* **7,** 701–706 (2008).

11. Grossklaus, K. a., Banerjee, a., Jahangir, S., Bhattacharya, P. & Millunchick, J. M.

Misorientation defects in coalesced self-catalyzed GaN nanowires. *J. Cryst. Growth* **371,** 142–147 (2013).

12. Nguyen, H. P. T. *et al.* p-Type modulation doped InGaN/GaN dot-in-a-wire white-light-emitting diodes monolithically grown on Si(111). *Nano Lett.* **11,** 1919–24 (2011).
13. Yan, L. *et al.* Structural and optical properties of disc-in-wire InGaN/GaN LEDs. *Nano Lett.* **15,** 1535–1539 (2015).
14. Zhou, X. *et al.* Nanoscale Optical Properties of Indium Gallium Nitride / Gallium Nitride. (2015).
15. Sibirev, N. V. *et al.* Influence of shadow effect on the growth and shape of InAs nanowires. *J. Appl. Phys.* **111,** (2012).
16. Kehagias, T. *et al.* Nanostructure and strain in InGaN/GaN superlattices grown in GaN nanowires. *Nanotechnology* **24,** 435702 (2013).
17. Bierman, M. J., Lau, Y. K., Kvit, A. V, Schmitt, A. L. & Jin, S. Dislocation-driven nanowire growth and Eshelby twist. *Science (80-.).* **320,** 1060–1063 (2008).
18. Matsuoka, T., Okamoto, H., Nakao, M., Harima, H. & Kurimoto, E. Optical bandgap energy of wurtzite InN. *Appl. Phys. Lett.* **81,** 1246–1248 (2002).
19. Varshni, Y. P. Temperature dependence of the energy gap in semiconductors. *Physica* **34,** 149–154 (1967).
20. Bell, A. *et al.* Exciton freeze-out and thermally activated relaxation at local potential fluctuations in thick Al xGa 1-xN layers. *J. Appl. Phys.* **95,** 4670–4674 (2004).
21. Jahangir, S., Mandl, M., Strassburg, M. & Bhattacharya, P. Molecular beam epitaxial growth and optical properties of red-emitting (λ = 650 nm) InGaN/GaN disks-in-nanowires on silicon. *Appl. Phys. Lett.* **102,** 71101 (2013).
22. Glas, F. Critical dimensions for the plastic relaxation of strained axial heterostructures in free-standing nanowires. *Phys. Rev. B* **74,** 121302 (2006).
23. Tham, D., Nam, C. Y. & Fischer, J. E. Defects in GaN nanowires. *Adv. Funct. Mater.* **16,**

1197–1202 (2006).

24. Stampfl, C. & Van de Walle, C. Energetics and electronic structure of stacking faults in AlN, GaN, and InN. *Phys. Rev. B* **57,** R15052–R15055 (1998).

25. Jacopin, G. *et al.* Optical properties of wurtzite/zinc-blende heterostructures in GaN nanowires. *J. Appl. Phys.* **110,** (2011).

26. Schuster, F. *et al.* Position-controlled growth of GaN nanowires and nanotubes on diamond by molecular beam epitaxy. *Nano Lett.* **15,** 1773–1779 (2015).

27. Laskar, M. R. *et al.* Molecular Beam Epitaxy of Graded-Composition InGaN Nanowires. doi:10.1007/s11664-013-2544-9

28. Tourbot, G. *et al.* Structural and optical properties of InGaN/GaN nanowire heterostructures grown by PA-MBE. *Nanotechnology* **22,** 75601 (2011).